

Title	宙吊りグラフェン・フォノン結晶 (GPnC)における熱輸送の研究
Author(s)	HAQUE, MAYEESHA MASRURA
Citation	
Issue Date	2020-09
Type	Thesis or Dissertation
Text version	ETD
URL	http://hdl.handle.net/10119/17015
Rights	
Description	Supervisor:水田 博, 先端科学技術研究科, 博士

Doctoral Dissertation

Thermal Transport in Suspended Graphene Phononic Crystal (GPnC)

by,

Haque Mayeesha Masrura

Supervisor: Professor Hiroshi Mizuta

School of Materials Science

Japan Advanced Institute of Science and Technology (JAIST)

June 2020

DECLARATION

I, Haque Mayeesha Masrura bearing the student ID s1620426 in JAIST, declare that this thesis is the result of my research, which is the outcome of work done in close collaboration with my colleagues, except - where specifically indicated in the text. It has not been previously submitted, in part or whole, to any University of the institution for any degree, diploma, or other qualification.

Signed: _____

Date: _____

ABSTRACT

With the advances in the field of electronics, it has become relevant to reflect on the ever-growing problem of management of waste heat and probe further into nanoscale heat transport as the devices are being vigorously scaled down to tens of nanometers. The physical entity that can help create thermal blockade is now defined as phononic crystals (PnCs) in the community- the terminology rooted into the word 'phonon' which represents the quanta of atomic vibration in materials. Fabrication of PnCs has become a subject of interest for the potential it offers for heat propagation control. Fabrication of intricate nanopatterns on materials like silicon and steel has long since been realized with the optimization of various focused ion beam (FIB) techniques. However, it has been reported that, with superior physical and mechanical properties i.e. Young's modulus (~ 1 TPa) and Debye temperature (~ 1900 K), graphene offers better flexibility and control of phonon contributions. In this work, we have reflected on the asymmetry in thermal transport in graphene phononic crystals as an initial study to understand thermal rectification characteristics in nanoscale devices.

First, the dispersion curves and transmission probability of graphene based phononic crystals by configuring different periodicity, porosity and pore shape were studied by Finite Element Method simulations. From the dispersion relations, obvious band flattening or distinct frequency regions were observed where phonon transmission was completely blocked. The analysis showed strong evidence of porosity and pore shape dependency on phononic band gap (PnBG) generation. For circular shaped nanopores, a very small PnBG opens at ~ 0.4 THz only at a high porosity over 0.73 which is extremely difficult to achieve using the current experimental facilities. To address this limitation, cross shaped nanopore pattern was introduced where PnBG opened at a porosity ~ 0.28 . The PnBG was most obvious at ~ 0.9 THz for single nanometer neck length and completely disappeared when it increased to 10 nm indicating that the constrictions due to the narrow neck structure induced phonon modes confinement contributing to the suppression or flattening of the dispersion relation. At similar porosity and unit cell size, snowflake shaped pores exhibited phononic bandgap (PnBG) in gradually higher THz (~ 1.5 THz) regime as the symmetric placement of the neck length along all the supercell edges reinforced the phonon confinement. Also, the snowflake shaped nanopattern gives the advantage of having larger neck lengths of ~ 10 nm.

Next, a reproducible hybrid method was developed and demonstrated to successfully fabricate large area (in μm^2 dimensions) suspended graphene nanomesh (GNM). The GNR are patterned

into required dimensions using EBL and later suspended by buffered hydrofluoric acid (BHF) release with gold electrodes acting as a heater. The GNM is fabricated by milling periodic nanopores with as small as ~ 6 nm diameter on the suspended GNR by direct focused helium ion beam milling (HIBM). Taking advantage of the fidelity of HIBM, symmetric and asymmetric graphene nanomesh (GNM) samples were fabricated. The concept of resistive thermometry was used to develop a 4-probe measurement method for thermal characterization of the prepared GNM devices which had 20 nm, 25 nm and 30 nm pitch and ~ 6 nm diameter nanopores. With the base temperature maintained at 150K in a cryogenic vacuum probe station, joule heating was used to generate temperature at the metal electrode. With the measurement setup, resistance at the electrode was measured accurately and the corresponding temperature was calculated. By observing the change in temperature at the heater when there is GNM present, it was confirmed that some of the heat is dissipated through the GNM. The measurement was adopted to observe the trend of thermal dissipation through asymmetric and symmetric GNM by maintaining similar experimental conditions and most interestingly, characteristics of thermal rectification by introducing asymmetry in the GNM was observed when the heater position was changed. It was observed that the heat transport through the non-meshed area of the patterned GNR to the meshed area is larger compared to when the heater position is swapped and heat transport direction is from the meshed area to the non-meshed area.

Keywords: Graphene phononic crystal, Graphene nanomesh, Helium ion beam milling, Phononic bandgap, Resistive thermometry, Thermal rectification.

Acknowledgement

Being a relatively new research field, the project of phonon engineering that I was involved with, has been challenging in many aspects. However, it has also been a rewarding journey to be able to develop an understanding on the subject. My deepest gratitude extends towards the Almighty and the following persons, who have, in one way or another, contributed to bring this research into fruition.

***Professor Hiroshi Mizuta**, my research supervisor, for his guidance, scholastic critique, moral support, and demonstrating unperturbed patience in understanding my limitations as an individual, both at a personal and academic level, from the initialization of this project till the production of this dissertation.*

***Dr. Manoharan Muruganathan**, my co-supervisor, for his time and effort in assisting me with every technical predicament, being extremely meticulous about every submission procedure with his selfless support throughout this journey despite all the adversities.*

*The honorable members of my thesis reviewing committee - **Professor Mikio Koyano**, **Professor Masashi Akabori**, **Professor Eisuke Tokumitsu** of JAIST and **Professor Shinji Matsui** (Professor Emeritus, University of Hyogo) for their insightful critique in evaluating this work.*

***Professor Yukiko Takamura**, my second supervisor and **Professor Yoshifumi Oshima**, my supervisor for Minor Research Theme, for their relentless support when it came to meeting the deadlines and being there as teachers I could always look up to.*

***Dr. Marek Edward Schmidt**, for being an incredible mentor, for the innumerable hours spent in the clean room learning from him first hand every technique to produce a successful device, for the invaluable discussions and most importantly, building the base for this whole research during my first year.*

***Dr. Kareekunnan Afsal** and **Dr. Ahmed Hammam**, for taking my hardships as their own, for hours of discussions that more often than not produced wonderful ideas and for every new thing I learned about physics from them over cups of coffee.*

***Dr. Fayong Liu**, for his co-operation, support and lending his expertise to establish the measurement system that brought this entire work into fruition.*

***Mr. Shinichi Ogawa** and **Mr. Tomohiko Ijima**, for their relentless support in the HIM lab in AIST, providing me every technical assistance to conduct necessary experimentation and their genuine curiosity, concern and sincerity towards this project.*

***Guenter Ellrott**, for introducing Optical Lithography that improved my fabrication scheme significantly, for creating an uplifting environment in the lab and for being an insightful physicist slash friend.*

***Dr. Sankar Ramaraj** and **Dr. Amit Banerjee** for their kindness and actively participating in adding valuable comments to my manuscript.*

***My fellow lab mates** and **Ms. Reiko Seki**, for their cooperation throughout the entire time to complete this work.*

***Marlou** and **Shofi**, for being the ever-understanding roommates during the tough period of writing the dissertation.*

***My parents** for their love, encouragement, motivation and tolerance while I bombarded them with untimely phone calls, and **my younger sister**, for demonstrating the value of hard work and encouraging me everyday.*

Mayeesha M. Haque.

Table of Contents

Chapter 1	13
Introduction.....	13
1.1. Motivation of this work.....	14
1.2 Aim of the thesis.....	16
Chapter 2	19
Background	19
2.1 Thermal management of devices	19
2.2 Thermal transport in materials	20
2.3 Phonon transport in nanoscale.....	23
2.3 The coordinate system and lattice structure of graphene.....	24
2.4 Phonons in graphene	26
2.5 Thermal rectification	28
Chapter 3	30
Thermal transport in graphene: FEM simulation.....	30
3.1 The finite element method (FEM)	31
2.2 Simulation in 2D module.....	34
3.4 Simulation in 3D module.....	38
Summary	50
Chapter 4	52
Experimental method: Device fabrication.....	52
4.1 Preparation of the sample substrate	54
4.2 Transferring CVD graphene on the substrate.....	55
4.3 Device fabrication.....	56
4.3.a Fabrication of metal contacts on the sample	57
4.3.b Fabrication of the electrodes	59
4.3.c Patterning of the GNR.....	62
4.3.d Suspension and nanopatterning of the GNR.....	64
Chapter 5	70
Measurement and thermal characterization.....	70
5.1 Measurement method overview	71
5.2 Effect of Joule heating on metal electrodes.....	73
5.3 Measurement setup	76
5.4 Thermal characterization.....	80

5.4.1 Calibration of reference electrode	80
5.4 Thermal characteristics of half-meshed GNM	83
5.4 Discussion.....	86
Chapter 6	91
Conclusion and future tasks	91
6.1 Conclusion	91
6.2 Future work.....	92
Appendix	95
Development of heat spreader method for thermal characterization.....	95
A-1 experimental setup for the thermal measurement	95
A-2 Measurement of thermal transport in supported graphene	97
A-3 measurement of thermal conductivity of supported graphene	105
A-4 Extension towards suspended graphene.....	106
Bibliography	108
List of publications	115
Academic journals	115
International conferences (in chronological order)	115

List of Figures

Figure 1-1	<i>The phononic spectrum [4]</i>	14
Figure 1-2	<i>2D Examples of phononic crystals at different dimensional periodicities ranging from centimeter, micrometer and nanometer range from left to right for controlling sound, hypersound and heat respectively [7]</i>	15
Figure 2-1	<i>Spectra of acoustic and vibrational i.e. mechanical and thermal wavelength regime. [4]</i>	23
Figure 2-2	<i>Different types of motions of the atoms in the unit cell.</i>	24
Figure 2-3	<i>a) A schematic of graphene lattice is shown with hexagonal unit cell and basis vectors a_1 and a_2. The space vectors are represented by δ_1, δ_2, and δ_3 that are connecting the sub-lattices A and B The light grey rhombus represents the primitive unit cell. b) First Brillouin zone with reciprocal lattice vectors b_1 and b_2 is shown, enunciating the high symmetry points Γ, K and M. Recreated based on various references.</i>	25
Figure 2-4	<i>The phonon dispersion of graphene. [15]</i>	26
Figure 2-5	<i>Thermal conductivity of various carbon allotropes [24].</i>	28
Figure 2-6	<i>Thermal rectification mechanism with two materials with different thermal conductivities joined together [25]</i>	29
Figure 3-1	<i>Basic steps to perform FEA in COMSOL Multiphysics. Recreated from various references.</i>	31
Figure 3-2	<i>Schematic of the basic 1D, 2D and 3D finite elements</i>	32
Figure 3-3	<i>Schematic of the discretization process in COMSOL. The function u showed by the solid blue line shows approximated values to u_h represented by the red dashed line. The linear basis functions are shown by the solid black line. https://www.comsol.jp/multiphysics/finite-element-method)</i>	33
Figure 3-4	<i>Schematic of the model with square shaped nanopores in GNR</i>	36
Figure 3-5	<i>Transmission spectra of a 2D phononic crystal model</i>	37
Figure 3-6	<i>The range of phononic bandgap generated in GnPC with circular shaped pores with the pitch varied from 10-18 nm.</i>	37
Figure 3-7	<i>The comparison of PnBG ranges for GnPC with square and circular shaped pores at different pitch.</i>	38
Figure 3-8	<i>Schematic representation of the model showing the neck, pitch and the diameter of the nanopores (top). Arrows pointing towards the respective pairs of boundary conditions (bottom)</i>	39
Figure 3-9	<i>Calculated dispersion relation for GnPC with 6 nm pitch and varying radius. The change in radius also corresponds to the change in porosity. The figure numbers (a), (b) and (c) correspond to the dimensions as described in table 2.1. As the porosity is increased, a PnBG around 4THz is opened for this case.</i>	41
Figure 3-10	<i>Calculated dispersion relation for GnPC with 7, 20 and 25 nm pitch and varying radius. The change in radius also corresponds to the change in porosity. The figure numbers (a), (b) and (c) correspond to the dimensions as described in table 2.2.</i>	42
Figure 3-11	<i>Different PnC models constructed for the simulation in 3D module.</i>	42
Figure 3-12	<i>Calculated phonon dispersion relations for graphene phononic crystals with circular, square and cross shaped nanopore structures from left to right. A porosity of 28%, 25 nm pitch and 1 nm thickness was maintained for all of the studies.</i>	43
Figure 3-13	<i>Effect of neck length on PnBG with porosity maintained at 28%, thickness 1 nm and pitch 25 nm for all of the models. From left to right, neck length was 10 nm, 5 nm and 1 nm gradually. The PnBG is observed to be dependent on the neck length and with smaller neck length, PnBG is more obvious.</i>	44
Figure 3-14	<i>PnBG map for different w/p ratios. The first and second PnBG are observed for the pitches 25 nm and 20 nm.</i>	44

Figure 3-15	<i>(a) Schematic representation of the unit cell of the hexagonal snow-flake phononic crystal. L and W are the length and width of the neck of the snow-flake structure. (b) Supercell of the snow-flake phononic crystal formed when the unit cell shown in (a) is repeated in both the x and y directions. The periodicity P represents the distance between the centres of two snow-flake nanopores and is fixed to be 25 nm throughout the calculation. (c) Schematic diagram showing the Brillouin zone of the hexagonal lattice. The shaded region $\Gamma \rightarrow K \rightarrow M \rightarrow \Gamma$ represents the path along which the phononic band structure calculation is performed. (d) The phononic band structure calculated for snow-flake structure with neck length 5.2 nm showing the bandgaps in the THz regime which is desired for room temperature thermoelectric applications.</i>	46
Figure 3-16	<i>Phononic band structure calculated along the high symmetry points of the Brillouin zone for neck lengths (a) 6.6 nm, (b) 7.6 nm, (c) 8 nm and (d) 9.2 nm of the snow-flake shaped phononic crystal.</i>	47
Figure 3-17	<i>The phononic bandgap map which depicts the band gaps plotted as a function of frequency for various neck lengths of the snow-flake phononic crystal. The neck-length is continuously varied from 2 nm to 11 nm. Different colours indicate different phononic band gaps appearing between two particular bands</i>	49
Figure 3-18	<i>The transmission probability calculated as a function of phonon frequency for the snow-flake shaped phononic crystal having neck length of 8 nm. The portion of the spectrum with zero transmission probability represents the phononic band gaps in the band structure calculation. The inset shows the pressure map, which analyses the transmission of the phonons with particular frequency through the snow-flake phononic crystal. The pressure map for phononic frequencies of 0.3 THz, 0.6 THz and 1.75 THz are shown.</i>	50
Figure 4-1	<i>The allotropes of carbon: a) diamond, b) graphite, c) lonsdaleite, d) C60 buckminsterfullerene, e) C540, Fullerite f) C70, g) amorphous carbon, and h) single-walled carbon nanotube. [From Wikipedia]</i>	52
Figure 4-2	<i>Illustration of the process of scotch-tape based mechanical exfoliation method. [8]</i>	53
Figure 4-3	<i>Schematic of a CVD growth chamber [11]</i>	54
Figure 4-4	<i>(a) and (b) images of CVD graphene sample from Graphene Platform. (c) A Raman spectrum of our CVD samples provided by the company.</i>	56
Figure 4-5	<i>Schematic of the GNM device used for thermal characterization.</i>	56
Figure 4-6	<i>Flow chart of EBL lift-off technique for metal deposition and the significance of using MMA/PMMA bilayer resist.</i>	57
Figure 4-7	<i>Fabrication of mask pattern for metal contacts (a) The process of obtaining the metal contacts by lithography and liftoff is shown. (b) the mask pattern of the original sample prepared in AUTOCAD. (c) the pattern for large contact pads after development. (d) comparison of resolution at the center of the pattern. The metal electrodes for thermal sensing will be patterned in this area along with GNR.</i>	58
Figure 4-8	<i>On the left, the high resolution center pattern is shown after optical lithography and development. ON the right, the same sample is shown after metal deposition.</i>	61
Figure 4-9	<i>Dose test results for negative ARN resist. The patterns here have a minimum resolution of 250 nm.</i>	63
Figure 4-10	<i>Schematic of the GNR patterning and suspension process. Bottom: SEM image of the Patterned and suspended GNR with 400 nm x 600 nm dimension.</i>	63
Figure 4-11	<i>Layout for the sample used to develop the suspension process of GNR. on the left, the layout of the entire chip. On the right, the schematic representation of a single device.</i>	64
Figure 4-12	<i>The fabricated sample for developing the suspension and patterning process.</i>	65

Figure 4-13	<i>SEM micrographs of the fabricated samples.</i>	65
Figure 4-14	<i>The process of HIBM milling on suspended graphene sample and the first attempt at milling shows a GNR milled at different ion doses.</i>	66
Figure 4-15	<i>(a) High resolution nanopores with a pitch of 12 nm are formed on large area suspended GNR. The dose was optimized. (b) Some cracks and large pores are observed in the zoomed image. These cracks are formed either due to the tensile stress and/or the Gaussian beam spot that merged the adjacent pores.</i>	67
Figure 4-16	<i>(a) Secondary microscope image of typical suspended GNM devices. (b) Magnified image of the fabricated nanopores with ~6nm diameter.</i>	68
Figure 4-17	<i>a) 100 nm wide non-meshed area maintained on the left and right edges. (b) visible cracks are observed at the edges of the device (a) as observed by secondary HIBM after milling (c) 100 nm gaps on the top and bottom, 50 nm gaps on the left and right were maintained to stabilize the meshed devices. For observation of this device, the focus was kept on the metal layer.</i>	68
Figure 5-1	<i>Schematic representation of the 4-probe electrothermal measurement.</i>	71
Figure 5-2	<i>Left: Optical microscope image of the metal electrode device. Right: Schematic of the device.</i>	72
Figure 5-3	<i>Model built with COMSOL multiphysics to quantify the joule heating effect at the gold nanowire. The bottom model was built as a supporting model to understand the thermal concentration at the bending point of the constriction.</i>	74
Figure 5-4	<i>The joule heating effect is centered at the small constriction of the metal conductor.</i>	76
Figure 5-5	<i>Left: the schematic of the device structure for 4-probe measurement. Right: actual measurement setup.</i>	77
Figure 5-6	<i>Schematic representation of the GNM device.</i>	77
Figure 5-7	<i>Fabricated suspended GNM structure with non-meshed edges.</i>	78
Figure 5-8	<i>(a) The milling area of a GNM with 25 nm pitch before milling. Imaging was not done after milling to keep the device integrity (b) At a fixed $VD = 5$ mV at a base temperature of 300 K, $ID \sim VBG$ plot is shown for the device shown in (a). (c) At a constant base temperature of 300 K and zero backgate voltage VBG, linear $ID \sim VD$ relationship is observed.</i>	78
Figure 5-9	<i>Left: Fabricated reference device for comparison of the CNP. 7 suspended parallel devices each with 100 nm width were fabricated for this purpose. Middle: $ID \sim VBG$ trend at a constant VD and base temperature 300 K shows average CNP appears at $VBG = 0$. Right: linear $ID \sim VD$ characteristics for $VBG = 0$ and 300 K base temperature is observed for the same device.</i>	79
Figure 5-10	<i>The characteristic linear $ID-VD$ trend observed for different GNM devices with varied pitch sizes.</i>	80
Figure 5-11	<i>Left: The characteristic linear $ID-VD$ trend observed for left side reference electrode at different base temperatures. Right: resistance of the metal electrode as a function of temperature</i>	80
Figure 5-12	<i>The $ID - VD$ characteristics of the right side reference electrode at different base temperatures. Right: resistance of the metal electrode as a function of temperature.</i>	81
Figure 5-13	<i>Left: heating characteristics of the left side metal electrode as a function of applied current. Right: temperature dependence of the metal electrode as a function of applied power</i>	82
Figure 5-14	<i>Left: heating characteristics of the right side metal electrode as a function of applied current. Right: temperature dependence of the metal electrode as a function of applied power.</i>	82
Figure 5-15	<i>Normalized temperature of the left side electrodes of 4 devices as a function of power.</i>	83

Figure 5-16	<i>Normalized temperature of the right side electrodes of 4 devices as a function of power.</i>	83
Figure 5-17	<i>SEM image of the half-meshed GNM device.</i>	84
Figure 5-18	<i>$I_d - V_d$ characteristics of half meshed GNM device as measured on the left side. Thermal dissipation is from the non-meshed side to the meshed side.</i>	84
Figure 5-19	<i>$I_d - V_d$ characteristics of half meshed GNM device as measured on the right side. Thermal dissipation is from the meshed side to the non-meshed side.</i>	85
Figure 5-20	<i>$I_d - V_d$ characteristics of half meshed GNM device with 30 nm pitch as measured on the right side. Thermal dissipation is from the non-meshed side to the meshed side.</i>	85
Figure 5-21	<i>$I_d - V_d$ characteristics of half meshed GNM device with 30 nm pitch as measured on the left side. Thermal dissipation is from the meshed side to the non- meshed side.</i>	86
Figure 5-22	<i>Heating characteristics of the half-meshed device with 20 nm pitch. By extracting the heating data for the left and right side of the half-meshed device, a difference in thermal transport is detected.</i>	87
Figure 5-23	<i>Heating characteristics of the half-meshed device with 30 nm pitch. By extracting the heating data for the left and right side of the half-meshed device, a difference in thermal transport is detected.</i>	87
Figure 5-24	<i>Heating characteristics of the fully-meshed device with 20 nm pitch. By extracting the heating data for the left and right side of the full-meshed device, the difference in thermal transport is negligible</i>	88
Figure 5-25	<i>Heating characteristics of the fully-meshed device with 25 nm pitch. By extracting the heating data for the left and right side of the full meshed device, the difference in thermal transport is negligible</i>	88
Figure 5-26	<i>Trend of thermal asymmetry observed in the fabricated GPnCs. The thermal transport is observed to be lower when the heater position is on the pristine graphene side of the fabricated GPnC compared to when the heater position is changed to the meshed side of the fabricated GPnC.</i>	89
Figure 6-1	<i>Schematic representation of the device fabrication process with hBN as an electrically insulating thermal conduction layer</i>	93
Figure A-1	<i>Schematic representation of the 4-probe electrothermal measurement</i>	97
Figure A-2	<i>Increase of resistance at the metal conductor with increasing temperature of the substrate.</i>	98
Figure A-3	<i>Increase of resistance at the metal electrode with increasing temperature of the substrate. The calculated value of TCR is in well agreement with literature.</i>	99
Figure A-4	<i>Calculated temperature at the electrode with respect to applied current.</i>	100
Figure A-5	<i>Possible combinations of heater and sensor on the device.</i>	101
Figure A-6	<i>On the left, the established circuit for thermal measurement is shown. On the right the temperature rise at the electrode with respect to the applied current</i>	101

is shown.

- Figure A-7** *Change in temperature at the sensor is observed due to the change in temperature at the heater. The temperature change at the heater is induced by the applied current.* **103**
- Figure A-8** *The thermal transport through graphene is shown here for two different pairs of electrodes. Both pairs have the same distance between them. The temperature dependence at the sensors for both cases show fairly similar characteristics with respect to the applied current.* **103**
- Figure A-9** *The thermal transport through graphene at different distance from the heat source is observed. The plot shows clear dependence of thermal transport on distance from the heat source. The electrode that is closer to the heater exhibits higher heat transport trait compared to the electrode further from the source.* **104**
- Figure A-10** *Calculated thermal conductivity of supported graphene (a) considering total thickness to be 500.3315 nm, (b) considering only the thickness of graphene as 0.3315 nm.* **105**
- Figure A-11** *The highest calculated temperature obtainable with suspended gold heater was about 153.75 K.* **106**
- Figure A-12** *The highest calculated temperature obtainable with suspended gold heater was about 153.75 K.* **107**

LIST OF TABLES

Table 2.1: Parameter for the 2D phononic crystal models

Table 2.2: Parameter for the 3D phononic crystal model for circular nanopores.

Table 2.3: Parameter for the 3D phononic crystal model for circular nanopores.

Table 3.3: Tabulated PnBG widths.

Table 4.1: Average misalignment while combining MLA and EBL

Table 4.2 Dose test for ARN

Table 5.1: Simulated result of temperature at the metal constriction due to applying current

Chapter 1

Introduction

Since Moore's prediction back in 1965 stating that the number of transistors in a dense integrated circuit (IC) doubles every two years resulted in a projection of a historical trend. In the same paper, the question was arisen, "will it be possible to remove the heat generated by tens of thousands of components in a single silicon chip?" [1] Decades later, now, designing CPUs that perform tasks efficiently without overheating is a major challenge and matter of consideration for manufacturers to date. Advanced industrial field of electronics is now dealing with significant increase in density integration, clock rate and the miniaturizing of modern electronic devices, resulting in heat flux dissipation in chip level. And it has now become relevant to reflect on the ever-growing problem of management of waste heat energy. At the same time, it goes without saying that the interesting physical phenomena that manifests due to the scaling down of the devices to nanoscale can now be observed. Of course, reducing the power supply voltage is one obvious way to reduce the heat dissipation in nanoscale. But ICs that are not actively cooled operate at a temperature of 100 °C and dissipate heat at room temperature [2]. Besides, the power dissipated from a square unit area of an IC is approximately the product of the device density, energy dissipated and the number of operation per second per device. Hence, the removable power that can be taken away from the device is limited by the thermal conductivity of the circuit material and the environment. Despite the extraordinary development in the silicon industry for the past few decades, the modern silicon transistors are still over >1000x more energy inefficient than fundamental physical limits [3]. From here, it is relevant to have an insight into the molecular concept of heat, which is essentially the kinetic energy of atoms and molecules. When we say heat travels from the hot region to the cold region, i.e. in the opposite direction of a temperature gradient, it is a depiction of heat flowing from the high internal energy region to low internal energy region. Another thing that needs to come to consideration is increasing the efficiency of energy conversion modules, like thermoelectric (TE) modules and thermal rectification. Thermal rectification is very important for controlling heat currents, as recently the research in this field suggests. This thesis documents the work carried out by the author in close collaboration with Dr.

Fayong Liu for deploying the necessary experiments and Dr. Manoharan Muruganathan for the simulations in understanding and demonstrating thermal rectification characteristics in suspended graphene phononic crystals.

1.1. Motivation of this work

Phonons are considered to be the mechanical counterpart of photons and defined as the quanta of crystal lattice vibrations, in other words, zero-spin bosonic quanta of excitations generated from the simple harmonic oscillations of atoms in crystalline solids. While we have achieved remarkable control over photons and electrons, for futuristic device applications, similar control over phonons would be considered equally valuable. Maldovan presents the phononic spectrum as shown in figure-1, which shows the frequency range of acoustic phonons for sound and heat transport [4].

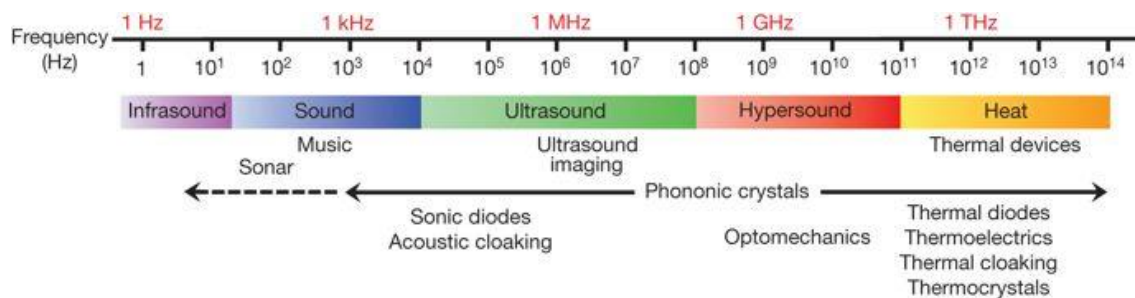


Figure 1-1 The phononic spectrum [4].

From the figure, we can see that the sound waves oscillate at low frequencies in KHz regime, while the heat vibrations oscillate at high frequencies in the THz regime. It is also significant to note that the heat waves would travel shorter lengths than the sound waves, which is why the manipulation and control of sound and heat propagation have different strategic approaches. The propagation and control of KHz to MHz sounds waves have been made possible by creating phononic crystals, which is roughly defined as periodic artificial structures comprising of two materials with different elasticities [5], [6]. With the advent of nanofabrication methods, recently, the fabrication of small scale periodic structures have been created with periodicities smaller than 1 μm to control THz phonon frequencies [7], [8], [9] From reference 7, phononic crystals with different periodicities are shown in fig. 1.2 to give an idea about the different dimensions required to manipulate phonons in different frequency regime. One of the intriguing aspects of

nanofabrication methods would be to fabricate device dimensionalities that can provide unidirectional transmission of heat. Of course, this is a difficult task to achieve, but experimental concepts has been demonstrated to show that heat flows unidirectionally, and even extended to provide ideas for implementation for digital electronic circuits like thermal transistors and thermal logic gates [10], [11]

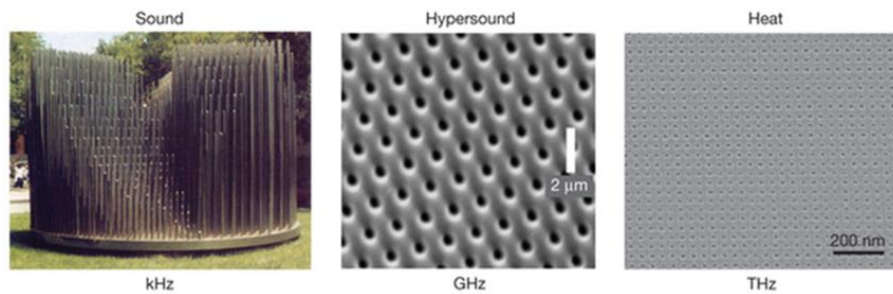


Figure 1-2 2D Examples of phononic crystals at different dimensional periodicities ranging from centimeter, micrometer and nanometer range from left to right for controlling sound, hypersound and heat respectively [7]

The study of phonon-photon interaction have been studied for a while now with the support of Raman spectroscopy and Brillouin scattering process. The simultaneous localization of acoustic and optical waves have been reported [9], [12]–[17]. However, when it comes to proper heat management of devices, one of the more important aspects to consider is the nanoscale heat transfer.

Research on thermal rectification is very important to establish the idea of controlling current induced heat transfer. The phenomena can be described as the thermal analogue of an electrical diode. The thermal rectification effect may have quite important roles in improving thermal management of electronics and saving energy. The concept of diode in electronics is a device of system that allows the passage of current in one direction and blocks the transport in the opposite. Analogously, thermal rectification is a diode-like behavior where the quantity of the heat flux changes asymmetrically as the direction of the temperature gradient is reversed. For bulk materials, the effect is more profoundly established as the researchers have shown that thermal rectification occurs for a heterogeneous bar constructed of materials of different thermal conductivity in two segments. As of now, an actual thermal diode in application has not been reported.

The study in thermal rectification behavior involves the designing and investigating the mechanism, understanding the characteristics of thermal transport behavior in an engineered system and so on. Such studies have been performed in case of bulk materials. However, for nanoscale materials and devices, the mechanism of rectification has room for explanation as the experimental studies are limited.

1.2 Aim of the thesis

While silicon is considered an important material in semiconductor studies due to its abundance and ease of fabrication, graphene is useful providing a ground for interesting experimental explorations. But, working with monolayer graphene is also challenging due to its optical transparency and difficulties in handling. With reported tensile strength of $\sim 1\text{TPa}$, large surface area to volume ratio, low reactivity and chemical purity make it an ideal material for experimental endeavors. Also, the superior physical properties of graphene compared to that of Silicon implies that manipulation of phonon of much higher frequencies is possible in graphene for similar dimensions of nanopatterns.

Recently, the availability of various nanofabrication processes with high fidelity have allowed researchers to fabricate and observe the novel properties of familiar materials at a nanoscale. Graphene, the atomic layer of carbon atoms in a hexagonal lattice, has a high Young's modulus of $\sim 1000\text{ GPa}$ and Debye temperature of $\sim 1900\text{ K}$ [18]. Thus, the wavelength of phonons at a given temperature is greatly increased compared to other materials such as silicon. Controlling and manipulating the flow of phonons which are the particles responsible for the transmission of heat and sound through a material is of great scientific and technological interest for decades [1–10]. Earlier efforts in this regard employed structural defects such as impurities and interfaces at the atomic scale to reduce the heat flow owing to the phonon scattering, essentially reducing the phonon mean free path [11–14]. However, with the recent technological advancement in terms of nanoscale device fabrication, scientists have found that materials with an array of specially designed pores can selectively suppress the flow of phonons with certain frequencies, as they introduce interference effects leading to the formation of phononic band gaps in these materials [15, 16]. The approach of controlling and manipulating heat transport and thermal conductivity by means of the wave interference method has an immense advantage over the phonon scattering method as they allow heat flow control at the nanoscale level. Also, the range of the phononic bandgap and the desired frequency of the thermal vibrations to be suppressed can be controlled by varying the size and shape of the pores. Such materials which are engineered to control the

transmission of phonons are called Phononic Crystals (PnC) and are used in a wide range of applications such as noise and vibration attenuation, acoustic waveguides and filters. For room temperature phononic applications, it is necessary to obtain a phononic bandgap in the THz regime. Graphene gives the flexibility of fabrication with its high Young's modulus and Debye temperature. With state-of-the-art patterning techniques like electron beam lithography (EBL) and helium ion beam milling (HIBM), the possibilities are immense when it comes to graphene.

In this project, we are working to establish two things,

- The fabrication of graphene phononic crystals using helium ion beam milling (HIBM).
- By introducing asymmetry to the device, we aim to observe and study thermal rectification phenomenon in graphene phononic crystal (GnPC).

As a future prospect, we also put into consideration improving the thermal sensing methods which is discussed in Appendix A.

1.3 Outline of the thesis

In this dissertation, the prospect and scope of GnPC for inducing thermal rectification is discussed in detail through the following chapters.

Chapter 2: Background

This chapter focuses on the theoretical concepts of thermal transport in nanoscale first. Then the thermal transport properties in graphene is presented in an attempt to show the importance of the unique 2D material for our experimental purpose. Finally, an overview of literature carried out by other pioneering works is presented.

Chapter 2: Phonon transport in graphene: FEM simulation

In this chapter, we studied by finite element method (FEM) the phonon transport characteristics in graphene. In a continuum model in both 2D and 3D module, we studied the phononic band gap by studying the transmission probability and dispersion relation obtained from eigenfrequency calculations.

Chapter 4: Experimental method: device fabrication

Taking into account the general idea obtained from the simulation, in this chapter the device fabrication process is discussed in detail. The fabrication of graphene phononic crystals involves two main techniques, a. Electron beam lithography (EBL) and b. Helium ion beam milling (HIBM). Optimization of both of these techniques is necessary to obtain large area GNR with high resolution nanopores. Fabrication of large area GNR with sub-10-nm pitch has already been

achieved. Based on this result, fabrication of graphene phononic crystal is being carried out.

Chapter 5: Measurement method: thermal characterization

The characterization of the fabricated devices was carried out in a cryogenic probe station. By varying the applied current through the metal electrodes, we measured the change in temperature at the electrode as a function of resistance. By measuring an asymmetrical device, we were able to observe thermal rectification phenomenon.

Chapter 6: Conclusion

A summary of the thesis and ideas for future plans are presented in this chapter.

Chapter 2

Background

2.1 Thermal management of devices

With the modern computational devices surpassing Moore's Law[19] it is now relevant to reflect on the ever-growing problem of management of waste heat energy. Heat is an inevitable by-product of any electronic devices. Electronic devices have many sources of heat. There are billions of transistor packed into a chip and there are extremely intricate connections made to keep these components together, all of which contribute in generating heat. Over the years, the coping mechanism to deal with this problem has been developed and evolved. To enable the controlling of the temperature and noise level of a semiconductor system by implementing innovative methods has become an increased need as the industry is responding to the consumers by offering products that are smaller and more powerful. A very basic example could be our personal computers, where overclocking requires greater cooling to prevent overheating of the chips, which reduces the computation efficiency significantly. The most straight forward, and in fact most commonly implemented, solution relies on the use of external cooling components such as highly heat conducting heat sinks and efficient heat exchangers. These essentially give of the heat into the surrounding area, effectively resulting in a decrease of energy efficiency in terms of computing power.

And as the industries are now working relentlessly on miniaturizing the chip features down to 50 nm, the crude solutions offered by macroscale heat management are not applicable anymore. As the density of integrated circuits increase within a system, this power consumption is now challenging the industry to create cutting edge technology to deal with thermal management. A term commonly used to understand a microprocessor's tendency to heat up is its thermal design power (TDP). It is a measure of maximum sustained power dissipated by the chip while driving a particular task. The evolution of processors from a 486 Intel chip to a multi-core processor shows the exponential and inevitable increase in power density needed to maintain superior computational power. And now, In the last decade, the processor power consumption has

increased from 70W to 250W, and now the transition from single-core to multi-core microprocessors are trying to address the increasing thermal management issue.

One of the ways to tackle is would be improving the design and 3-D circuit concept has come a long way since then. They hold possibilities to increase device performance and reduce the structural complexity a lot compared to the 2-D designs a lot. However, according to simulations, the real challenge is the circuit delay induced by the rise in temperature, which is about 5% with 10 °C increase in temperature. The performance is degraded by more than 30% when the temperature is doubled [20]. Another factor is to look into the thermal behavior materials in nanoscale. In semiconductors and insulators, the heat transport through materials is mainly through phonons which are quantized vibrations of atoms and are analogous to the elementary particles in many ways- including the fact that they possess a certain mean free path (MFP) like electrons. Phonon MFP can be in the range tens of nanometers to a few hundreds. So the interest now lies in using 2-D materials like graphene, that possess high electron mobility and high thermal conductivity that can lead to faster processing and high heat dissipation [21]-[25]

2.2 Thermal transport in materials

The macroscopic heat transfer is related to the thermal energy related properties of a material, such as thermal conductivity. From there, we can associate these properties to the nanoscale and atomic-level properties and phenomenon. In the macroscopic sense, heat transfer q is by means of conduction, convection and radiation. The heat flux vector, defined as the flow of every per unit of area per unit of time and expressed in units of $W\cdot m^{-2}$, is the sum of conductive q_c , convective q_u and radiative q_r heat flux.

According to the Fourier’s law of heat conduction, thermal conductivity is a property of a material that can be defined as the rate of heat flow through unit cross-sectional area of a material per unit temperature gradient under steady state conditions. The heat transfer rate across a material with an area A is given by the following equation,

$$q_c = - K A \Delta T \text{ ----- (1)}$$

Here, K and ΔT are the thermal conductivity an the temperature gradient respectively. In some materials, when T is small, K is considered to be a constant, while at wide temperature range, K is

a function of T [26].

Convective heat flux, \mathbf{q}_u is expressed with the following equation,

$$\mathbf{q}_u = \rho c_p u T \text{ ----- (2)}$$

here, ρ , c_p , u and T are material's density, specific heat capacity, thermal conductivity and temperature.

Finally, \mathbf{q}_r is equal to the photon contribution and expressed as the product of directional radiation intensity I ($W/(m^2\text{-sr-rad/s})$) dependent on the angular frequency of the photons ω , surface normal unit vector \mathbf{s} , polar angle θ and the ratio of radiant flux absorbed by a volume per unit length and received by the same volume μ .

$$\mathbf{q}_r = \mathbf{q}_{\text{photon}} = 2\pi \int_0^\infty \int_{-1}^1 s I_{ph,\omega} d\mu d\omega \text{ ----- (3)}$$

Thus, the macroscopic thermal energy entities like thermal storage, thermal transport and thermal interactions can be associated with the study of the 4 principle carriers, electrons, phonons, fluid particles and photons. Amongst these, the thermal transport due to fluid particles is associated to their kinetic energy in a liquid or gas where collisions take place between the particles. In a fluid, the collisions thus occur more often than in gases eventually having the particles to overcome all intermolecular forces and become a gas. On the other hand, photons are defined as the quantum of excitation of an electromagnetic field, i.e. the building blocks of EM radiation. What we know as the visible light is only a small fraction of the photon spectrum.

The quantum property of an EM waves is given by its energy $E_{ph} = \hbar\omega$ where \hbar is the Plank's constant. The photon also has a quantum momentum $p = \hbar k$, where κ is the wave vector and the wave number $\kappa = 2\pi/\lambda$.

Thermal conduction in solid materials has two components- K_e , which is the component due to electrical charge and K_p , which is the component due to atomic vibrations from their equilibrium positions. The total thermal conductivity of a solid material can be expressed as,

$$K = K_e + K_p \text{ ----- (3)}$$

The phonon contribution to thermal transport in metals is usually negligible. The phonons are likely to be scattered by the electrons and the electron component K_e is dominant due to the large quantity of free carriers.

In 1983, Franz and Wiedemann experimentally discovered that the ratio of the thermal conductivity K_e to the electrical conductivity σ in metals is almost the same at a certain temperature, T . This can be expressed as the following equation,

$$K_e / \sigma T = L(T) = L_0 \text{-----} (4)$$

This was later established by Lorentz that the ratio K_e/σ is proportional to the absolute temperature T and therefore, K_e/σ is a universal constant in all metals. The expression L_0 is known as the Lorenz number and only depends on the electron charge e , and Boltzmann constant k_B of a material.

$$L_0 = \frac{\pi^2}{23} \left(\frac{k_B}{e} \right)^2 = 2.45 \times 10^{-8} \text{ W}\Omega/\text{K}^2 \text{-----} (5)$$

In room temperature, L_0 values for three dimensional (3D) metals is exceptionally universal [27].

When it comes to insulators, the thermal transport is mainly due to the lattice component. The mechanism of thermal transport involves the displacement of a particular atom, which travels through the lattice instead of being localized. This gives rise to the lattice wave and results in thermal wave propagation through the material. From this, the definition of phonons comes as the quanta of excitation of normal modes of vibration. As the packing density of the semiconductor devices is increased drastically, as a result, the characteristic device length is also become reduced down to sub-100 nm range. This dimension is comparable to the mean free path (MFP) of the energy carriers, which are electrons and phonons. At this scale, continuum laws such as the Fourier's law breaks down. In the cases of semiconductor materials like silicon, where phonons conduct most of the heat through the channel, the MFP comes into play. When the heat conduction channel becomes so narrow that its length is comparable to smaller to the MFP, phonon-boundary condition becomes dominant and suppress the thermal conductance.

2.3 Phonon transport in nanoscale

Phonon transport is markedly different when the system size reduces to nanoscale. Due to the advancement in fabrication and synthesis of the devices in nanoscale, it is now important to understand the nature of phonon transport in nanostructured materials. In crystalline solid materials, the atoms oscillate around their equilibrium positions in quantized vibrations due to the temperature of the system. These quantized oscillations are defined as phonons. In fig. 2.1, different phonon wave regimes are shown.

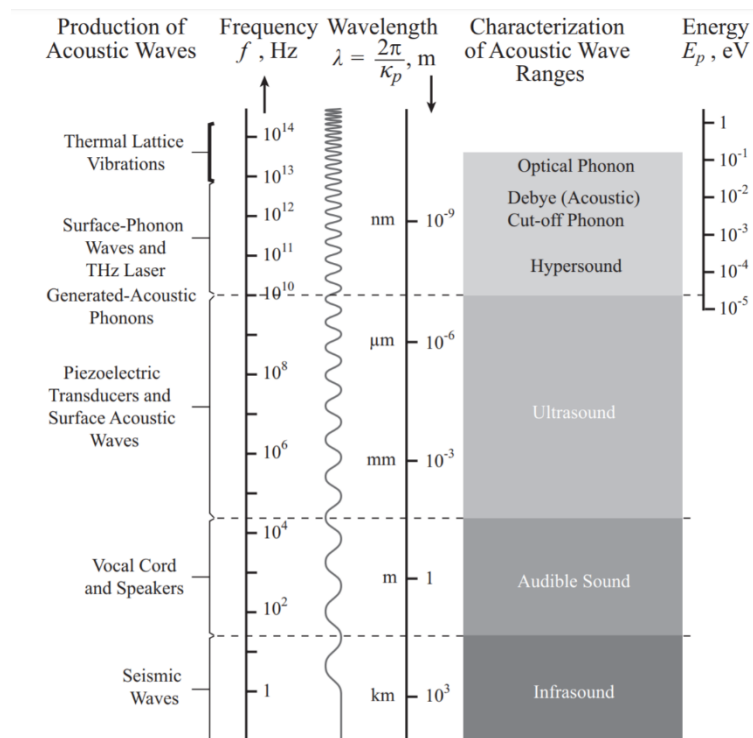


Figure 2-1 spectra of acoustic and vibrational i.e. mechanical and thermal wavelength regime. [4]

In semiconductor materials, the thermal transport is mostly dominated by phonons with large wave vector where the room temperature mean free path (MFP) can range from 1nm- 100 nm. The surface or interface phonon scattering becomes important in this regime [28] [29] [30]. At nanoscale, when the structural dimension becomes comparable to that of the phonon wavelength, other phenomena like dispersion relation modification takes place that leads to quantum confinement of phonons resulting in further alterations of the thermal transport through the material. Also, at nanoscale, the surface to volume ratio of the material increases which in turn increases the importance of boundaries and interfaces [31].

In solids, there are two types of phonons, acoustic phonons (denoted by A) and optical phonons (denoted by O). Acoustic phonons are in-phase phonons relative to the neighboring atoms, and optical phonons are the out-of-phase ones as shown schematically in fig. 2.2. Both types of these phonons disperse in Longitudinal and Transverse branches respectively, which will be shown in detail in the next sub-section of this chapter. Optical phonons have a minimum frequency even at infinite wavelength, whereas the acoustic phonon frequency approaches zero when the wavelength is infinite. Finally, there are three polarization branches for acoustic and optical phonons, one longitudinal and one transverse. In general, for N atoms per unit cell, there are 3 acoustic and $3(N-1)$ optical branches.

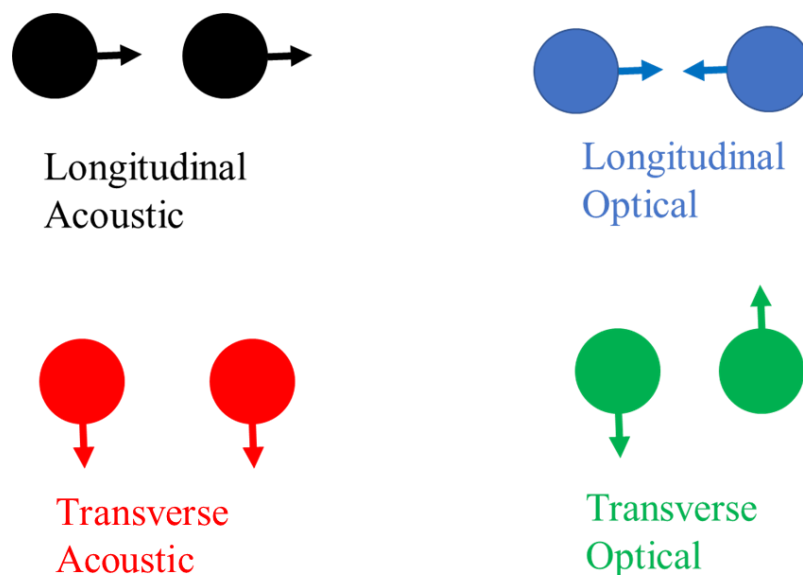


Figure 2-2 Different types of motions of the atoms in the unit cell.

2.3 The coordinate system and lattice structure of graphene

Graphene is a two-dimensional (2D) material that can be considered as a monoatomic sheet of SP² bonded carbon atoms. Graphene sheets are the building blocks for three dimensional graphite when they are weakly bonded to each other by the van der Waals force. While carbon nanotubes (CNT) was a subject of investigation for about two decades now, studies on graphene is relatively a new field. Extensive studies on graphene was only possible after it was first isolated by mechanical exfoliation from graphite on a dielectric substrate [32] [33] [34] . Besides two dimensionality, graphene is a widely sought material for its high Young's modulus, optical

transparency, and high melting temperature. These properties make graphene a perfect material to be applied in industries [35], [36].

Graphene possesses the distinguishable honeycomb structure in atomic level as shown in fig. 2.3 [37]. In the figure the lattice structure of the material is shown, as well as the interatomic distance, $a = 1.42 \text{ \AA}$. The unit cell of graphene is defined by the two lattice vectors,

$$a_1 = a \begin{pmatrix} \sqrt{3} \\ 0 \end{pmatrix} \text{----- (1) and } a_2 = \left(\frac{a}{2}\right) \begin{pmatrix} \sqrt{3} \\ 3 \end{pmatrix} \text{----- (2) [38]}$$

As we are more interested in the phonon transport through graphene, it is important to describe the reciprocal lattice vectors as below ,

$$b_1 = \left(\frac{2\pi}{a}, \frac{2\pi}{\sqrt{3}a}\right) \text{----- (3) and } b_2 = \left(\frac{2\pi}{a}, -\frac{2\pi}{\sqrt{3}a}\right) \text{----- (4)}$$

The first Brillouin zone represents a set of equivalent points in reciprocal space as shown in Fig. 2.3(b). There are six corners of the first Brillouin zone that consists of three pairs of inequivalent points K and K_0 .

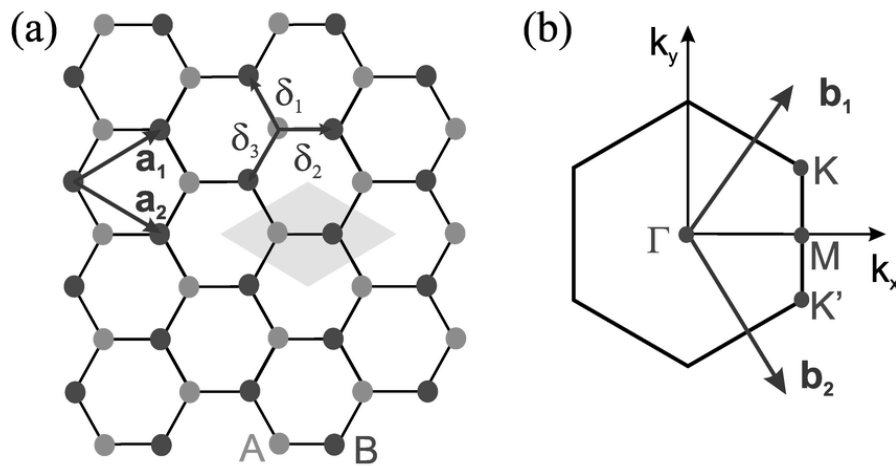


Figure 2-3 (a) A schematic of graphene lattice is shown with hexagonal unit cell and basis vectors a_1 and a_2 . The space vectors are represented by δ_1 , δ_2 , and δ_3 that are connecting the sub-lattices A and B. The light grey rhombus represents the primitive unit cell. **b)** First Brillouin zone with reciprocal lattice vectors b_1 and b_2 is shown, enunciating the high symmetry points Γ , K and M . Recreated based on various references.

By using the relations established in eq. 4 and 5, it is possible to draw the first Brillouin zone in

graphene in the reciprocal plane (K_x, k_y) as shown in fig. 1.3. The points Γ , K and M at the boundary of the Brillouin zone have the highest symmetry then the other points of the Brillouin zone. The coordinates of these space points are given by,

$$\Gamma = \left(\frac{2\pi}{a\sqrt{3}} \middle| \begin{matrix} 0 \\ 0 \end{matrix} \right), K = \left(\frac{2\pi}{a\sqrt{3}} \middle| \begin{matrix} \frac{2}{\sqrt{3}} \\ 0 \end{matrix} \right) \text{ and } M = \left(\frac{2\pi}{a\sqrt{3}} \middle| \begin{matrix} \frac{1}{2} \\ \frac{2}{\sqrt{3}} \end{matrix} \right) \text{-----(5)}$$

2.4 Phonons in graphene

The structure of graphene discussed above considers graphene as a rigid material. But at finite temperature the atoms vibrate around these equilibrium positions due to the thermal energy they have. As the atoms are still bound to the periodic lattice, the movement of one atom will be affected by the movement of the other atoms. These motions of the particles can be described by a potential, from which the equations of motions can be obtained.

The equations of motions can be obtained by Bloch's theorem. The solutions are actually the frequencies of the wavelike solutions that depend on the structure of the lattice.

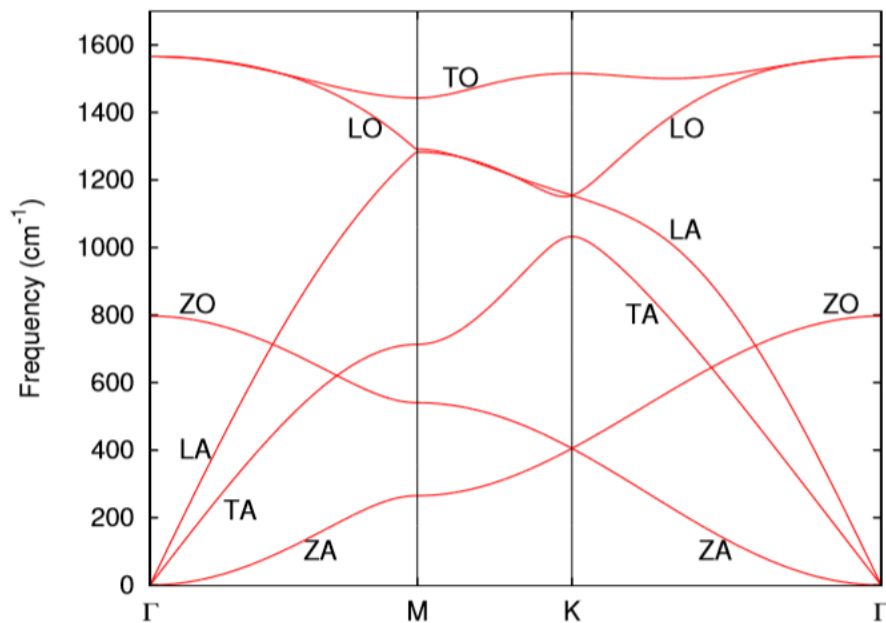


Figure 2-4 The phonon dispersion of graphene. [15]

These frequencies are the normal modes of the lattice and are described in terms of the reciprocal lattice vector given by the dispersion relation $\omega(k)$ [38]. In other words, the vibrations of these

atoms are defined by the periodic wave solutions that matches the periodicity of the lattice. The whole lattice vibrates with superposition of these normal modes, which are called phonons.

From the phonon dispersion plot in fig. 2.4 [39] we can notice the following things-

- The acoustic and optical branches typical for a two atom basis material is observed.
- We can recognize the high symmetry points at Γ , K and M as discussed in the previous section.

Thermal properties of graphene has not been explored as extensively despite intensive research on graphene for different applications. An experimental method to measure the thermal conductivity of suspended graphene flake by implementing RAMAN spectroscopy has been reported by Balandin et.al [21]. By observing the change in the position of the G-band in graphene with the change in laser power and thus inducing higher temperature, it was possible to detect the temperature rise in graphene. [21]. The measurement has room for error because even though the actual sample was supported on the SiO₂ layer, due to the weak thermal coupling between the substrate and the exfoliated graphene flake, it was assumed to be suspended. However, a more recent measurement showed that when graphene is embedded in SiO₂, the thermal resistance at the interface of the two materials is lower compared to the values measure for other carbon allotropes like carbon nanotubes [40]. Another factor to consider here is that, in the case of supported graphene, the phonon scattering between the substrate and the graphene cannot be ignored. Therefore, assuming similar values of thermal conductivity for both supported and suspended graphene could be rather misleading. Most common type of device configurations include supported graphene nowadays, however, not enough information is available regarding thermal conductivity of supported or suspended graphene. Another RAMAN spectroscopy based experimental method has been demonstrated by Freitag et. al. They had supported monolayer graphene on a 300nm thick oxide film substrate. This method is also not perfect to measure the thermal conductivity as the heat generated from the laser would travel both laterally and through cross plane and travel into the substrate. In carbon nanotubes (CNT) this value was found to be around 3500 WmK⁻¹ [34]. Fig-2.5 shows the average values of thermal conductivity of graphene allotropes as reported in various literature[33].

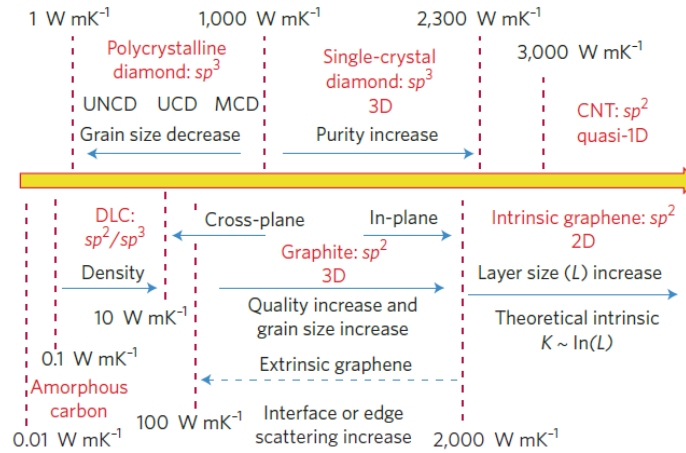


Figure 2-5 Thermal conductivity of various carbon allotropes [24].

2.5 Thermal rectification

Thermal rectification (TR) is a phenomenon analogous to the electrical transport in an electrical diode, that promotes directionally preferential heat transport. Engineered nanostructures are now being considered potential candidates to induce thermal asymmetry along with enhancing electrical transport [3]. This in fact, acts as the thermal equivalent of an electrical p-n diode. For the same temperature difference ΔT , this kind of system would allow a larger heat flux to flow in one direction and in the opposite direction it will be comparatively lower.

Thus, we can introduce the rectification ratio from the following equation,

$$\gamma_{TR}(T_0 - T) = Q_+ - Q_- \quad \text{where } Q_+ > Q_- \quad \text{and } Q_+ / Q_- > 1.$$

where T_0 , T , Q_+ and Q_- are the mean temperature, temperature between hot and cold ends, larger heat current and smaller heat current respectively [41].

It has been shown both theoretically and experimentally that thermal rectification can be achieved when two bulk materials with different thermal conductivities are joined as observed by C. Dames [42] and Kobayashi et. al.[43].

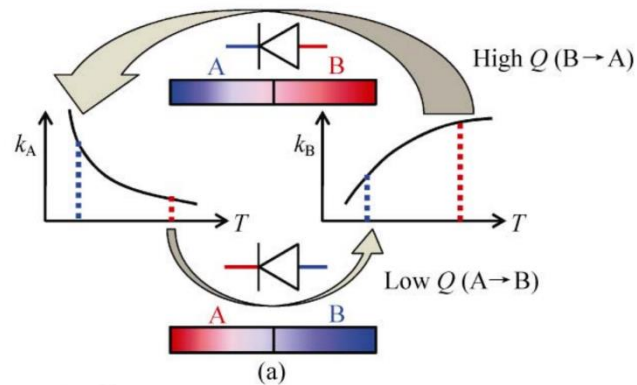


Figure 2-6 Thermal rectification mechanism with two materials with different thermal conductivities joined together [25]

The mechanism is shown in fig. 2.6 [3] two materials A and B can be subsequently used as the 'hot' and cold' terminals where, $\Delta T = (T_B - T_A)$ or $\Delta T = (T_A - T_B)$. In the first case, both materials are in a higher thermal conductivity regime and in the second case, the opposite is true. In the first case, heat flows more easily from B to A in the second case, the heat dissipation direction is from A to B. This is a demonstration of asymmetric heat flux for same ΔT .

Several promising methods have been proposed theoretically. One intriguing idea is proposed by N. Yang et. al. is the carbon nanocone. They demonstrated a thermal rectification in large temperature range from 200K to 400K by creating an indentation in graphene that preferentially scatter phonons [44]. By performing energy based deviational MC simulation, A. Arora et. al. have evaluated the thermal conductivity of restructured graphene [23]. While most of the proposal to date are theoretical studies, recently there are intriguing experimental works are being done to achieve thermal rectification in materials. C.W. Chang et. al. have achieved a thermal rectification ratio of 1.02-1.07 by fabricating unevenly mass loaded carbon or boron nitride nanotubes and observed heat flow preference from the high to the low-mass regions [45]. H. Wang et. al have achieved 26% thermal rectification factor by defect-engineering monolayer suspended graphene. The asymmetry is introduced by creating nanopores on one side of the GNR, or by creating a structured with a tapered shaped to induce asymmetry [46].

Chapter 3

Thermal transport in graphene: FEM simulation

With the recent technological advancement in terms of nanoscale device fabrication, scientists have found that materials with an array of specially designed pores can selectively suppress the flow of phonons with certain frequencies, as they introduce interference effects leading to the formation of phononic band gaps in these materials [4], [47]. The approach of controlling and manipulating heat transport and thermal conductivity by means of the wave interference method has an immense advantage over the phonon scattering method as they allow heat flow control at the nanoscale level. Also, the range of the phononic bandgap and the desired frequency of the thermal vibrations to be suppressed can be controlled by varying the size and shape of the pores. Such materials which are engineered to control the transmission of phonons are called Phononic Crystals (PnC) and are used in a wide range of applications such as noise and vibration attenuation, acoustic waveguides and filters. The emergence of two-dimensional materials which exhibit extraordinary properties has led to the quest of novel ideas and applications in these materials [48]. Amongst which, graphene, which is the first isolated two-dimensional material, is of particular interest as it showcases excellent phonon transport properties [36], [49], [50]. As mentioned earlier, phononic crystals which limit the heat flow due to the presence of an array of specially designed pores are of utmost importance from this perspective. Recently, our group has successfully nanopatterned periodic arrays of 3-4 nm sized pores on suspended graphene using focused helium ion beam milling [51]. The robustness of the focused helium ion beam milling system allows the fabrication of more complicated nanopore patterns such as cross shape, hexagonal snowflake shape with the help of a pattern generator. It has already been reported that circular periodic nanopores in graphene generate a phononic bandgap in the GHz regime [52]. The bandgap frequency is dependent on the pitch size of the pattern. With lower pitch size in the sub-10 nm regime, phononic band gaps at higher frequencies were observed. However, for potential room temperature device applications, we need to obtain the phononic bandgap in the THz regime. In this segment of the project, we tried to understand by simulation the conditioning of GnPc within the available novel nanofabrication methods to generate PnBG.

3.1 The finite element method (FEM)

Finite element method (FEM) is used widely for solving mathematical models. In analytical works, this method is widely used for structural analysis, heat flow analysis, determination of electromagnetic potential, mass transport and so on.

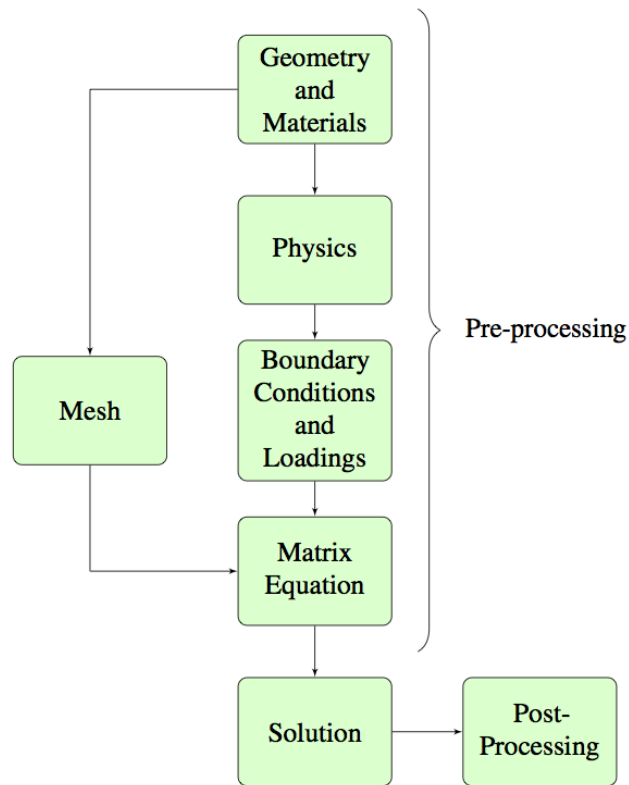


Figure 3-1 Basic steps to perform FEA in COMSOL Multiphysics. Recreated from various references.

FEM technique is a numerical analysis method for finding approximate solutions of partial differential equations. For this project, the FEM simulations were carried out using COMSOL multiphysics software (previously known as FEMLAB) which is a commercial software designed to address a wide range of physical phenomena. The software is equipped with “physics interfaces” that are pre-built packages of physical equations and corresponding boundary conditions [53].

In principle, the FEM method works by discretizing a continuous domain by a large number of subdomains. Each of these subdomains are called elements and can be defined with an unknown function represented by simple interpolation of functions with unknown coefficients. By discretization, we are basically dividing the initial boundary value problem with an infinite number of degrees of freedom into smaller segments each of which now has a smaller (finite)

number of degrees of freedom. Now, the solution of the entire problem is now an approximation of a finite number of unknown coefficients each of which now can be associated with a partial differential equation. By solving these PDEs we can generate the solution of the individual boundary value problems. An FEM analysis flow chart is shown in fig. 3.1 and the steps are discussed as follows.

Pre-processing: At first, it is necessary to build the model with the required design and dimensions. To most efficiently use the computational power within the shortest amount of time without having to compromise with the calculation accuracy, the most important step is to discretize the entire domain, say Ω . In this step, the entire domain is subdivided into a number of small domains, denoted as $(e = 1, 2, 3, \dots, M)$, where M is the total number of subdomains or elements as known otherwise. A one-dimensional domain is often discretized into elements that are straight or curved lines as shown in (fig. 3.2 (a)). These short segmented elements then interconnects to form the actual line. Elements for two and three-dimensional domains are also shown in fig. 3.2. These linear lines, triangles and tetrahedral can be taken as the basic elements for one, two and three dimensional problems where the elements form the curved lines or planer patches for the model.

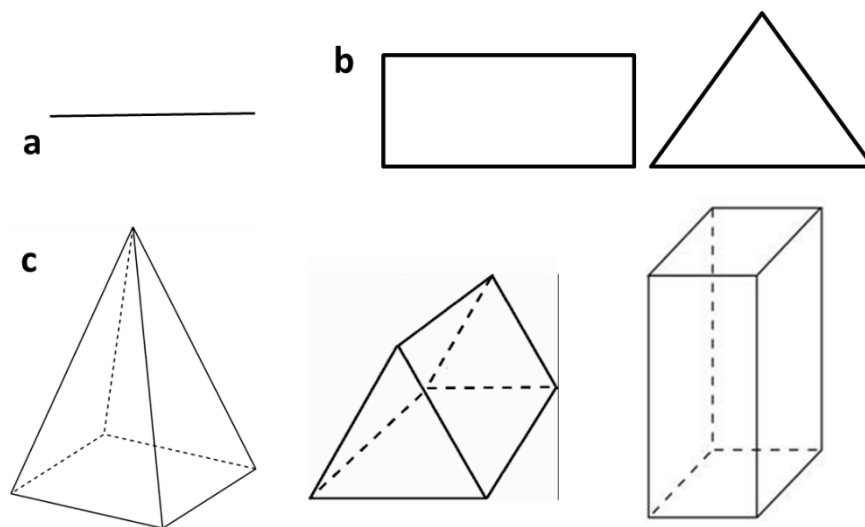


Figure 3-2 Schematic of the basic 1D, 2D and 3D finite elements.

Solution

To understand how the solution works, we can consider a one dimensional typical boundary value problem where a function u can be approximated by another function u_h according to the

following linear relation,

$$u \approx u_h \text{-----} (3.1)$$

$$\text{and, } u_h = \sum u_i \Psi_i \text{-----} (3.2)$$

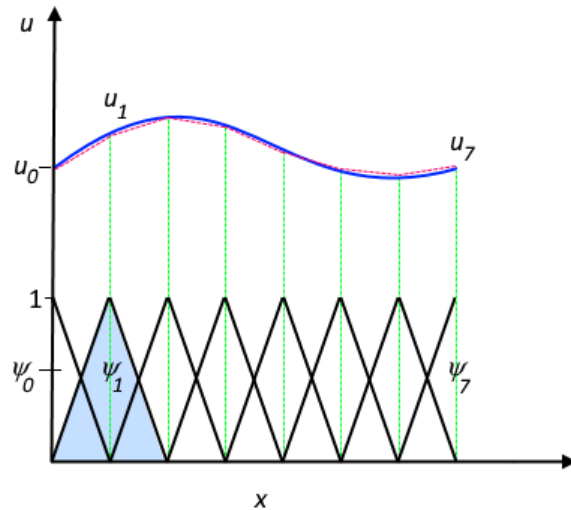


Figure 3-3 Schematic of the discretization process in COMSOL. The function u showed by the solid blue line shows approximated values to u_h represented by the red dashed line. The linear basis functions are shown by the solid black line.

<https://www.comsol.jp/multiphysics/finite-element-method>)

Fig. 3.3 [54] schematically represents an 1D problem where a rod is nonuniformly heated in the x direction. Here, Ψ_i represents the basis functions and u_i denotes the coefficients of the functions that approximate u with u_h . For a real valued problem, in the second step, the finite element analysis (FEA) selects an interpolation function that provides an approximation of the unknown solution within the element. It is usually a first, second or higher order polynomial equation. It is important to choose the interpolation function accordingly because higher order polynomials will result in more complex functions even though they are more accurate. Therefore, more simple and basic linear interpolations are usually used.

Post processing

Once the solutions of the problems are determined, the post-processing step enables the user to evaluate the results of the FEA by plotting data and exporting tools.

As mentioned before, the aim of this project is to fabricate a graphene based phononic crystal. To

be able to understand the ideal characteristics of the phononic crystal and to have an idea about the nanopattern to obtain for phononic bandgap generation, we performed numerical analysis. We used FEM simulation using COMSOL MULTIPHYSICS software [55]. Thermal phonon wavelengths are a few nanometers at room temperature and phonons quickly lose their coherence when scattered by surfaces with nanometer scale roughness [47], [56]. Therefore, the simulation model was based on the approximation of periodic nanopores on monolayer graphene. Starting with simple 2D models, the simulations were gradually improved to imitate the actual conditions as close as possible. To simulate the heat transfer in graphene we created the following models which differ from each other primarily by types of the GNR with the corresponding nanopores:

- 2D model with square shaped pores
- 2D model with circular pores
- 3D model with circular pores
- 3D model with cross shaped pores,
- 3D model with snowflake shaped pores.

In COMSOL the design of the model involves several steps that include

- 1) Geometry specification of the object
- 2) Division of the object into sub-domains, i.e. meshing,
- 3) Applying descriptions of the subdomains,
- 4) Specification of the subdomain boundaries and performing the calculation.

2.2 Simulation in 2D module

At first, we developed the model for 2D acoustic module with boundary probe conditions. The structure is considered to be infinite in y-direction and finite in the x-direction. The periodicity is considered to be a_1 and a_2 described by the two basis vectors $(a_1, 0)$ and $(0, a_2)$. According to the Floquet-Bloch theorem, if x is a position vector in the unit cell and $k = (k_x, k_y)$ is the Bloch wave vector, the relation of pressure distribution p for nodes lying on the boundary of the unit cell is,

$$p(x + a_1 + a_2) = p(x) \exp [i (k_x a_1 + k_y a_2)] \text{ ----- (3.4)}$$

The transmission probability of the phonon frequencies is shown for the model with an extremely

small pitch of 6nm. The schematic of the model is shown in fig. 3.4. Transmission probability of the phononic crystal and the associated pressure map at fixed frequencies were generated using FEM simulation. The COMSOL MULTIPHYSICS software is adopted to solve the acoustic wave propagation in the designed phononic crystal. The equation used to analyze the acoustic wave problems is expressed as,

$$(1/\rho_0 c^2) (\delta^2 p / \delta t^2) + \Delta \cdot (-\Delta p / \rho_0) = 0 \text{ ----- (3.5)}$$

This can be reduced to,

$$\Delta \cdot (-\Delta p_0 / \rho_0) - (\omega^2 p_0 / \rho_0 c^2) = 0 \text{ -----(3.6)}$$

For the two dimensional case, the model is build using the parameter described in the following table.

Table 3.1: parameters for the 2D phononic crystal model

Name	Expression	Value	Description
a1	18 [nm]	1.8E-8 m	unit cell x size
a2	a1	1.8E-8 m	unit cell y size
c0	343[m/s]	343 m/s	speed of sound
Dvisc	0.22[mm]*sqrt(100[Hz]/10[kHz])	2.2E-5 m	viscous boundary layer
Kx	0	0	wave vector x-component
Ky	0	0	wave vector y-component
L_in	5*a1	9E-8 m	inlet length
L_out	5*a1	9E-8 m	outlet length
L_pml	3*a1	5.4E-8 m	0
lambda0	c0/50[GHz]	6.86E-9 m	wavelength at 50 MHz
N	10	10	number of wave

			vector
N_layer	10	10	number of unit cells (layers) in finite model
l1	3 [nm]	3E-9 m	length of square pore
l2	3 [nm]	3E-9 m	width of square pore

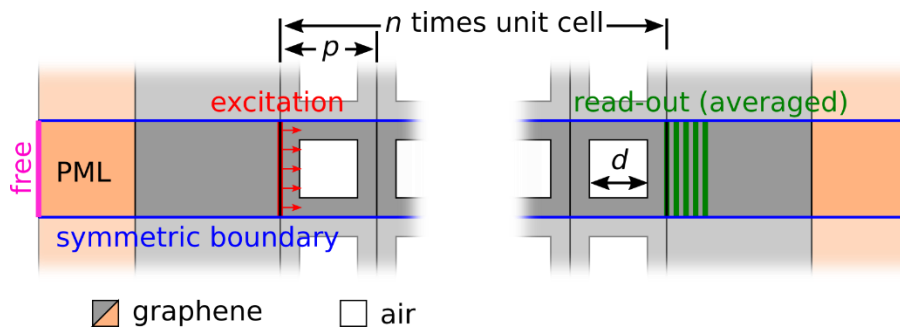


Figure 3-4 Schematic of the model with square shaped nanopores in GNR

A 2D crystal system with 10×5 crystal lattice with lattice parameter of 16 nm and a different pitch size is built in COMSOL multiphysics. The pitch is defined as the distance between the centers of two adjacent nanopores. The illustrated transmission spectra shown in fig. 2.4 shows clearly the phonon blockade at different frequencies. The illustrated pressured maps are taken at frequencies as shown below,

- 3 THz – pre Bragg gap formation
- 4 THz – Shows complete phonon blockade at the middle of the first Bragg gap
- 5.5 THz – Shows transmission after Bragg gap formation
- 6.5 THz – complete phonon blockade at the middle of the second Bragg gap
- 7 THz – shows transmission again.

From this transmission characteristics, we can see that at low THz regime, the system acts as homogeneous medium and acoustic wave propagation is through the whole material. The periodic structure doesn't affect the transmission of the acoustic waves in this regime as the lattice constant is much smaller than the wavelength. At about 6 THz, the wavelength is comparable to the length

Extending the simulation for different pitch lengths, we can obtain transmission probability at different ranges of the spectrum. In fig. 3.5, we can see the probability of PnBG generation is inversely related to the pitch length.

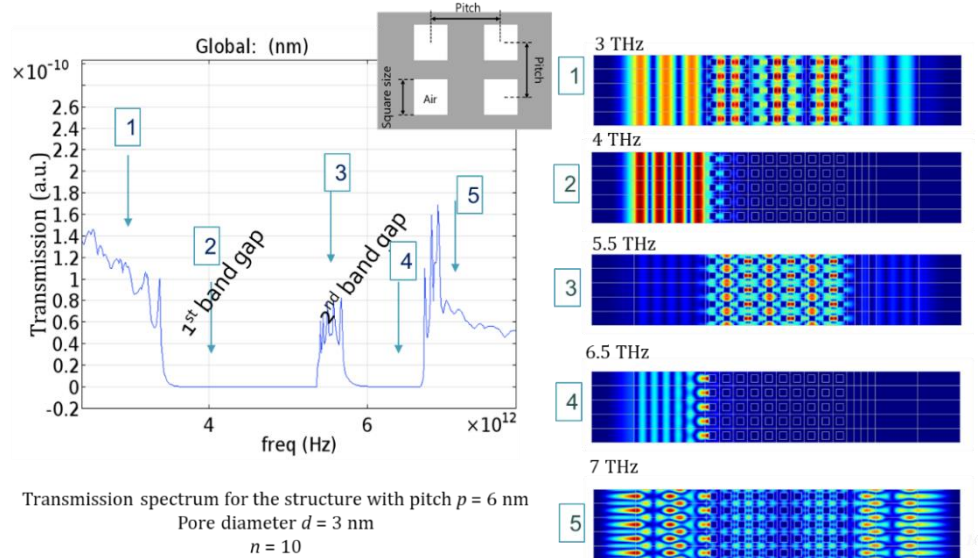


Figure 3-5 Transmission spectra of a 2D phononic crystal model

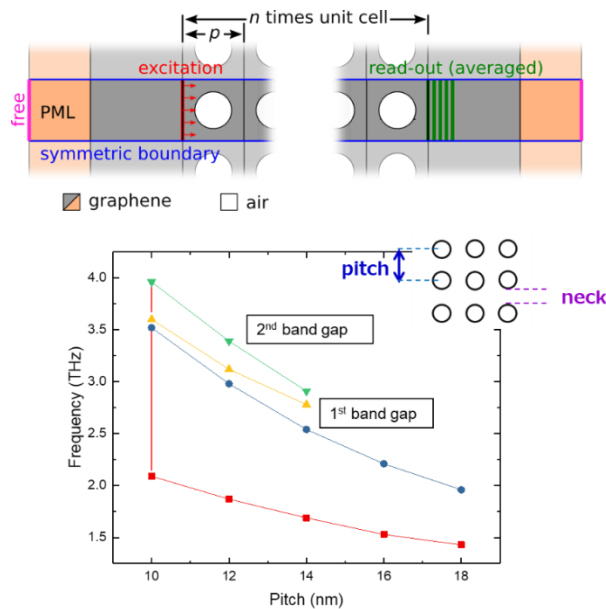


Figure 3-6 The range of phononic bandgap generated in GnPC with circular shaped pores with the pitch varied from 10-18 nm.

Next, the effect of pitch size on the bandgap width and bandgap range was studied as shown in

fig. 3.6 and 3.7. In fig 3.6, the different pitch for circular shaped pores were plotted in the x-axis for corresponding PnBG along y-axis. The effect of lattice parameter is obvious as the lower pitch contributed in opening larger bandgaps in higher THz regime. When the nanopores were square shaped, similar effects are observed and even a second bandgap is opened at sub-10-nm pitch regime. This is a very crude simulation performed in 2D module and only takes into account the unidirectional longitudinal wave transport through the lattice. In the next section, we improvise the simulation in 3D module for more accuracy based on the preliminary findings from here.

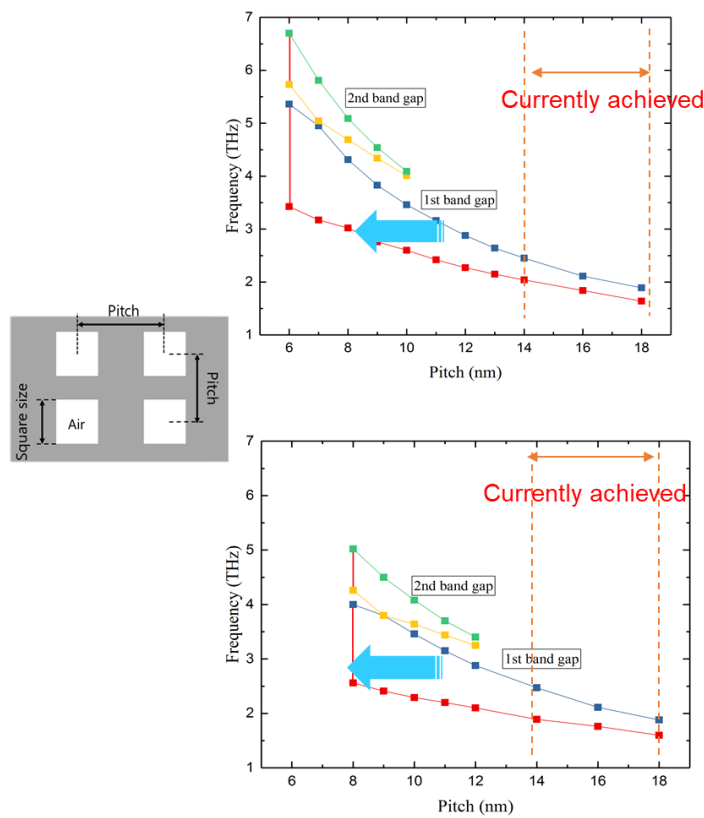


Figure 3-7 The comparison of PnBG ranges for GnPc with square and circular shaped pores at different pitch.

3.4 Simulation in 3D module

After being able to observe the significance of PnBG in terms of lattice parameter, pore shape and periodicity, the simulation was extended in the 3D module. Our colleague developed the model with the assumption of graphene with 1nm thickness to favor the meshing condition in COMSOL and performed the study for square, circular and cross shaped pores. It has been shown that while

circular and square shaped pores do not show any PnBG opening, by implementing certain dimensional conditions it was possible to observe PnBG for cross-shaped nanopores. It was observed that the PnBG depended strongly on the ratio of the width at the edge of the cross (w) to the pitch (p) of the cross. The phenomena and the possible mechanism are discussed in detail in the later sections.

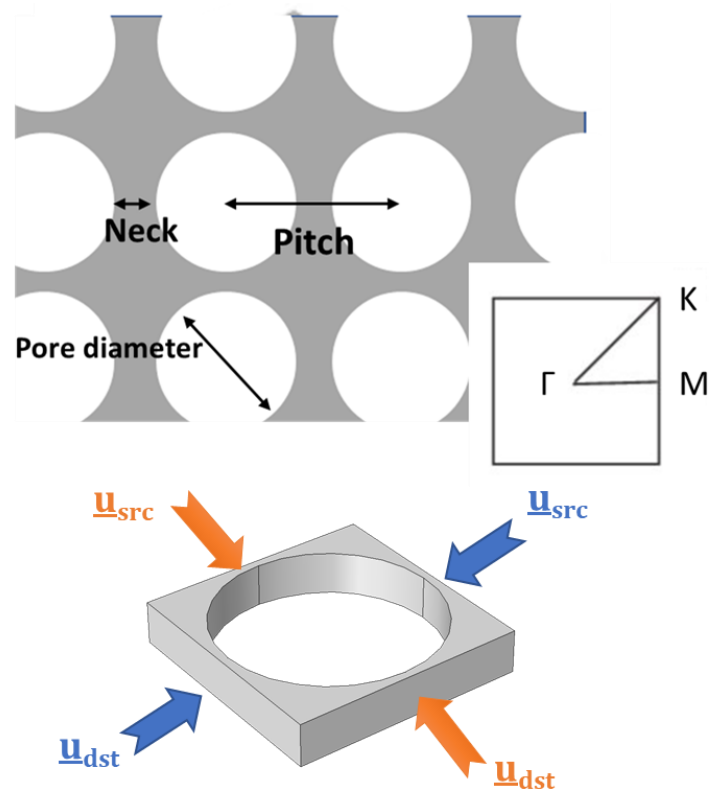


Figure 3-8 Schematic representation of the model showing the neck, pitch and the diameter of the nanopores (top). Arrows pointing towards the respective pairs of boundary conditions (bottom)

To carry out the dispersion relation between the phonon energy and the wave vector, Floquet boundary conditions are used [57]. Amongst the available application-specific modules for various physics phenomena, we made use of the acoustic module to solve the wave propagation in the phononic crystal to obtain the pressure map of the system at fixed phononic frequencies. The graphene thickness was fixed to be 1 nm to favor the meshing condition in COMSOL MULTIPHYSICS software.

In the 3D case, we first try to simulate the most common and experimentally affordable circular pore shapes. In the 2D case, the bandgap was larger at sub-10-nm pitch scale, we also constructed

our 3D models varying the pitch starting 6 nm. Then we took care to investigate the porosity favorable for PnBG opening at this lattice parameters. To study the dispersion relation, we applied Floquet boundary condition (Floquet BC) on the model as shown in fig. 3.8. For an infinite waveguide, Floquet BC is represented by the following equation.

$$\underline{u}_{dst} = \underline{u}_{src} e^{-ik_F(\underline{r}_{dst} - \underline{r}_{src})} \text{-----} (3.7)$$

Here, k_F is the Floquet wavenumber, and the subscripts dst and src represent destination and source respectively. \underline{u} is the displacement field and \underline{r} is the spatial coordinates of the boundaries on which the BC is applied.

Once the BC is applied on a representative unit cell, it would then sweep for the relevant wavenumbers while solving the eigenvalues (or eignefrequencies) at each interval defined by the user. The wavenumber and the frequency values would then build the dispersion relation curves for the periodic waveguides. Collet et. al. have shown the use of Floquet BC to obtain dispersion relation for a cylindrical rod attached to a thin plate [57].

In the following segment, I will discuss the results obtained for circular nanopores in graphene. For 6 nm pitch, we can see that the PnBG is prompted to open as the porosity is increased from 0.523 to 0.68. A PnBG around 0.4 THz regime is observed.

Table 3.2: Parameter for the 3D phononic crystal model for circular nanopores.

Pitch (unit cell length)	6 nm		
Thickness	1 nm		
Porosity	(a) 0.502	(b) 0.53	(c) 0.68
Radius	(a) 2.4	(b) 2.6 nm	(c) 2.8 nm

It is encouraging for us that the PnBG is observed for the more realistic case of GnPC. However, the unit cell dimensions at this point are extremely small and experimentally impossible to achieve. The neck length becomes ~1nm when the porosity is 0.68 which is not achievable with

the current technology. So we explore to obtain more possibilities to get as close to experimental scenario by increasing the pitch, neck length and optimizing the porosity.

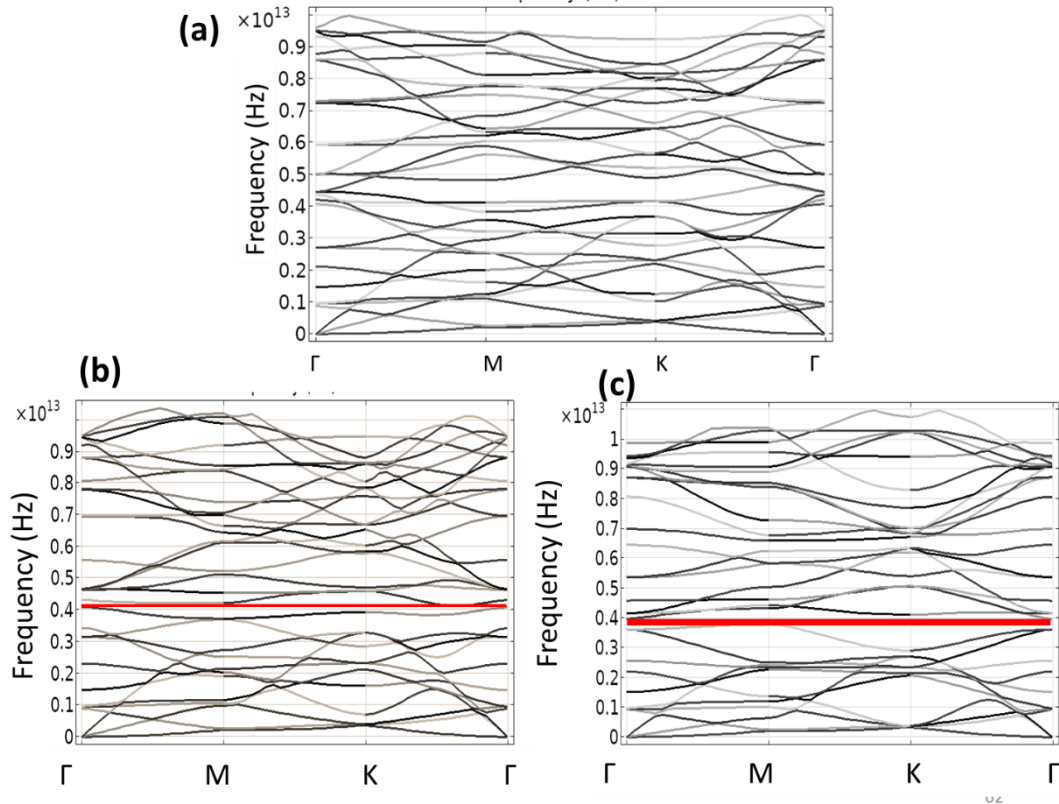


Figure 3-9 Calculated dispersion relation for GnPC with 6 nm pitch and varying radius. The change in radius also corresponds to the change in porosity. The figure numbers (a), (b) and (c) correspond to the dimensions as described in table 2.1. As the porosity is increased, a PnBG around 4THz is opened for this case.

Table 3.3: Parameter for the 3D phononic crystal model for circular nanopores.

Pitch (unit cell length)	7 nm	20 nm	25 nm
Thickness	1 nm		
Porosity	(a) 0.89	(b) 0.78	(c) 0.789
Radius	(a) 3.4 nm	(b) 9.64 nm	(c) 12.13 nm

With the dispersion relation shown in fig. 3.10, we observed that the PnBG opens when the

porosity is relatively high, even when the pitch is increased upto 25 nm. This attests to an extremely narrow neck length associated with the PnBG opening.

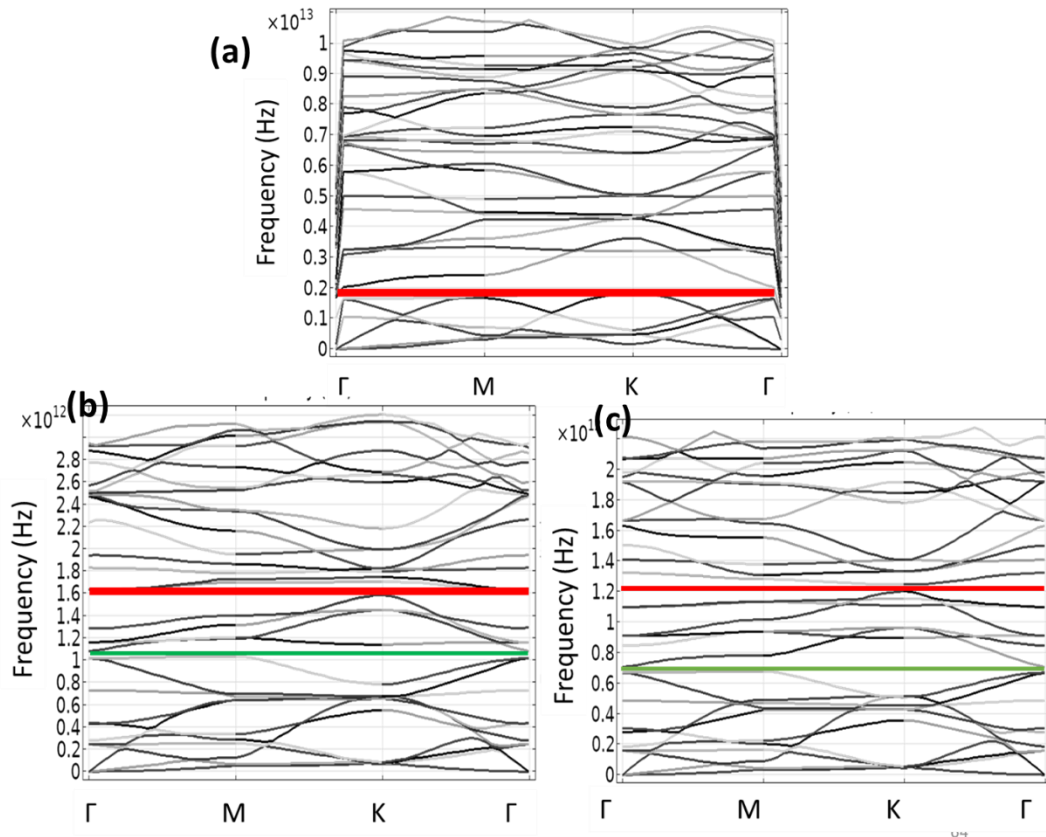


Figure 3-10 Calculated dispersion relation for GnPC with 7, 20 and 25 nm pitch and varying radius. The change in radius also corresponds to the change in porosity. The figure numbers (a), (b) and (c) correspond to the dimensions as described in table 2.2.

As shown in fig. 3.11, the pore-shape dependence of the the GNPC was studied for different models

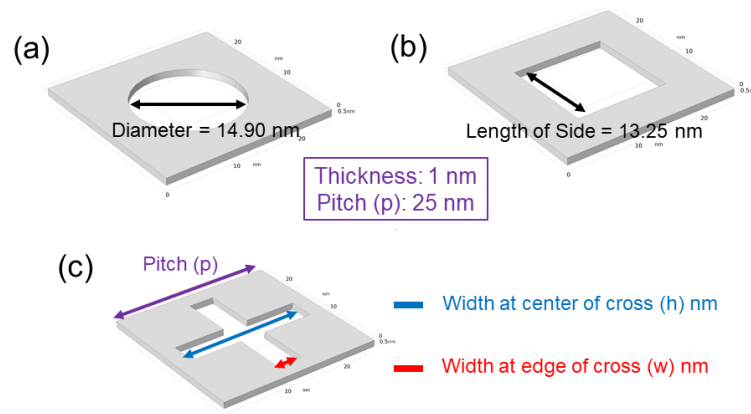


Figure 3-11 Different PnC models constructed for the simulation in 3D module.

with square, circular and cross shaped pores. This particular study is done in close collaboration with our colleague **S. Kubo**.

The porosity and pitch of the GnPC was maintained at 0.28 and 25 nm respectively. For the cross shaped structure, which is the structure of our interest, has a pitch of 25 nm, width at the center of the cross = 20 nm and width at the edge of the cross 5 nm. This gives a neck of 5 nm which is referred to as the distance between the two holes in the periodic structure. While the circular and square shaped pores didn't show any phononic band gap, the cross shaped pore exhibited multiple phononic bandgaps in 0.57 THz to 0.60 THz, 0.68 THz to 0.69 THz and 0.87 THz to 0.90 THz regions (fig. 3.12). In this simulation, the porosity, thickness and pitch of all the GPnCs are considered the same. From this, we can make the assumption that the appearance of the PnBG was influenced by the pore shape control in the graphene.

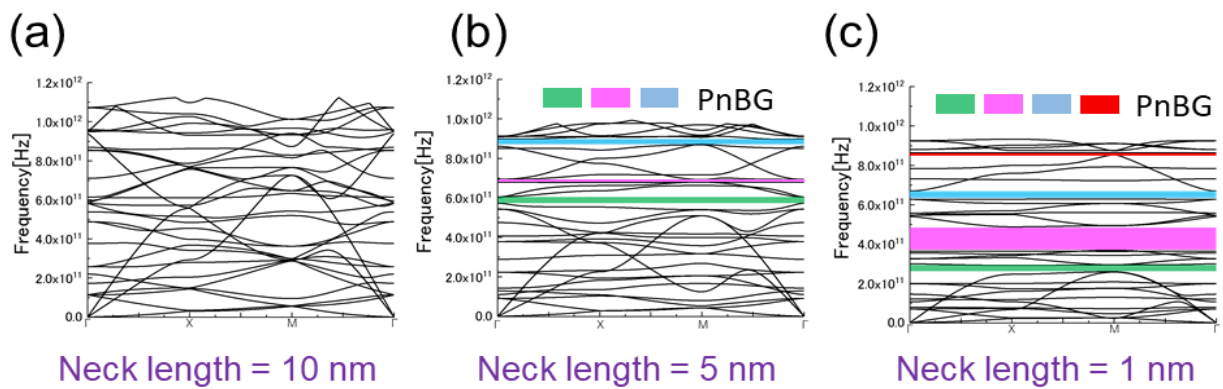


Figure 3-12 Calculated phonon dispersion relations for graphene phononic crystals with circular, square and cross shaped nanopore structures from left to right. A porosity of 28%, 25 nm pitch and 1 nm thickness was maintained for all of the studies.

To correlate the effect of pore shapes on the PnBG opening, we saw that, one important aspect of the cross-shaped hole structure that had influenced the PnBG opening was the neck length, which is defined as the distance between two corresponding pores. 28% porosity was maintained for all of the structures with varying neck length by adjusting the width at the center of the nanopores accordingly. The phonon band dispersion relations of these structures are shown in 3-12 (a)-(c). When the neck length was 10 nm, no PnBG was observed from the dispersion relation. However, the PnBG appeared and became more obvious as the neck length was gradually decreased as shown in fig. 3.12. Also, at smaller neck length conditions, we could observe multiple PnBGs. At a neck length as small as 1 nm, from the dispersion relation we could observe four different PnBG regions: green (0.26 THz to 0.29 THz), purple (0.37 THz to 0.49 THz), blue (0.63 THz to 0.67 THz),

and red (0.85 THz to 0.86 THz) compared to the case of the 5 nm neck cross structure which showed only three regions. These results show that due to the shorter neck length, the phonons are obstructed at the constriction leading to phonon confinement. The opening of PnBG is due to the interference of the phonon waves at the constriction along the length and width [58]

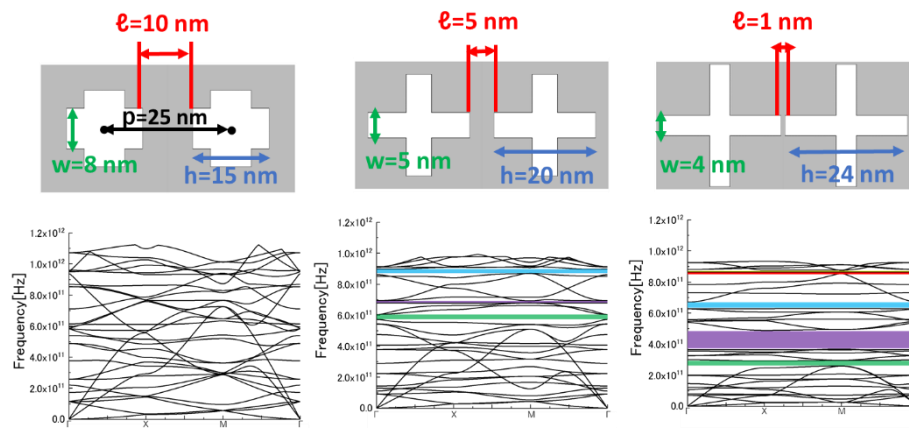


Figure 3-13 Effect of neck length on PnBG with porosity maintained at 28%, thickness 1 nm and pitch 25 nm for all of the models. From left to right, neck length was 10 nm, 5 nm and 1 nm gradually. The PnBG is observed to be dependent on the neck length and with smaller neck length, PnBG is more obvious.

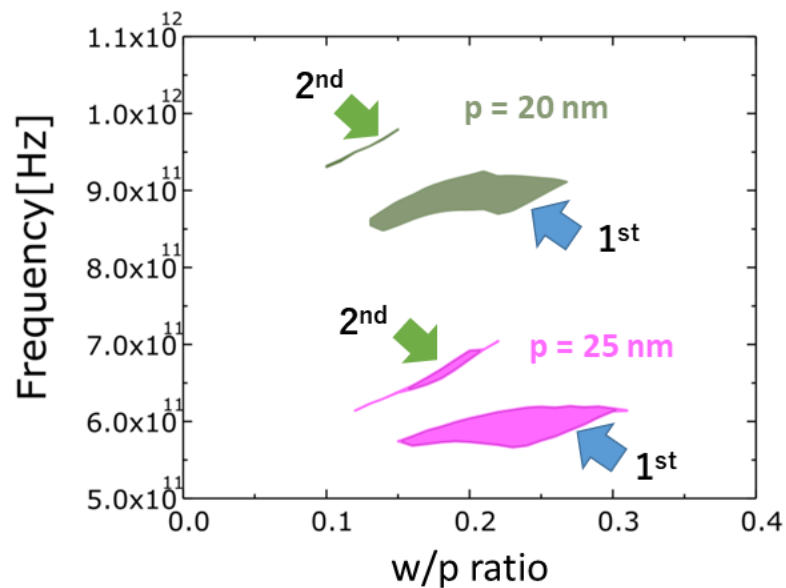


Figure 3-14 PnBG map for different w/p ratios. The first and second PnBG are observed for the pitches 25 nm and 20 nm.

From the bandgap map shown in fig. 3.14, we can observe the effect of pitch to width ratio (W/P) on the generation of PnBG. Both 20 and 25 nm pitch GpNCs show phononic bandgap opening at a

certain W/P value. Phononic bandgaps around 0.6 THz and 0.9 THz frequency regime were observed for the 25 and 20 nm pitch GPnCs respectively. With the decreasing pitch, i.e. decreasing unit cell size that resulted in increasing pore intervals, it was observed that the phonon dispersion relation shifted to higher frequency regime. Conditioning of the PnBG seems to be dependent on the w/p ratio as the bandgaps are seemingly generated at the similar w/p regions.

After realizing the importance of conditioning pore-shape size for the generation of PnBG and with the possibility with HIM milling system for the practical applications, I was further motivated to expand the previous study for a snowflake-shaped GnPC. We envisioned being able to generate high THz PnBG by introducing more complex shapes that would help increase the neck length by keeping the similar porosity. From experimental point of view, introducing a more complex shaped waveguide is not easy, but not completely a farfetched idea either. Keeping the material parameters similar as the preliminary simulation cases, this time a hexagonal snowflake shaped PnC was studied.

Fig. 3.15(a) shows the schematic representation of the unit cell of the hexagonal snow-flake phononic crystal considered in this study. According to Floquet's theorem, wave propagation through a lattice can be realized within the irreducible Brillouin zone. If we have a medium with heterogeneous elastic properties or particular geometric features, only certain waves can propagate through the structures. Each of these modes can be identified by a wave number and defined as the distribution of dispersion curves, from which it is possible to identify the frequencies that are being blocked by a certain phononic crystal system [21]. Henceforth, it becomes necessary to define a unit cell in the k -space such that the wave vectors can be expressed in terms of the reciprocal lattice basis as shown in fig-3.15 (a) for the hexagonal unit cell. The periodic nanostructure obtained by repeating the unit cell in x and y directions is shown in 1b. The periodicity of the structure is fixed to be 25 nm throughout the calculations. In this study we focus on the variations in the interference effect as we change the neck-length of the snow-flake structure. Hence we performed phononic band structure calculation for different neck-length L , along the high symmetry points of the Brillouin zone shown in Fig 3.15c. The pitch is defined by the distance between the center of two snowflakes, which is essentially the length of the unit cell itself. The study has been carried out on the minimum unit cell (fig-3.15(b)) with periodic boundary conditions which replicates the minimum unit cell in both X - and Y - directions to imitate the snowflake shaped phononic crystal. Also, several other bandgaps are seen to be formed at lower frequencies suppressing a large portion of the phonon frequency.

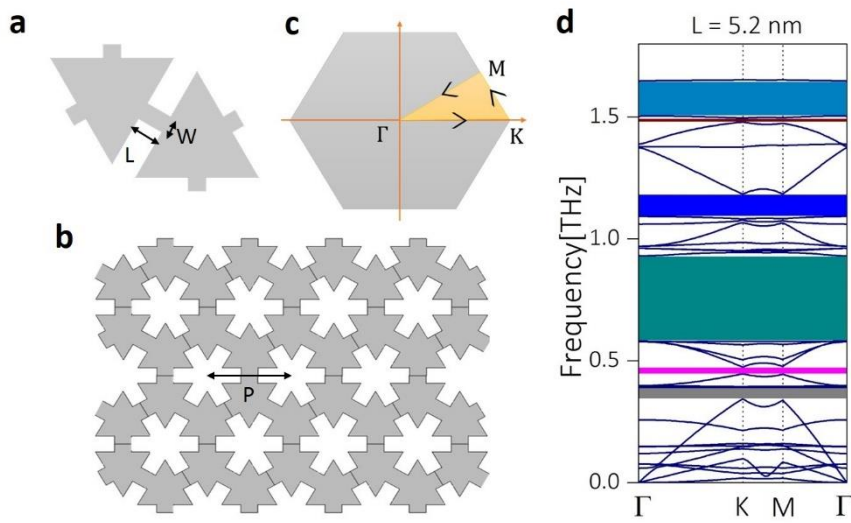


Figure 3-15 (a) Schematic representation of the unit cell of the hexagonal snow-flake phononic crystal. L and W are the length and width of the neck of the snow-flake structure. (b) Supercell of the snow-flake phononic crystal formed when the unit cell shown in (a) is repeated in both the x and y directions. The periodicity P represents the distance between the centres of two snow-flake nanopores and is fixed to be 25 nm throughout the calculation. (c) Schematic diagram showing the Brillouin zone of the hexagonal lattice. The shaded region $\Gamma \rightarrow K \rightarrow M \rightarrow \Gamma$ represents the path along which the phononic band structure calculation is performed. (d) The phononic band structure calculated for snow-flake structure with neck length 5.2 nm showing the bandgaps in the THz regime which is desired for room temperature thermoelectric applications.

The thermal conductivity in a material can be expressed with the following equation,

$$\kappa = \sum_j \int_0^{\omega_{max}} \hbar \omega_j \frac{\partial n_j}{\partial T} g_j v_j l_j d\omega \quad \text{----- (3.8)}$$

where j runs over different polarization branches of phonon, which include two transverse acoustic branches and one longitudinal acoustic branch, $\hbar \omega_j$ is the phonon energy, n_j is the occupation number, T is the temperature, g_j is the density of states, v_j is the group velocity and l_j is the mean free path of the phonon. As far as the wave interference approach towards controlling the heat transport and thermal conductivity concerned, various shapes of nanopores with different periods affect the dispersion relation of the phonon which in turn affects the propagation of phonon by changing the density of states and the group velocity. The wavelength of the phonon forbidden to propagate depends on the period of the nanopores as the interference effect follows Bragg's law, $n\lambda \approx 2a$ where λ is the phonon wavelength and a is the periodicity of the nanopores. The shape of the phononic crystal also has immense effect in introducing the thermal bandgap in these nanostructures. Fig. 3.15 (a) shows the schematic representation of the unit cell

of the hexagonal snow-flake phononic crystal considered in this study. L and W are the length and width of the neck of the snowflake structure. The periodic nanostructure obtained by repeating the unit cell in x and y directions is shown in fig. 3.15 (b). The periodicity of the structure is fixed to be 25 nm throughout the calculations. In this study we focus on the variations in the interference effect as we change the neck-length of the snow-flake structure. Hence we performed phononic band structure calculation for different neck-length L , along the high symmetry points of the Brillouin zone shown in Fig 3.15 (c) . Fig. 3.15 (d) shows the band structure calculated for the snow-flake structure which has a neck length of $L = 5.2$ nm. A phononic bandgap at higher frequency regime (~ 1.6 THz) was obtained compared to the bandgap around 0.9 THz obtained for the cross bar structure in our previous study [23]. Also, several other thermal bandgaps are formed at lower frequencies suppressing a large portion of the phonon frequency.

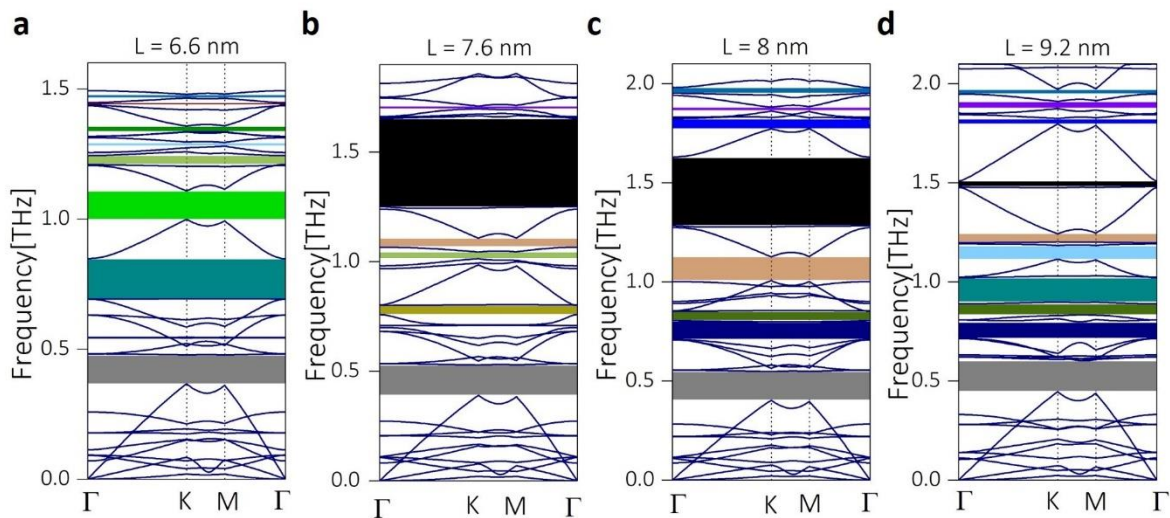


Figure 3-16 Phononic band structure calculated along the high symmetry points of the Brillouin zone for neck lengths (a) 6.6 nm, (b) 7.6 nm, (c) 8 nm and (d) 9.2 nm of the snow-flake shaped phononic crystal.

Motivated by the improvement in the thermal bandgap calculation, we carried out band structure calculations for other neck lengths. We noticed that varying the neck-length also reduces the size of the triangles in the snow-flake unit cell so as to keep the periodicity constant. This could impact the dispersion relation as the coherent interference due to the wave reflection from the triangular surfaces may change with the size of the triangle. Fig 3.16 a-d shows the phononic band structure plotted along the high symmetry points for the lengths 6.6 nm, 7.6 nm, 8 nm and 9.2 nm respectively. Compared to the large bandgap observed for $L = 5.2$ nm in Fig 3.16 d, increasing the length to 6.6 nm lowered the frequency of the bandgap and at the same time reduced the size of

bandgap (Fig 3.16 b). However, increasing the neck length further to 7.6 nm (Fig 3.16 c) brought back the large bandgap around 1.6 THz. Additionally, a small bandgap of width 14 GHz is opened around 1.7 THz (purple colour). Further increasing the neck length to 8 nm gives rise to more bands at higher phononic frequency. Also, a new bandgap is opened around 1.96 THz. Note that the large bandgap present around 1.5 THz reduced in size compared to the case of $L = 7.6$ nm. Fig 3.16 (d) shows the phononic band structure calculation for $L = 9.2$ nm, where the top band gap reduced in frequency. Also, the large bandgap around 1.5 THz became very narrow. To summarize the observation of the bandgap opening for different neck length of the phononic crystal, we tabulated the range and width of the highest bandgap for all the above-mentioned neck-lengths in table 3.4.

Table 3.4: Tabulated PnBG widths.

L	PnBG range	PnBG width
(nm)	(THz)	(GHz)
6.6	1.465 - 1.479	14
7.6	1.698 - 1.711	13
8	1.951 - 1.980	29
9.2	1.948 - 1.971	23

Although a steady increase in the frequency of the highest bandgap was observed until $L = 8$ nm, the frequency range and the width of the bandgap reduced for $L = 9.2$ nm. Thus the dependence of the bandgap opening on the length of the neck is not linear as expected. This motivated us to study the phononic band gap opening for all the possible neck lengths. Fig 3.17 shows the phononic band gap map for neck length varied from 2 nm until 11 nm. The different colours indicate different band gaps appearing between two particular bands. These colours are also matched with the colours used in Fig 3.15 d and Fig 3.16 to indicate different bands. As is evident from the bandgap map, the bandgap does not follow a linear relationship with the neck length. Moreover, some of the bands follow an oscillatory pattern where the bandgap width increases with the length, reaches a maximum and then decreases with increase in neck-length. Such a pattern can be observed especially in the case of the large hill shaped bands centring at 5 nm and 8 nm neck length (Cyan and black respectively). Also, it is noteworthy that the overall bandgap map has an oscillatory pattern which peaks at neck lengths of 5.4 nm and 8.4 nm. Such a bandgap map will help to selectively choose the parameters of the snowflake phononic crystal to suppress the thermal conductivity in the THz regime [59].

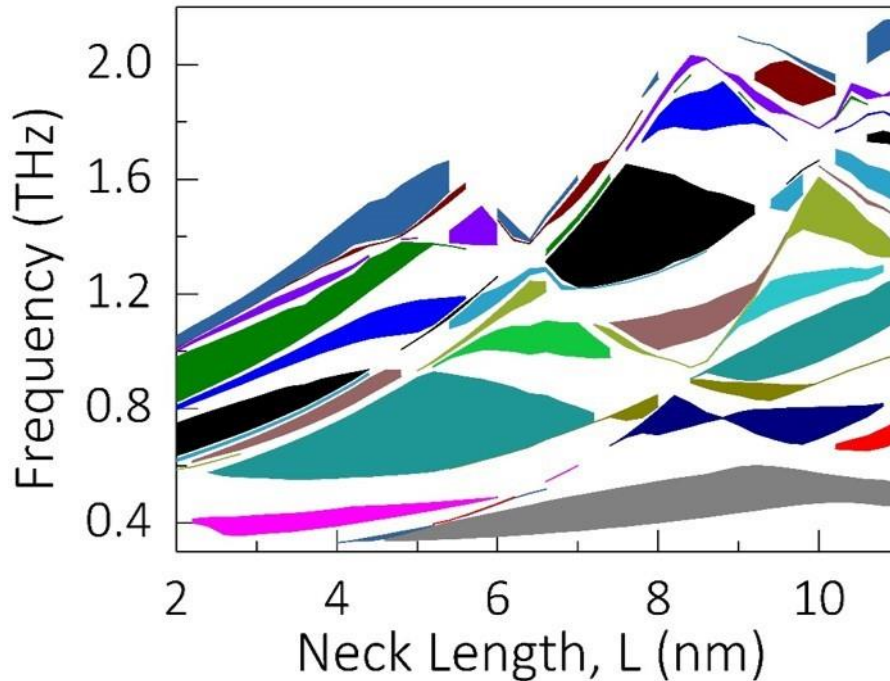


Figure 3-17 The phononic bandgap map which depicts the band gaps plotted as a function of frequency for various neck lengths of the snow-flake phononic crystal. The neck-length is continuously varied from 2 nm to 11 nm. Different colours indicate different phononic band gaps appearing between two particular bands

We have also calculated the transmission probability as a function of phonon frequency for the snow-flake shaped phononic crystal having neck length of 8 nm (Fig. 3.18). Complete suppression of frequencies around 0.7 THz, 1 THz and 1.75 THz observed in the transmission probability spectrum represents the phononic bandgaps. When compared with the phononic band structure calculated for the snow-flake structure with neck length 8 nm, an upward shift of 0.27 THz in the phonon frequency is observed in the transmission spectrum. Such a difference is expected due to the limited number of nanopores used in the transmission spectrum analysis (Fig. 3.18 inset). Also, the diffraction effects from the two edges of the snow-flake structure would have contributed to this anomaly. Nonetheless, apart from this upward shift in the frequency, the position of the bandgap and the width of the bandgap is in good agreement with the band structure calculation shown in Fig 3.16c. To confirm the propagation of phonons with certain frequency through the phononic crystal we visualized the pressure map for various frequencies in the transmission spectrum (Fig 3.18 inset). Here a pressure wave of a certain frequency is applied at the left end of the sample and visualised the transmission of the wave through the phononic crystal. The pressure map for 0.3 THz, 0.6 THz and 1.75 THz are shown in the inset of

Fig. 3.18 As for 0.3 THz, which shows high transmission probability, most parts of the wave reached the other end of the phononic crystal as expected. While for 0.6 THz frequency, which has a very small transmission probability, a small portion of the wave reached the other end. However, for 1.75 THz wave which falls in the bandgap region of the transmission spectrum, the wave is completely blocked by the phononic structure which substantiates the ability of the snow-flake nanopores in suppressing thermal conductivity.

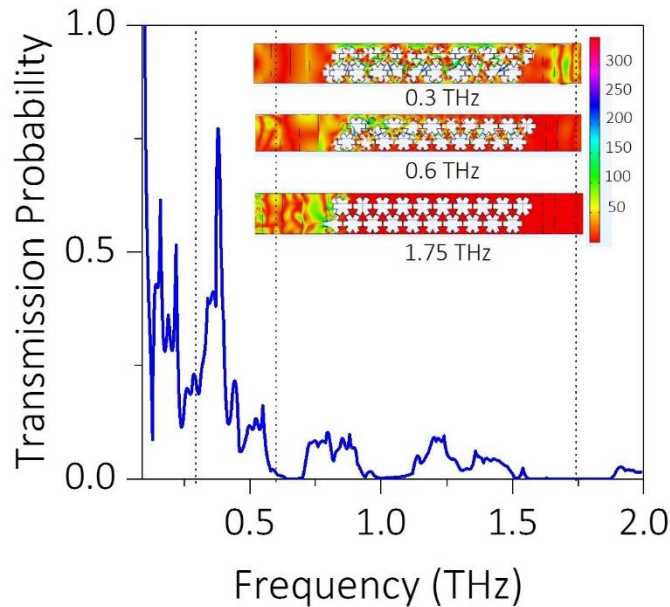


Figure 3-18 The transmission probability calculated as a function of phonon frequency for the snow-flake shaped phononic crystal having neck length of 8 nm. The portion of the spectrum with zero transmission probability represents the phononic band gaps in the band structure calculation. The inset shows the pressure map, which analyses the transmission of the phonons with particular frequency through the snow-flake phononic crystal. The pressure map for phononic frequencies of 0.3 THz, 0.6 THz and 1.75 THz are shown.

Summary

To summarize this chapter, we have investigated the thermal transport probability regulation in graphene phononic crystals in carrying conditions using FEM. As a result of the coherent interference from the snow-flake nanopores, a phononic bandgap in the THz regime was obtained which is desirable for room temperature thermoelectric applications. The size of the bandgap and its position in the phonon dispersion curve could be manipulated by varying the neck length of the snow-flake structure. A distinctive band gap map is also computed by varying the neck length of the snow-flake structure, which provides enormous information as to the size and position of

the phononic band gap at various neck length. The transmission probability calculation as a function of phonon frequency also shows good agreement with the band structure calculation. The pressure map of the phononic crystal for various frequencies having different transmission probability also validate the effectiveness of snow-flake shaped nanopores in suppressing the phonons with frequencies in the bandgap region [59]. While the much simpler pore shapes like the circular one requires high density nanopores, in the case of the more complicated shapes, the pitch dependence becomes rather crude.

Chapter 4

Experimental method: Device fabrication

Carbon is one of the most abundant materials on Earth and when bonded to itself, can be found in a number of allotropes like diamond, graphite, fullerenes, graphene and so on (Fig. 4.1) [60]s. These allotropes occur due to the different ways the chemical bonds are structured. The hexagonal honeycomb lattice of graphene is the most stable one. Graphene is considered one of the exotic materials of the 21st century.

This monolayer allotrope of carbon has earned attention worldwide since 2004, resulting in a Nobel Prize in Physics in 2010 for Geim and Novoselov, before which it was considered that the strictly 2D material can not exist [36].

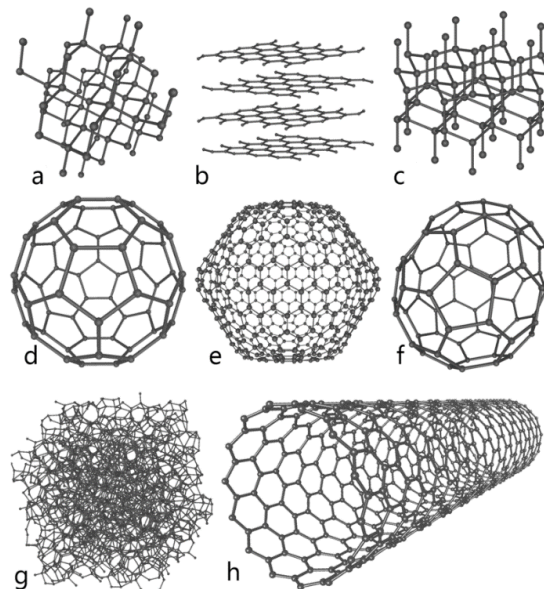


Figure 4-1 The allotropes of carbon: a) diamond, b) graphite, c) lonsdaleite, d) C60 buckminsterfullerene, e) C540 Fullerite f) C70, g) amorphous carbon, and h) single-walled carbon nanotube. [From Wikipedia]

Due to its exceptional charge transport, mechanical, thermal and optical properties, graphene is now considered for a variety of novel and futuristic applications such as nanoelectronic devices, gas and biosensors, flexible electronics and so on [61]–[63].

However, the practical application of graphene based devices is still restricted mostly due to the fact that tailoring graphene to the desired forms is not established yet. The mechanical and electrical characteristics are immensely affected by the defects in graphene. At the same time, intentionally created periodic defects can open up new possibilities such as phononic applications. Therefore, it is essential to be able to visualize and understand monolayer graphene in the atomic regime. There are mainly two methods of obtaining pristine monolayer graphene,

a. Mechanical exfoliation: Graphene can be readily exfoliated from bulk graphite because graphite is basically graphene sheets attached by van der Waals force in a stacked fashion [36], [50], [61], [64]. The process is as simple as attaching the sticky side of scotch tape on a graphite source and pulling out, causing a number of graphitic flakes with variable area and thickness to adhere to the tape. These flakes then can be easily transferred onto a desired substrate i.e. SiO₂ and under careful observation under an optical microscope, monolayer graphene can be easily detected. (fig4-2) [65]

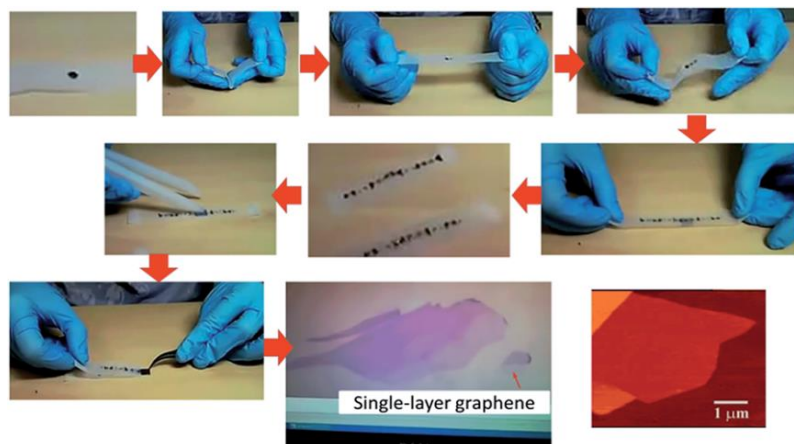


Figure 4-2 Illustration of the process of scotch-tape based mechanical exfoliation method. [8]

b. Chemical vapor deposition (CVD): The domain size obtained by mechanical exfoliation method is rather small and limits the flexibility in device fabrication process in many cases. Monolayer

graphene is also produced by epitaxial growth by chemical vapor deposition (CVD) method where methane as a precursor gas is inserted into a growth chamber along with a carrier gas. A metal is used as a substrate to avoid formation of carbides as a byproduct of the chemical reaction. Metal substrate also helps avoid formation of carbon solid solution that can range from room temperature up to 1000 °C (fig. 4.3) [66]. To briefly explain the mechanism of graphene formation, carbon would diffuse into the metal and precipitate on the surface to form monolayer graphene. [67], [68].

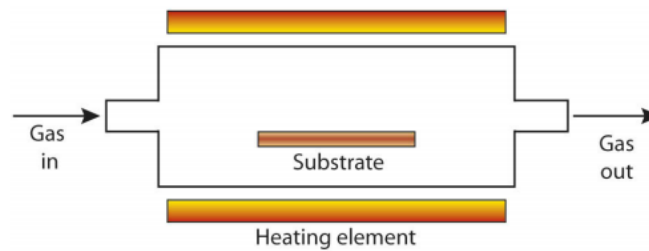


Figure 4-3 Schematic of a CVD growth chamber [11]

In this chapter, the fabrication of graphene nanophononic device is being described. For this experiment, commercially available CVD graphene (Graphene supermarket, Graphenea) on Cu-foil has been utilized. The devices are fabricated on a Si substrate covered with 500 nm thick thermal SiO₂. The substrate wafers are available commercially (University Wafer). The nanophononic device consists of suspended graphene with periodic nanopores with metal electrodes acting as the thermal sensors. The aim is to be able to detect the change in thermal transport through the suspended graphene with and without the periodic nanopores. It is expected that the nanoporous structure would exhibit significant reduction in thermal conductivity due to phonon scattering.

4.1 Preparation of the sample substrate

The substrate was diced into the size of 15x20 mm wafers to accommodate the sample into the sample cassette of our EBL system (ELS-7500, ELIONIX INC., Japan). The wafer is also pre-diced into smaller sections for easier separation of devices to fit into a chip carrier. The dicing process is carried out with a dicing saw from A-WD-10B, Tokyo Seimitsu Co., Ltd., Japan). Afterwards, the substrates are cleaned with acetone, isopropyl alcohol (IPA) followed by deionized water (DIW).

Finally, they're once again cleaned with piranha solution (hydrogen peroxide H_2O_2 and sulfuric acid H_2SO_4) to remove any contaminations.

4.2 Transferring CVD graphene on the substrate

Polymer supported graphene transfer is the most widely used method for graphene transfer. In this process, a polymer layer such as PMMA, poly bisphenol A, PDMS or special self release polymers are used as a temporary support to prevent folding or tearing of graphene during the metal etching step [69], [70].

For our experiment, commercially available CVD graphene from Graphene Platform has been used. The CVD graphene is delivered on a 4x4 inch copper foil. It is expected that high quality monolayer graphene covers the top side of the entire Cu-foil surface, which is the desirable layer we want to transfer on the substrate. To begin the process, a suitable section out of the Cu-foil is cut out. Care has been administered while handling as not to inflict damage on the top layer. PMMA was spin coated on the substrate at 4000 rpm and post baking was done on a hot plate for 5 minutes at 180 °C. This PMMA layer acts as a support and protective layer for the graphene during the following steps of etching and transfer. The Cu foils containing graphene was moved carefully on the surface of the etching solution (25% Ammonium peroxide sulfate (APS) $(NH_4)_2S_2O_8$) keeping PMMA/graphene side up. Once the copper is completely dissolved in 5-6 hours, the PMMA layer containing graphene is carefully transferred to DIW for 15 minutes. This allows the residual APS to be diluted and removed. This step is repeated 3 times to ensure maximum possible removal of APS. In the last step, The PMMA/graphene layer is picked out of the water bath with the substrate. Afterwards, the sample is air dried to remove any excess water and then baked on the hot plate at 120° C for 2 minutes. Keeping the sample in vacuum condition for a few hours after this step seems to be preferable to enhance the adhesion of graphene on SiO_2 and increase the quality. However, any technical proof to assess this condition has not yet been confirmed. Later on, the PMMA is removed by keeping the sample in acetone for 2-3 hours. The sample is again rinsed in acetone and IPA. Graphene is very sensitive to impurities and contaminants; therefore, the cleanliness of graphene is vital when studying its intrinsic properties. Due to the polymer residue after the transfer process, cleaning the sample is necessary and critical. Therefore, the sample kept in Acetone (60°C) for 30 min before rinsing in IPA for additional 2 min. Then the sample annealed in the infrared furnace (ULVAC VHC-P610CP) for 3 hrs at 250°C in (Ar+H₂) atmosphere. Figure 4.4 shows Raman spectrum of one of the received samples (before cleaning). Address pattern (5.91X6.5) mm² with registration marks and contact pads fabricated by one EBL step on top of

(10X10-mm²) CVD sample.

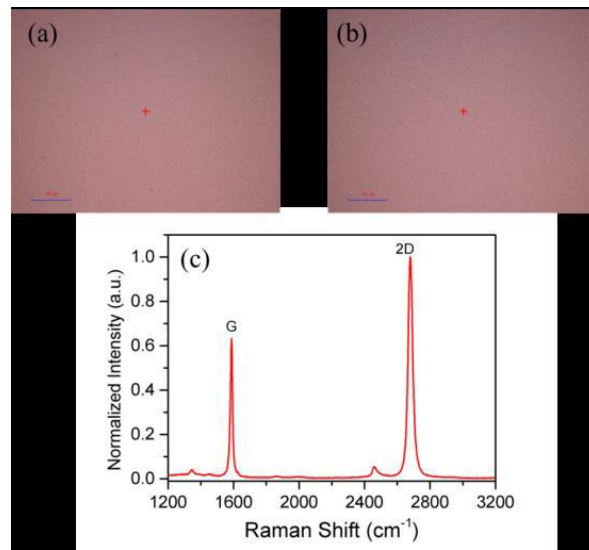


Figure 4-4 (a) and (b) images of CVD graphene sample from Graphene Platform. (c) A Raman spectrum of our CVD samples provided by the company.

4.3 Device fabrication

The measurement method involves a heating element that should produce a thermal gradient through the graphene, and the thermal transport is measured at a metal electrode. The GNR should be suspended to ensure maximum heat transport through graphene itself. There should be a heating and sensing element to measure the thermal transport through the GNR.

A schematic of the device is shown in fig. 4.5

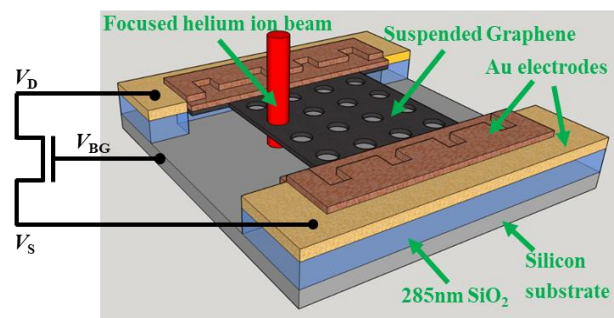


Figure 4-5 Schematic of the GNM device used for thermal characterization.

The device fabrication method is discussed in detail in the following segments.

4.3.a Fabrication of metal contacts on the sample

The sample device consists of 4 metal electrodes, each equipped with 4 contact pads for performing 4-terminal electrothermal measurement. Before beginning the fabrication, the CVD graphene should be void of impurities and foreign particles. The samples with CVD transferred graphene are kept in vacuum environment, but the samples are always rinsed in acetone and IPA and dried on a hot plate prior to every process.

For electron beam lithography (EBL), I coated the sample with a positive bilayer resist consisting of Methyl Methacrylate (MMA)/Poly Methyl Methacrylate (PMMA 495K). The sample was pre-baked at 180° C for 5 minutes. MMA and PMMA resists were spin coated at 2000 and 4000 RPM respectively, with a 5 minutes soft-baking at 180° C in between. The benefit of using bilayer resist is to achieve an undercut after the development due to the difference in sensitivity of the upper and lower layer of the resist. This undercut significantly enhances the liftoff process. Our lab has already developed this recipe as shown schematically in fig. 4.6

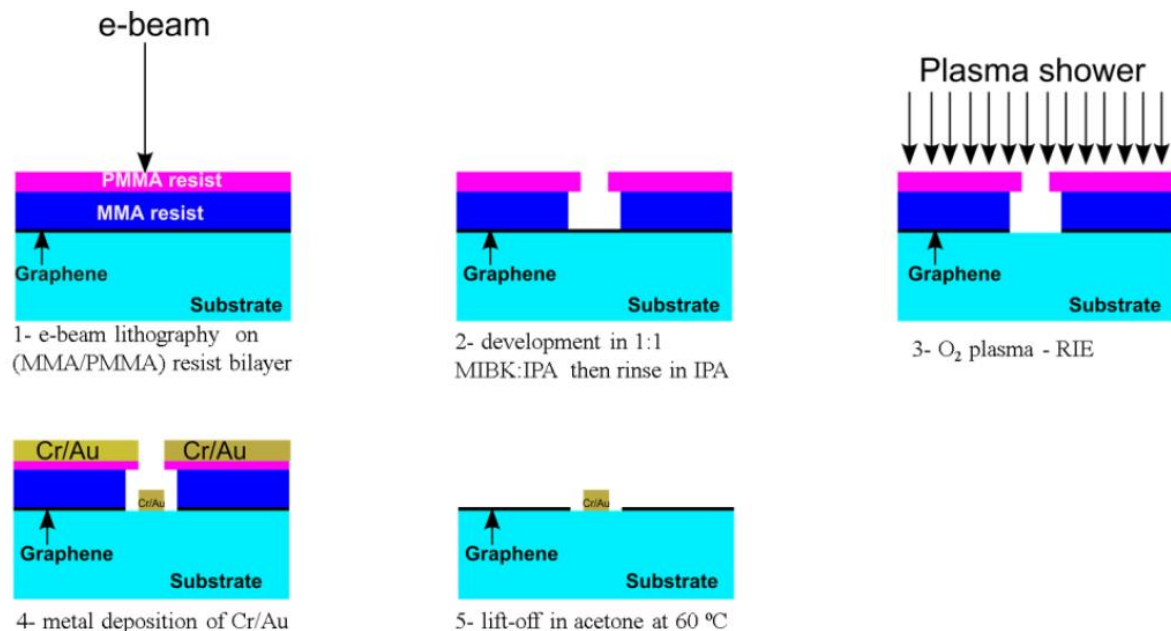


Figure 4-6 Flow chart of EBL lift-off technique for metal deposition and the significance of using MMA/PMMA bilayer resist.

The e-beam lithography (EBL) was performed using Elionix ELS-7500 EBL system operating at an acceleration voltage of 50 keV. The exposed sample was developed in 1:1 MIBK: IPA mixture (Methyl isobutyl ketone (MIBK):2-Iso-Propanol (IPA)) for 51 secs, then immediately rinsed in IPA for 30 seconds. This process yields nicely sharp patterns as shown in fig. 4.7.

Before metallization, the sample was placed in a Reactive Ion Etch (RIE) chamber to etch the CVD graphene. This step makes it possible to have the metal in direct contact with the SiO₂. Otherwise, if graphene is between the SiO₂ and metal, peeling occurs during consecutive fabrication steps. The uncovered Graphene layer was etched in O₂ (10 sccm) using an RF power of 30 W for 25 sec and at a pressure of 4 Pa.

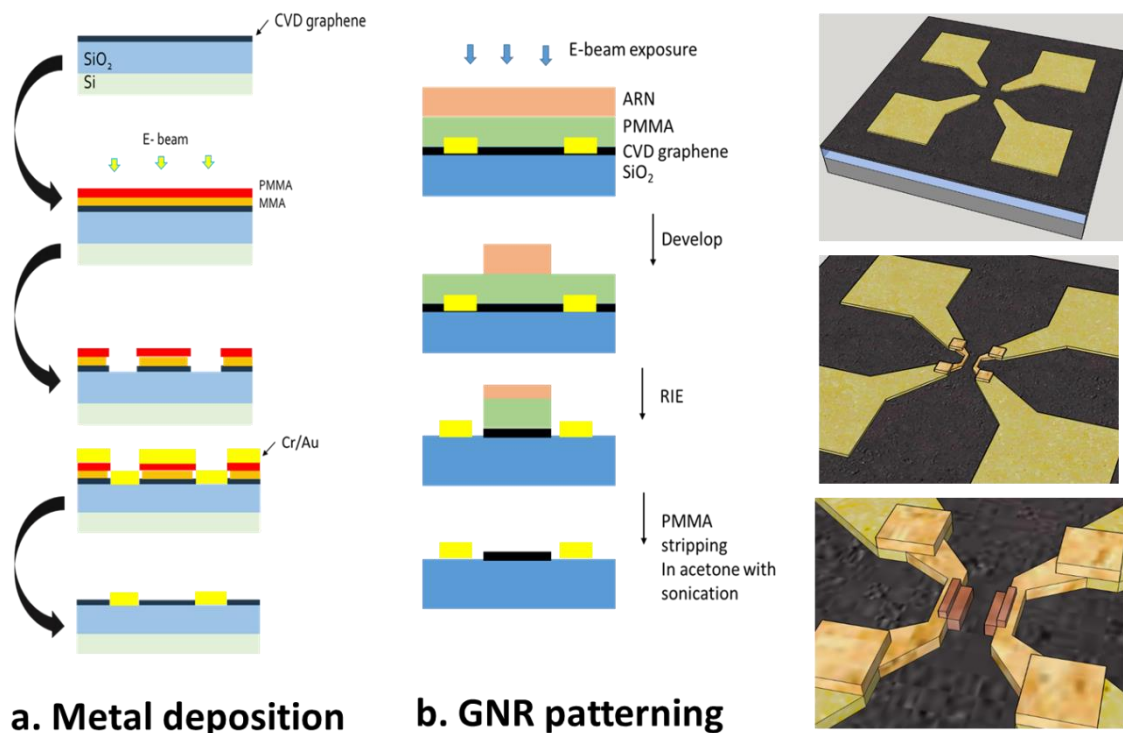


Figure 4-7 Fabrication of mask pattern for metal contacts (a) The process of obtaining the metal contacts by lithography and liftoff is shown. (b) the mask pattern of the original sample prepared in AUTOCAD. (c) the pattern for large contact pads after development. (d) comparison of resolution at the center of the pattern. The metal electrodes for thermal sensing will be patterned in this area along with GNR.

However, as the pattern is quite large, for the later processes, I have switched to using optical lithography for the later endeavors. The optical lithography system (Heidelberg MLA 150 Maskless Aligner) provides a minimum pattern resolution of 600 nm, which is acceptable for my sample. It is a full scale production level laser writer which can be used to perform lithography

directly on wafers as well as to prepare photomasks for contact or shadow lithography. In this case, a positive optical resist AZ-1500 spin coated at 5000 RPM on the sample was used. The sample was pre-baked for 5 minutes at 120°C to ensure no moisture was adhered on the surface, as the resist is hydrophobic and any amount of moisture might lead to bad adhesion and subsequently to distorted structures.

The exposed sample was developed using MF-319 for 55 seconds, and then rinsed in DIW for 30 seconds. The graphene was removed by using RIE using the similar recipe as mentioned in the previous paragraph. Afterwards, gold deposition and liftoff was carried out in a similar fashion.

The metal deposited with an electron beam evaporator system (EBE) (ULVAC MUE-ECO-EB). At a base pressure of 1×10^{-3} Pa, I deposited Chromium of 5 nm thickness and gold of 75 nm thickness. The rate of deposition is ~ 1.5 Å/second and ~ 2.5 Å/second for Chromium and gold, respectively.

Chromium provides good adhesion between gold and SiO₂. After the metal deposition was complete, the sample was allowed to be cooled down to room temperature and kept in acetone for ~ 30 minutes for liftoff. The samples after depositing metal contacts is shown in fig. 3.8. It is to be noted that, vernier scales have been added to the pattern as well. This additional step helps keep track of shifting of the patterns in the later steps.

4.3.b Fabrication of the electrodes

The electrodes are the crucial components of the device and the trickiest as well. These electrodes are small constrictions with a width in the nanometer range and a length of a few micrometers. These will work as the heater and thermometer to measure the thermal conductivity of graphene. As the electrodes are much smaller than the rest of the components of the device, I used EBL with a high resolution positive resist, ARP.

One important issue to discuss here is the misalignment between the different layers of exposure. The basic fabrication process involves stacking individual layers with different exposure conditions. Also, it is to be mentioned again that the very first layer was fabricated using optical lithography, while the following layers were fabricated using EBL. Therefore, aligning the individual layers is extremely important.

Here I would like to explain the aligning method in EBL. The first step is inserting the pattern information into the EBL system. The alignment marks for the first layer must be patterned on the substrate. There are two types of registration marks (REG marks) used as discussed below,

REG 2 marks: used for global position of the wafer for writing. The software searches for REG marks A and B, calculates rotational misalignment with respect to the stage from the detected position and orients the stage accordingly. Then it calculates the difference between the detected actual position to the value obtained from the CAD file. This data is used in the next step.

REG 3 marks: these are for local rotational misalignment correction of the actual scan area. The software finds the marks A and B to calculate the rotational misalignment from the detected actual position and compares it to the actual specified position. This data is then added to the pattern for exposure.

Another topic to consider here is the registration types. Automatic registration allows the software to detect the reg marks automatically. As long as the liftoff is good and the marks are sharply defined, auto registration is recommended. For manual registration, the operator has to manually drive the SEM GUI to find the reg mark and align it with a cross, square or circle mark according to the shape of the reg mark itself on the fabricated sample.

Unfortunately, even after carefully maintaining the standard alignment procedures, it is expected for the EBL systems to show at least some shift between the layers. These errors are due to two major problems,

Due to the proximity effect, the actual marks slightly expand and their edges become blunt [71]. This kind of expansion affects the position of the alignment spot of the marks. The blunt edges therefore increase the alignment uncertainty in high magnification

The second problem is the mechanically induced errors, which is unavoidable for almost any mechanical system. This error will be different for every EBL system. In our case, the errors occurring from stage movement seems to be almost always constant.

Considering all these issues we have modified the design of the electrodes so that it gives maximum possibility of compensating the misalignments in most of the fabrication cases.

The misalignment was found to be $\sim 1 \mu\text{m}$ in the x direction, but more severe in the y direction with a value exceeding $\sim 2.5 \mu\text{m}$ most of the times, as shown in the following table.

Table 4.1: Average misalignment while combining MLA and EBL

Pattern type	Minimum separation	Minimum pattern width	Process	Thickness of gold	Misalignment
Low resolution mask	$\sim 5 \mu\text{m}$	$2.6 \mu\text{m}$	MLA	100 nm	$\sim 1.2 \mu\text{m}$ along Y-axis
High resolution mask	$1 \mu\text{m}$	$.5 \mu\text{m}$	EBL	80 nm	

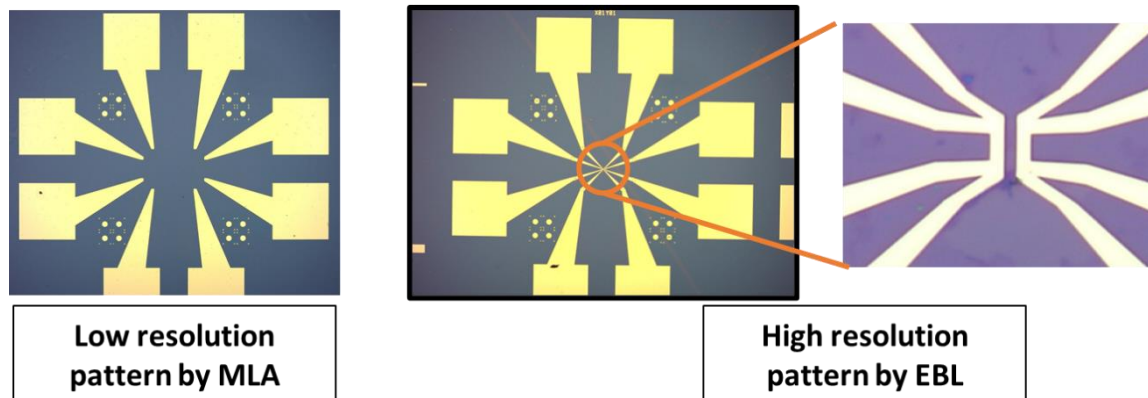


Figure 4-8 On the left, the high resolution center pattern is shown after optical lithography and development. ON the right, the same sample is shown after metal deposition.

To carry out the operation, ARP-6200 resist is spin coated on the substrate at 4000 rpm for 60 seconds. The sample is soft baked at 150°C for 60 seconds. The exposure is carried out at 0.0375 dose time and 50 pA current. After exposure, the sample is developed with AR 600-546 developer for 110 seconds, then rinsed in AR 600-02 to stop the chemical reaction of the developer. The sample is then rinsed in DIW for 30 seconds and post baked at 130°C for 30 seconds. In fig. 4.8, the optical microscope images of the fabricated metal contacts and electrodes are shown.

4.3.c Patterning of the GNR

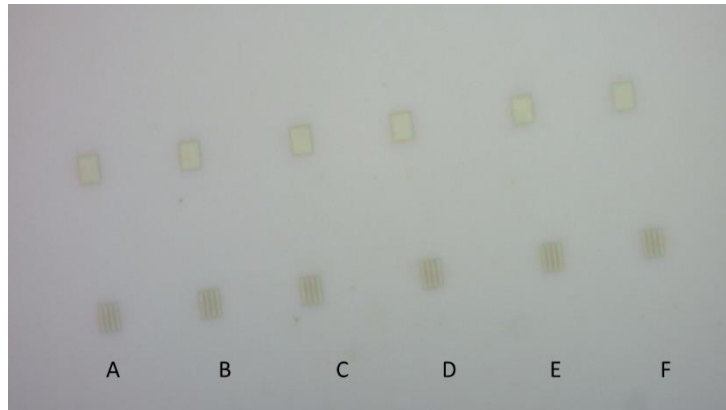
According to the design, the GNR sits at the center of the pattern and good alignment is necessary. This time, two different methods were utilized.

For the first method, I used a bilayer resist consisting of PMMA and ARN-7520. ARN is a negative resist, meaning that it remains on the substrate after exposure and developing. It belongs to the novolac family (obtained from Allresist) which gives very high resolution for electron beam lithography. The ARN provides the pattern layer and the PMMA is the liftoff layer, as it is difficult to remove ARN with currently available resist removers.

Before the process, the sample is again rinsed in acetone, IPA and annealed in the infrared furnace in Ar+H₂ environment for 3 hours at 250° C to ensure that the graphene is clean. Immediately after annealing, PMMA and ARN are spin coated respectively at 4000 RPM with a 5 minute soft bake at 180° C in between. The EBL exposure is carried out with 250 pA current at 50 kV acceleration voltage. Dose test was carried out to realize the best possible dose and current. The dose test result for ARN is shown in the table below.

Table 4.2 Dose test for ARN

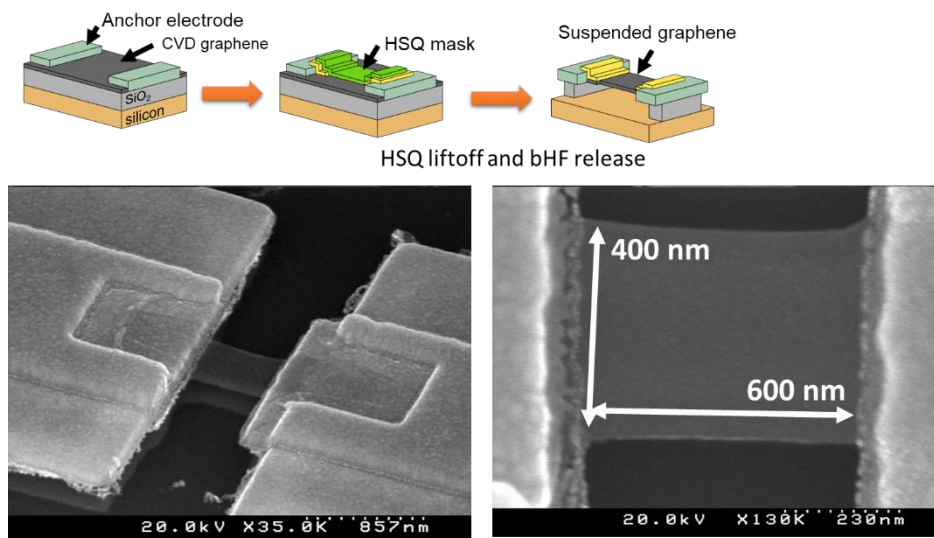
Write field (μm)	Dose (μC/cm ²)	Current (nA)	Dose time
600	110	1	0.11
	100		0.10
	90		0.9
	80		0.8
	70		0.7
	60		0.6



Dose time varied from 0.11 to 0.06 μs

Figure 4-9 Dose test results for negative ARN resist. The patterns here have a minimum resolution of 250 nm.

From the dose test results, I chose the 0.60 $\mu\text{C}/\text{s}$. The sample was developed in AR 300-47 for 90 seconds. The PMMA and graphene was removed by oxygen plasma for 2 minutes and 10 seconds. The etching rate of ARN with O_2 plasma is 125 seconds and the thickness of the resist is $\sim 180 \mu\text{m}$. It is safe to say that a few hundred nm of ARN will still remain after PMMA and the rest of the graphene is removed as shown in fig. 4.9. Finally, the sample is rinsed in acetone in an ultrasound bath for 2 minutes to remove dissolve PMMA and remove the ARN layer (liftoff of ARN layer). The quality of the GNR obtained in this process is confirmed by RAMAN spectroscopy.



SEM micrograph of suspended GNR sample

34

Figure 4-10 Schematic of the GNR patterning and suspension process. Bottom: SEM image of the Patterned and suspended GNR with 400 nm x 600 nm dimension.

The second process of patterning GNR is explained now. Instead of ARN, we used HSQ (hydrogen silsequioxane) which is also a negative resist. HSQ is spin coated at 5000 rpm for 60 seconds resulting in a thickness of about 32 nm. After that, the sample was pre-baked at 180 °C for 5 minutes. The GNR was patterned using EBL at 250 pA current and 90 mC/cm² dose and the exposed sample was developed in MF-319 developer for 70 seconds and gently rinsed in flowing DiW for 30 seconds. Afterwards, it was post baked at 90 °C for 30 minutes and the hard mask for the GNR was prepared. Afterwards, reactive oxygen plasma was used to remove the exposed graphene. The O₂ plasma is non-reactive for the SiO₂ hard mask. The process is shown in fig. 4.10. For our final samples, we followed this process of GNR patterning.

4.3.d Suspension and nanopatterning of the GNR

The suspension of the GNR is the most difficult part of the process and requires careful execution. We have seen that the failure of devices occur mostly during the process itself. Once the device is suspended, it has been fairly stable handle for experiments. The process of suspending monolayer graphene has been developed and demonstrated by our lab [51]. To develop the suspension and patterning process, we started with a sample layout as shown in fig. 4.11 that houses 94 devices with GNR lengths varying from 0.6 – 9.6 μm and widths varying from 0.2 – 16 μm.

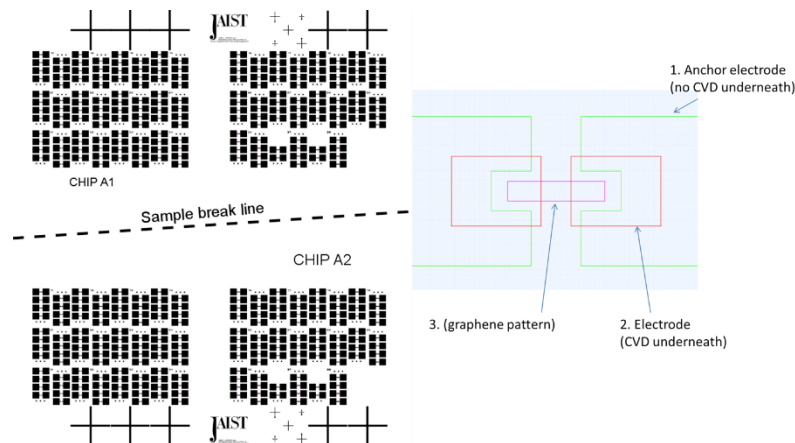


Figure 4-11 Layout for the sample used to develop the suspension process of GNR. on the left, the layout of the entire chip. On the right, the schematic representation of a single device.

The general fabrication scheme for this sample was a two step lithography to fabricate the anchor and electrodes, the patterning of graphene using a negative resist. A completely fabricated sample and the optical image of a single device with a large GNR is shown in the following figure.

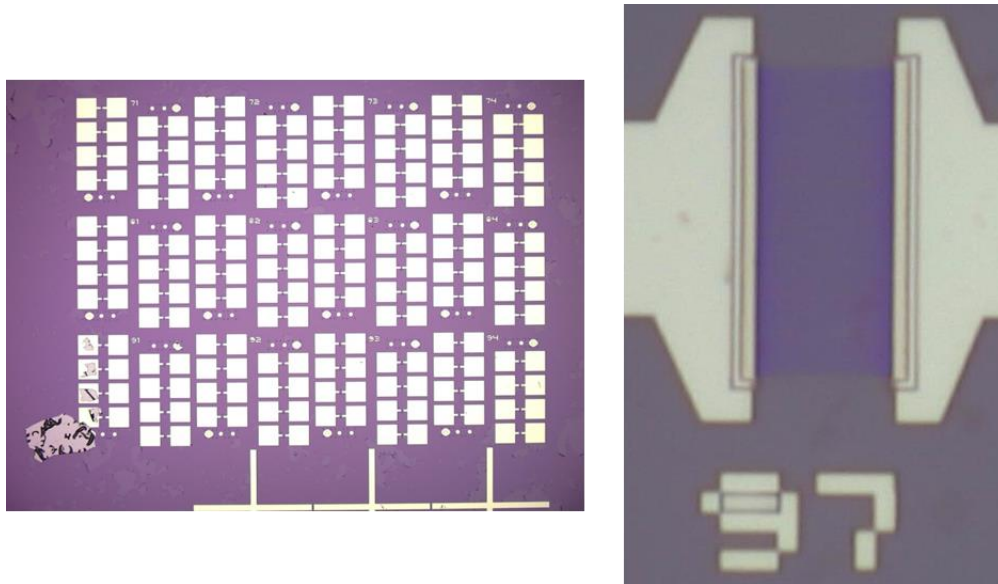


Figure 4-12 The fabricated sample for developing the suspension and patterning process.

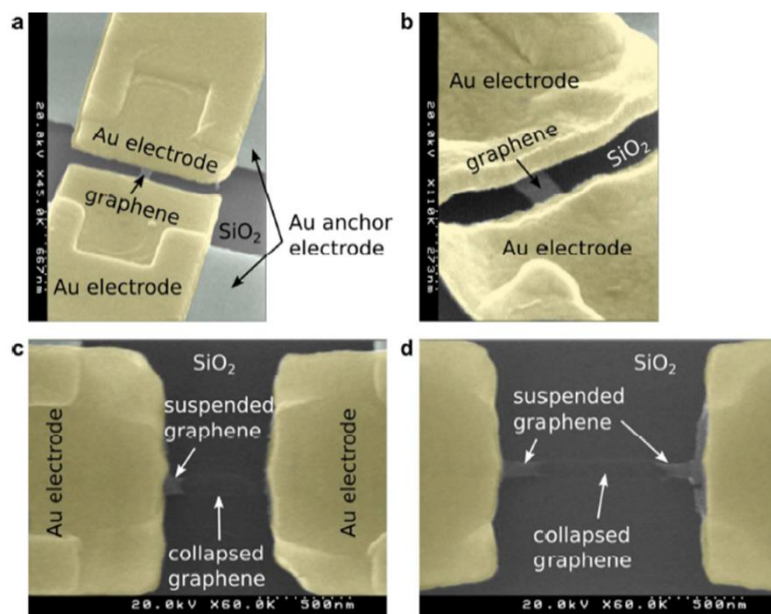


Figure 4-13 SEM micrographs of the fabricated samples.

The fabricated samples with supported graphene are released in buffered hydrofluoric acid (bHF)

for 60 seconds to result in ~ 100 nm SiO₂ etching for. However, for larger graphene ribbon with higher than 1.2 μ m width, the etching time is significantly higher, about 180 seconds. The longer etching time removes about 300 nm SiO₂. After that, the sample is carefully taken out of the bHF container, and then submerged into DIW for one minutes to rinse the bHF. This step is repeated 3 times. Then, the suspended sample is released into an IPA bath. To avoid the collapsing of GNR due to surface tension, the sample is dried in a critical point dryer. Finally, the sample is annealed once again at 250⁰ C for 3 hours in Ar+H₂ environment. From the SEM images in fir. 4.13, suspended and collapsed GNR can be identified from their clear contrast.

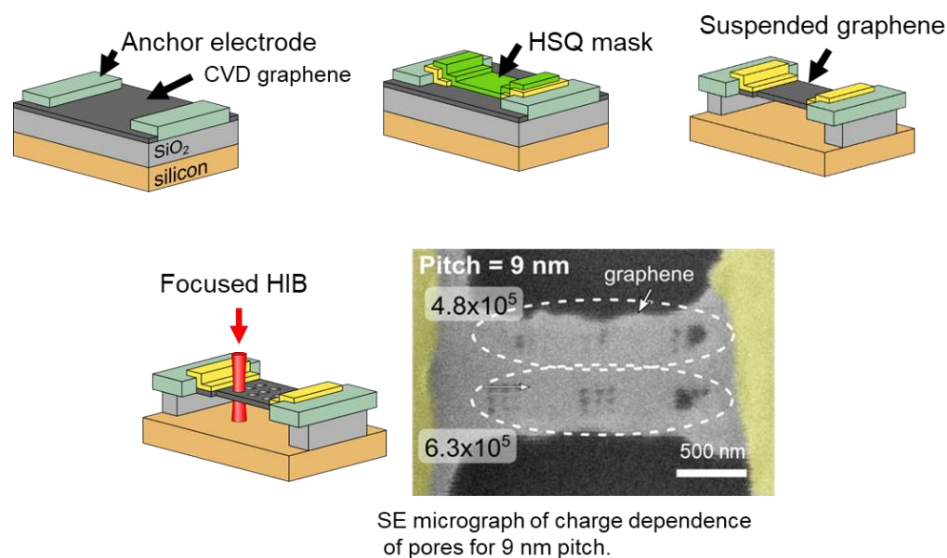


Figure 4-14 The process of HIBM milling on suspended graphene sample and the first attempt at milling shows a GNR milled at different ion doses.

The suspended devices were patterned by using HIBM facility in AIST in a high vacuum chamber . The schematic of the mechanism of HIBM milling is shown in the fig. 4.14. In the figure, we can see that nanopattern with 9nm pitch was obtained. The dose should be optimized in this case because as seen from the figure, the nanopatterns are already obtained for the low charge of 4.81×10^5 ions/pore and 6.3×10^5 ions/pore. At the higher dose, the pores tend to get merged which is due to the overexposure from Gaussian beam tail [72]. In fig. 3.15, a device patterned with nanopores at 25 pitch is shown. The large area GNR with 600 nm width and 4 μ m length was patterned successfully with the charge of 4.81×10^5 ions/pore. By optimizing the dose, it was possible to fabricate the nanopatterns at a pitch as low as 12 nm as shown in fig. 4.15. As the pitch was much smaller, this time the dose was also reduced to 2.18×10^5 ions/pore. We can see that

the nonpatterns were obtained but at some vertical cracks can be observed in the zoomed in image (fig. 4.15 b). These vertical cracks were formed due to two effects,

- The tensile stress in the horizontal direction,, and
- Gaussian beam spot caused the adjacent nanopores to merge to form a crack.

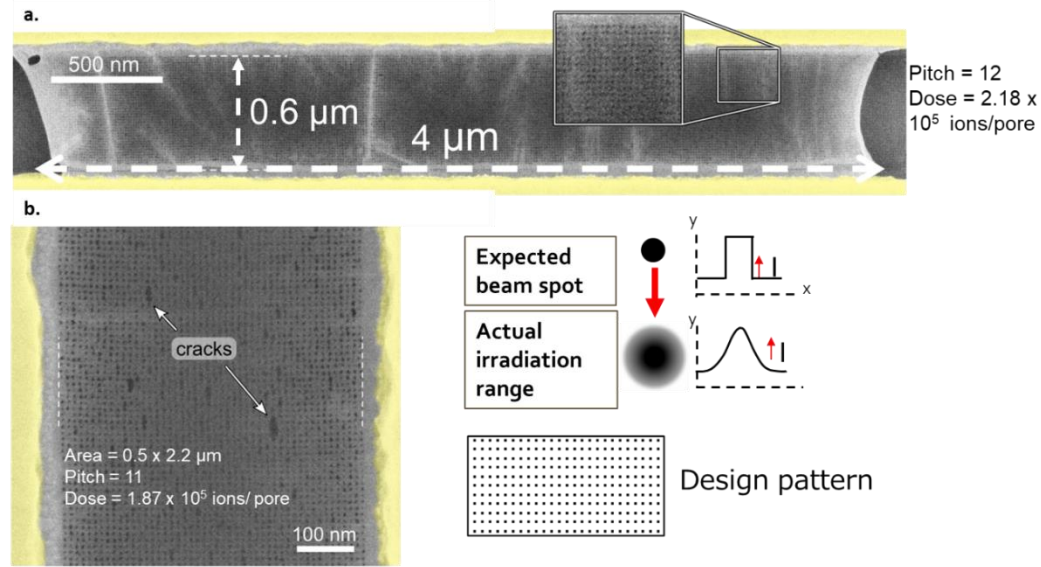


Figure 4-15 (a) High resolution nanopores with a pitch of 12 nm are formed on large area suspended GNR. The dose was optimized. (b) Some cracks and large pores are observed in the zoomed image. These cracks are formed either due to the tensile stress and/or the Gaussian beam spot that merged the adjacent pores.

After successfully patterning ~10nm pitch nanopores on suspended graphene, we extended this experiment to fabricate the GnPC for the thermal measurement. From our previous work, we saw that a beam current of 1 nA and a dwell time of 45000 μs yields the best results. Therefore, In order to maintain the consistency of the dimensions of the nanopores, and also to be able to investigate the influence of different pitch size we kept the experimental parameters the same as before. Here, the dwell time here refers to the time that one nanopore is exposed to the helium ion beam. If required, the patterned samples could be checked using secondary helium ion beam microscopy. The contaminations on the milled GNR are suspected to be the residual resist.

For the final sample, the GNMs were patterned by HIBM on the suspended GNRs in a high vacuum chamber ($< 5 \times 10^{-7}$ mbar), as shown in Figure 4.16. From the images obtained from the

secondary HIBM micrographs after patterning of the sample was finished, the diameter of the nanopores was estimated to be approximately 6 nm as shown in Figure 4-16 (b). It can also be observed that at some areas, no nanopores cannot be observed. This is due to the contaminations on the GNR that prevents the He-ion from making nanopores. From the image, we can also confirm that the fraction of the missing nanopores is relatively low compared to the entire meshed area on the sample.

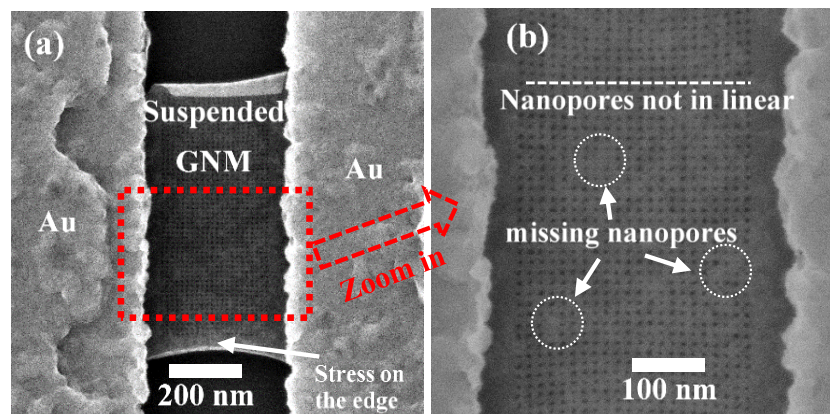


Figure 4-16 (a) Secondary microscope image of typical suspended GNM devices. (b) Magnified image of the fabricated nanopores with ~6nm diameter.

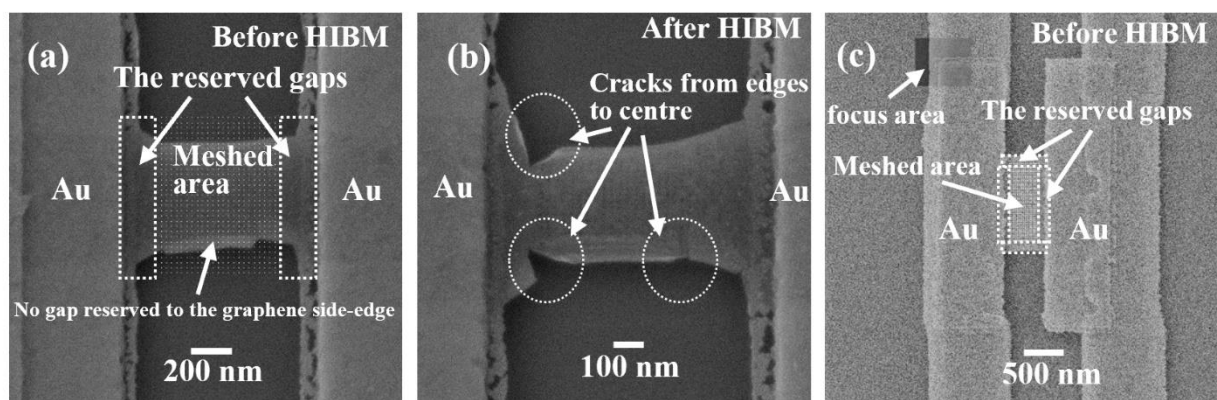


Figure 4-17 (a) 100 nm wide non-meshed area maintained on the left and right edges. (b) visible cracks are observed at the edges of the device (a) as observed by secondary HIBM after milling (c) 100 nm gaps on the top and bottom, 50 nm gaps on the left and right were maintained to stabilize the meshed devices. For observation of this device, the focus was kept on the metal layer.

It is to be addressed here that, milling such a large GNR entirely might cause the structure to collapse at the edge connecting the GNR to the metal electrode. To avoid this, we attempted to maintain a certain distance of 50 nm between the graphene and metal contact to create an anchor for the GnPC device.

Summary

This chapter focused on the fabrication process of the device to measure thermal conductivity of GnPC by heat spreader method. The main points are,

- A repeatable method to fabricate complex multilayer designs was developed. One important aspect of this method is to be able to combine optical lithography and EBL. This helps immensely to reduce the fabrication time. Also, the process has been optimized so that the misalignment between the optical lithography and EBL layers are maintained strictly within the acceptable level.
- A suitable method to suspend large area GNR was developed during the early stage of this project and later implied for the fabrication of the main device.
- Finally, HIBM has been used to fabricate extremely high resolution nanopores on GNR which has the possibility to exhibit PnBG in accordance to the numerical simulation discussed in chapter 2.

Chapter 5

Measurement and thermal characterization

Electronic transport in graphene has been extensively studied since its isolation. But the experimental challenges limit the methods of understanding the thermal properties. As discussed earlier, a method for measuring room temperature thermal conductivity of suspended graphene has been reported using the heat generated with the laser beam of RAMAN by Balandin et. al. [21], [32], [40]. Malekpour et. al. measure the thermal conductivity of graphene laminate films deposited on polyethylene terephthalate (PET)[49]. The obtained values range from about 3000 $\text{Wm}^{-1}\text{K}^{-1}$ to 5000 $\text{Wm}^{-1}\text{K}^{-1}$, which is much higher than diamond and graphite. However, the temperature (T) sensitivity of the RAMAN techniques, the k-T behavior for the 2D system has not yet been understood properly. Also, these measurements were performed on supported graphene. the charge mobility of graphene supported on SiO_2 should be 10 times suppressed compared to the supported graphene [73].

Control and manipulation of heat transport through materials has been a key goal in thermal engineering. Thermal rectification is one of the most well sought aspects of solid-state devices which is an analogous expression of an electrical diode in which the thermal transport through a material is directional. To say in the simplest way, thermal rectification is achieved when the heat flow in the forward direction is relatively higher and very little heat flow is maintained in the backward direction. There have been quite a few theoretical studies on thermal rectification in graphene based systems like the one described by J. Hu et. al where thermal conductivity of symmetric and asymmetric graphene nanoribbon were studied by molecular dynamic simulations. It was observed that the asymmetric nanoribbons show significant thermal rectification behaviors compared to the symmetric ones [74]. An experimental study of observing thermal rectification in graphene has been conducted by H. Wang et. al, where they claim that monolayer graphene can be potentially engineered to create high-performance thermal rectifiers [46]. In our experimental work, we had the chance to explore the effect of asymmetry in graphene nanoribbons to demonstrate thermal rectification characteristics.

5.1 Measurement method overview

We established a measurement method with an aim to generate a temperature gradient through a graphene nanoribbon and detect the change in temperature at the heater. The basic idea of this measurement comes from resistive thermometry which is measuring the corresponding change in resistance of a material with the change in temperature. We used the 4-probe measurement method to detect accurately the change in resistance at the heating terminal as a function of applied power. This method is specially useful when the samples like thin films, thin wafer or thin semiconductor materials. The schematic of a 4-probe resistivity measurement system is shown in figure 5.1. Current is applied to the sample through the terminals 1 and 4 creating a potential drop across the terminals 2 and 3, which can be measured.

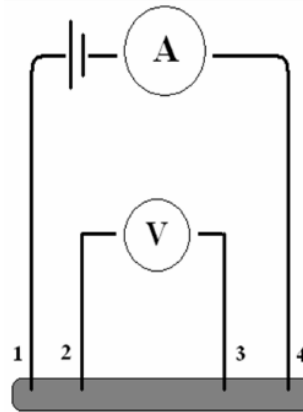


Figure 5-1 Schematic representation of the 4-probe electrothermal measurement.

As discussed in the previous chapter, we fabricated suspended GNM devices by engineering nanopatterns on them using helium ion beam milling (HiBM). Symmetric and asymmetric samples were fabricated by preferentially choosing nanoporous and pristine regions on the suspended GNR. For thermal characterization, we measured the thermal properties of the metal electrodes to establish a reference scale. Afterwards, we observed the thermal properties of a GNR with a uniformly patterned nanomesh. This device serves as the symmetrical device and provides comparable result with the reference electrode. Finally, we fabricated a GNM device with nanopatterns fabricated across the halfway length of the GNR to create an asymmetry.

The entire measurement process is carried out in 4 steps as mentioned below.

Step 1: calibration of the heating element: in this step, the metal electrode is calibrated which is used to detect the reference temperature.

Step 2: Measure the change in heater temperature as a function of applied current.

Step 3: Normalizing the reference temperature for multiple devices.

Step 4: Using the same method from steps 1-3, normalizing the temperature for the symmetrical device.

Step 5: Using the same method from steps 1-3, normalizing the temperature for the asymmetrical device.

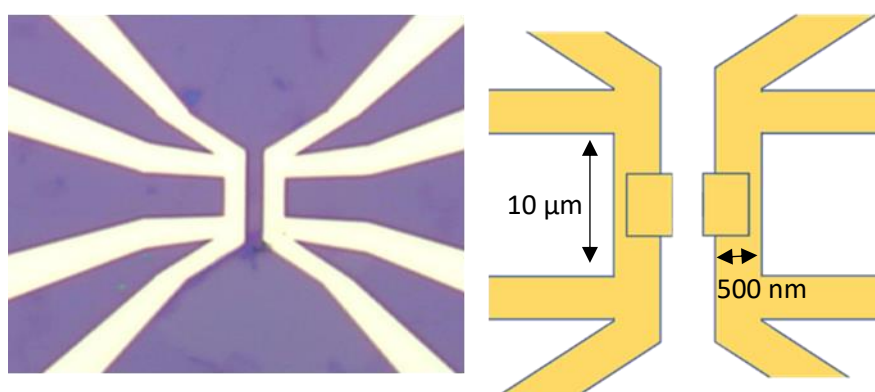


Figure 5-2 Left: Optical microscope image of the metal electrode device. Right: Schematic of the device.

The reference devices consists of gold electrodes as shown in the optical microscope image in fig. 5.2(left) and schematically shown in fig. 5.2(right). Regarding the calibration of the metal electrode, we took for devices and pattern the structure including both the heater and the sensor. The direction of the heater and the sensor can be swapped by changing the direction of the applied current. The device is made such that the center part of the electrode is much narrower than the metal contacts to induce joule heating when an electric current is applied and thus can function as a heater.

5.2 Effect of Joule heating on metal electrodes

Before proceeding to the measurement, we studied the effect of joule heating on the metal nanowire by FEM method. The performance and scaling of graphene based electronics is highly dependent on the quality of contacts between the graphene and the metal electrodes. Joule heating, also known as resistance heating or ohmic heating, is the phenomena when electrical current passing through a conductive material produces heat in the process. This is also one commonly anticipated reason of device failure. To better understand the role of Joule heating on thermal conductivity, several research groups have reported the methods to indirectly measure the local temperature changes during electromigration [75], [76]. However, any method to directly quantify the temperature fields due to electromigration has not yet been reported. Especially, for systems with nanoscale resolution, the knowledge remains vague, even though it is important to understand the phenomena for the sake of both to ensure the reliability of the nanoscale systems and to create functional devices. Here, I tried to simulate the effect of joule heating on the metal electrodes of the same dimensions and material properties as our fabricated samples. First, the heating power P is expressed by the following equation,

$$P \propto I^2R \text{ ----- (5.1)}$$

Here, I is the applied current and R is the resistance of the material and the law is known as Joule-Lenz's law. Joule heating can be explained as the interaction between charge carriers, e.g. electrons and the atomic ions on the material. If a voltage difference can be maintained between two points of a conductor, the resultant electric field can accelerate the charge carriers in the direction of the electric field. These charged particles now have kinetic energy and can collide with the ions in the conductor. These collisions result in scattering of the particles randomizing and deviating their direction of motion from the electric field, which constitutes thermal motion. This is the basic concept of thermal energy generation in a conductor [76]. Consequently, material flowing along such a wire is not replaced as the atoms are moving in the direction of the electron flow, which is called electromigration. These voids eventually result in failure of the wire itself, which is evident from the OM and SEM images of our samples.

FEM simulation was performed to understand the joule heating phenomena in the fabricated gold nanowire. COMSOL Multiphysics® version 5.4 includes a heat transfer module that was used for this work. Multiphysics coupling for heat transfer due to electromagnetic heating, i.e. joule heating, is possible in the new update, which gives more freedom in simplifying the model [77]. A model

was constructed consisting of large gold connectors and a gold nanowire at the center of the assembly which represents closely the experimental sample. As shown in fig. 5.2, the nanowire has a length of 10 μm , width of 500 nm and thickness of 100 nm. Models with two different configurations were made. Fig. 5.3 represents the model closer to the actual device. The boundary condition of the contact surface is specified using Fourier’s law of heat conduction written as,

$$\mathbf{n} \cdot (K\Delta T) = q_0 \text{ ----- (5.2)}$$

Here, \mathbf{n} is the magnitude of the unit vector normal to the contact surface of the subdomain and q_0 is the heat flux that enters the subdomain. A constant temperature is maintained at the opposite boundaries of the sub-domains according to the equation 5.3

$$T = T_0 \text{ ----- (5.3)}$$

Where T_0 is the initial temperature. All the other subdomains are constructed to assume that complete insulation from the surrounding environments is achieved so that,

$$\mathbf{n} \cdot (K\Delta T) = 0 \text{ ----- (5.4)}$$

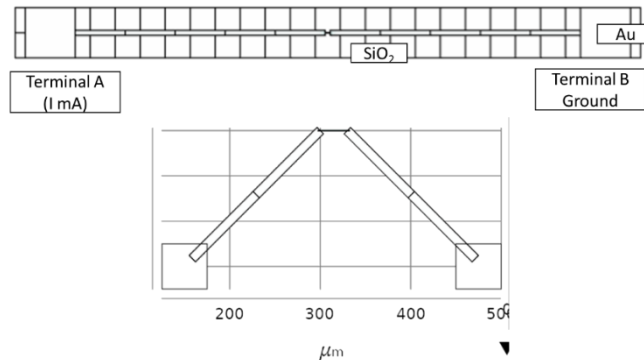


Figure 5-3 Model built with COMSOL multiphysics to quantify the joule heating effect at the gold nanowire. The bottom model was built as a supporting model to understand the thermal concentration at the bending point of the constriction.

This assumption implies that the conductor, despite being heated by some current source at a terminal, can only interact with either surrounding air or the substrate SiO₂. Air and SiO₂ have thermal conductivities of 0.024 Wm⁻¹K⁻¹ and 1.28 Wm⁻¹K⁻¹ respectively, which is negligible compared to the thermal conductivity of graphene. This assumption helps to simplify the mode by assuming that the heat transfer from graphene to either air or SiO₂ can be ignored.

Considering that the structure is in contact with air, we used the convective heat flux on the surface as the boundary condition. Mathematically, the heat flux is described by the following equation,

$$-n \cdot q = h (T_{\text{ext}} - T) \text{-----(5.1)}$$

Here, h is the heat transfer coefficient and T_{ext} is the temperature of the external fluid (in our case ambient air) from the boundary. h was defined considering free convection takes place between the surface of the gold and ambient air. We calculated the change in heat through the metal interface by applying some current I at one terminal and considering terminal B as ground. The terminal current was varied from 0.001 A to 0.1 A. For all the cases, it was observed that the increase of temperature was constrained mostly at the center of the structure. The constriction length was varied from 10 μm to 30 μm , where the prior one is closer to the dimension of the actual device. The temperature raised as a function of applied current for different constriction lengths is shown in the following table. All of the calculations were carried out at an ambient temperature of 293.5 K (table 5.1).

Table 5.1: Simulated result of temperature at the metal constriction due to applying current

Length of the electrode (μm)	Thickness of the electrode (nm)	Applied current (A)	Maximum temp. at the electrode ($^{\circ}\text{C}$)
10	100	0.0001	20
		0.001	20
		0.01	21.4
		0.05	55.7
		0.1	168

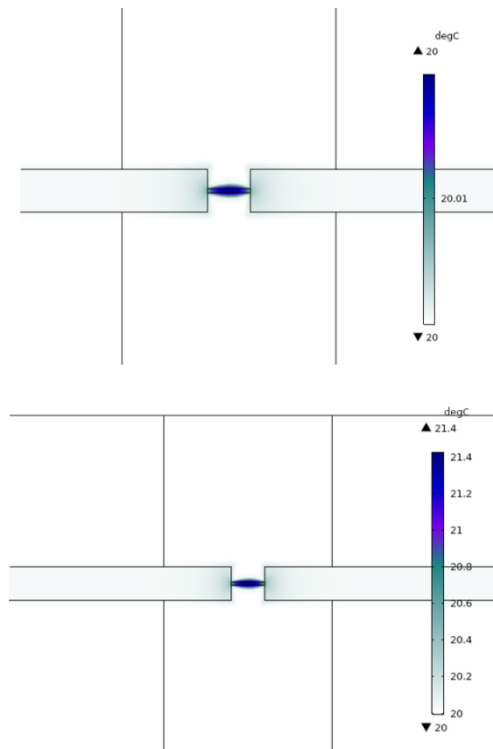


Figure 5-4 The joule heating effect is centered at the small constriction of the metal conductor:

5.3 Measurement setup

A KEITHLEY 4200 sourcemeter with system noise below 1 pA was used to apply current through the metal contacts and a KEITHLEY 2420 nanovoltmeter was used to measure the resistance at the constriction. All measurements were carried out in vacuum in a variable temperature helium close cycle cryogenic cooling system which can go down to ~ 4.8 K base temperature. The measurement temperature range was from 10K to 300K. The Au electrodes shown in fig. 5.3 were used to apply a drain current I_D and drain voltage V_D . For establishing the feasibility of the 4-probe measurement system, we first measured the temperature dependent resistance of the gold nanowire by varying the base temperature from 100K to 300K at an interval of 50K between measurements. The measurement current was maintained to sweep between -1mA to 1mA to ensure that no additional effect of joule heating took place. The measurement setup is shown schematically in fig. 5.5, where the Au electrode on the left side was calibrated first.

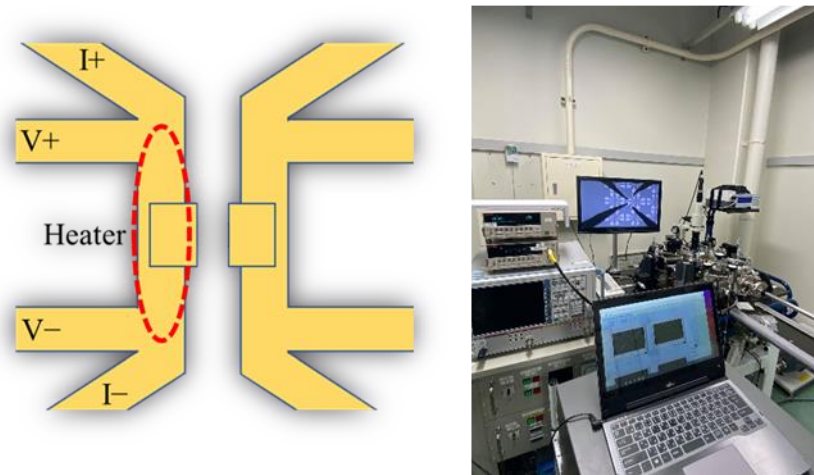


Figure 5-5 Left: the schematic of the device structure for 4-probe measurement. Right: actual measurement setup.

5.3 Electrical characterization

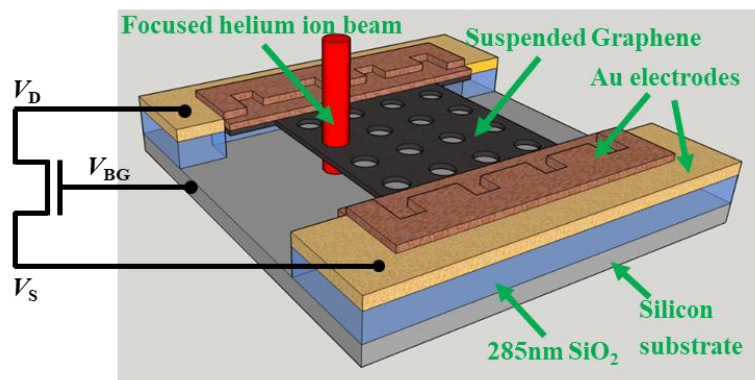


Figure 5-6 Schematic representation of the GNM device.

The schematic structure of the suspended GNM is shown in fig. 5.6. The device is fabricated on 285 nm thick SiO₂ substrate. The gold electrodes on the two sides anchoring the meshed GNR were used to apply a drain voltage V_D and source voltage V_S . the backgate voltage V_{BG} was applied at the silicon substrate at the bottom of the structure. As discussed in the previous chapter, 50 nm no-meshed area from the metal edges and 100 nm non-meshed area at the side of the GNR was maintained as shown in fig. 5.7.

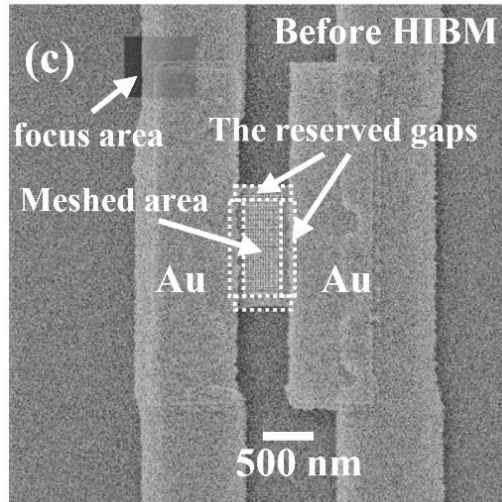


Figure 5-7 Fabricated suspended GNM structure with non-meshed edges.

Source and drain voltage were applied along the two metal electrodes and the chuck inside the cryogenic chamber was used to apply the backgate voltage. From similar experiments conducted in our lab previously, we have seen that during $(I_D - V_{BG})$ measurements, the GNMs would collapse [78]. It is due to the strong electrostatic force applied on the GNR by V_{BG} which results in a strong pulling force on the suspended GNRs. This phenomenon can damage the suspended GNM device. A reference GNM with 500 nm length and 1200 nm width was used to modulate the $(I_D - V_{BG})$ characteristics as shown in fig. 5.9. After extracting the charge neutrality point (CNP), conventional $(I_D - V_D)$ measurement was implemented for the other GNM devices with their pitch varying from 15nm to 50 nm. The GNM used for measuring the CNP was not imaged after meshing with HIBM to avoid additional damage on the device. These measurements are carried out at 300K base temperature.

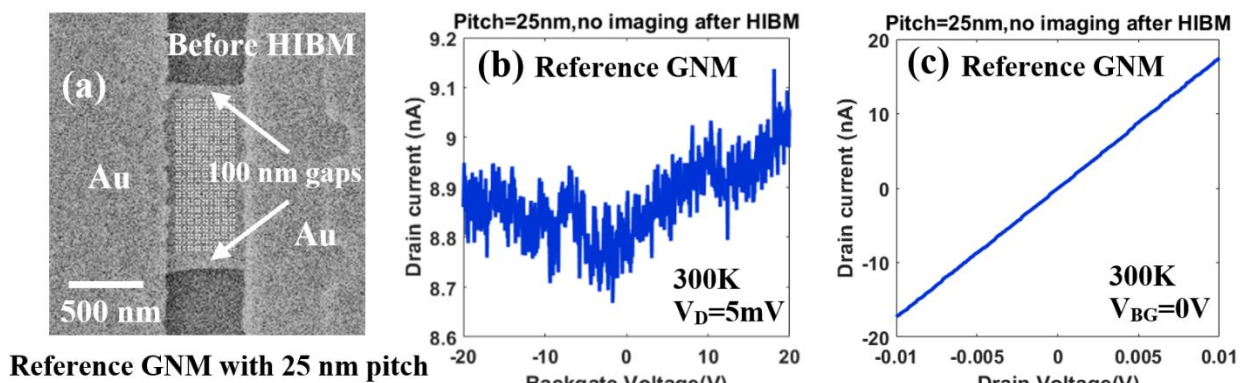


Figure 5-8 (a) The milling area of a GNM with 25 nm pitch before milling. Imaging was not done after milling to keep the device integrity (b) At a fixed $V_D = 5 \text{ mV}$ at a base temperature of 300 K, $I_D \sim V_{BG}$ plot is shown for the device shown in (a). (c) At a constant base temperature of 300 K and zero backgate voltage V_{BG} , linear $I_D \sim V_D$ relationship is observed.

As shown in fig. 5.8, the GNM device with 100 nm non-meshed area and a pitch of 25 nm for the meshed area shows V_{BG} dependence on I_D shows less than 10 nA current flowing at $V_{BG} = 0$, which is close to the CNP of the device. For comparison, a reference device as shown in fig. 5.10 was introduced. This device has seven suspended GNR with 500 nm length and 100 nm width. After measurement, it was seen that the average current for CNP in the GNR device was 60 nA at $V_{BG} = 0$ which is higher than the GNM device. This can be due to two reasons,

The tensile stress on the non-meshed side is expected to highly suppress the conductance in that region. This kind of strain can highly suppress the conductance at the non-meshed regions [79]–[81]. With 100 nm non-meshed region in this device, the central meshed area exerts some stress to the non-meshed side and sinks slightly, which is discussed in the fabrication chapter by showing the non-linear distribution of the nanopores and can be observed from the secondary HIBM image of the meshed structure.

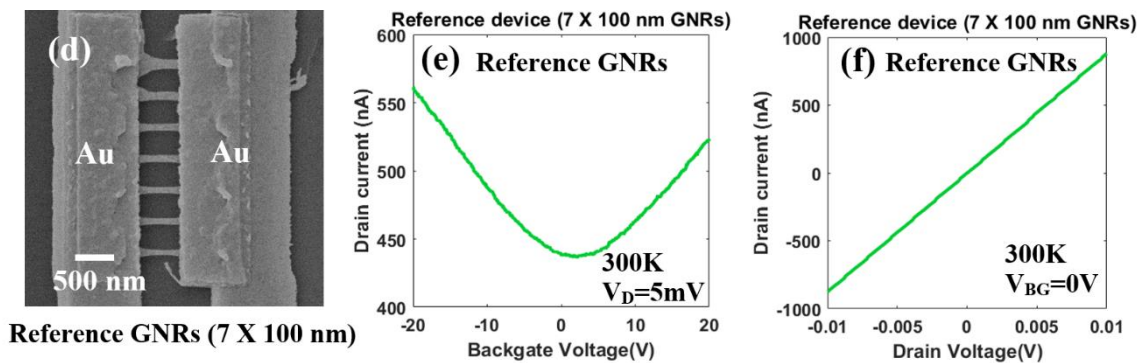


Figure 5-9 Left: Fabricated reference device for comparison of the CNP. 7 suspended parallel devices each with 100 nm width were fabricated for this purpose. Middle: $I_D \sim V_{BG}$ trend at a constant V_D and base temperature 300 K shows average CNP appears at $V_{BG} = 0$. Right: linear $I_D \sim V_D$ characteristics for $V_{BG} = 0$ and 300 K base temperature is observed for the same device.

From fig. 5.8 (c), there was no transport gap opening observed. This implies that the stress on the non-meshed 100 nm region was not enough to open a band gap and a small amount of current could still flow in room temperature. Keeping this mind, $I_D - V_D$ measurement was carried out for GNM devices with different pitches as shown in fig. 5.10. All of these devices had non-meshed regions of the same dimensions. Despite that, it was possible to observe the effect of pitch on the $I_D - V_D$ characteristics of the GNMs. From this observation, for this measurement, the 100 nm non-meshed region was counted out of the conductance analysis. At the same time, it is to be noted that the non-meshed region is a notable part of the GNM device both in mechanical and electrical properties.

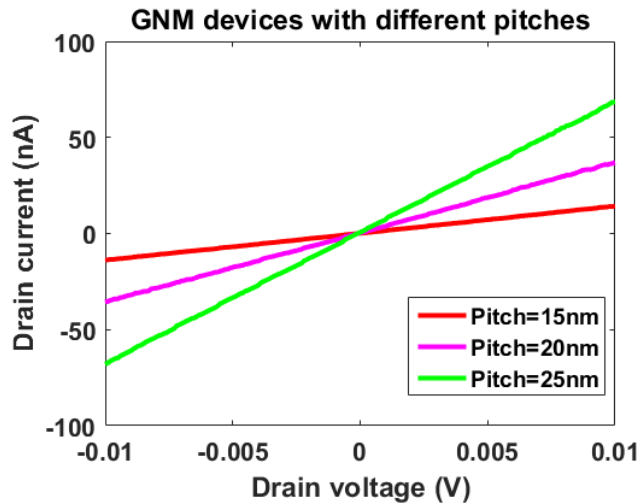


Figure 5-10 The characteristic linear $I_D - V_D$ trend observed for different GNM devices with varied pitch sizes.

5.4 Thermal characterization

5.4.1 Calibration of reference electrode

The measurement result of the conventional $I_D - V_D$ characteristics of the gold nanowire is shown in fig. 5.11 (a). The characteristic Ohmic property is observed by sweeping source current between -1mA to 1mA. By extracting the slopes of the plots corresponding to different stage temperatures, we can see that the resistance of the metal nanowire increased linearly as a function of temperature.

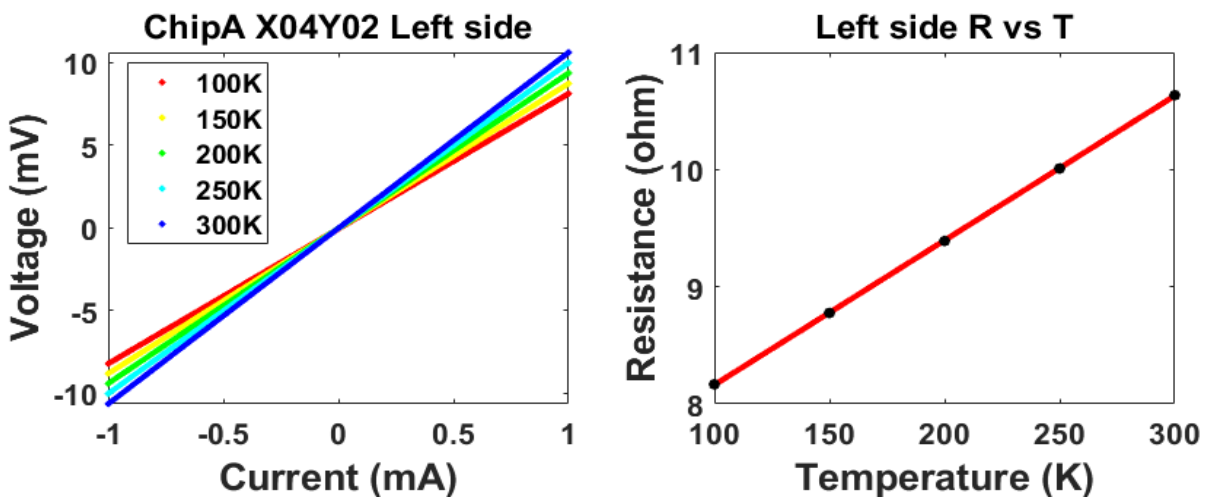


Figure 5-11 Left: The characteristic linear $I_D - V_D$ trend observed for left side reference electrode at different base temperatures. Right: resistance of the metal electrode as a function of temperature.

Similar characteristics were observed for the electrode on the right side as well, as shown in the following figure. For rest of this chapter, the left and right electrode will be analogous to the schematic figures.

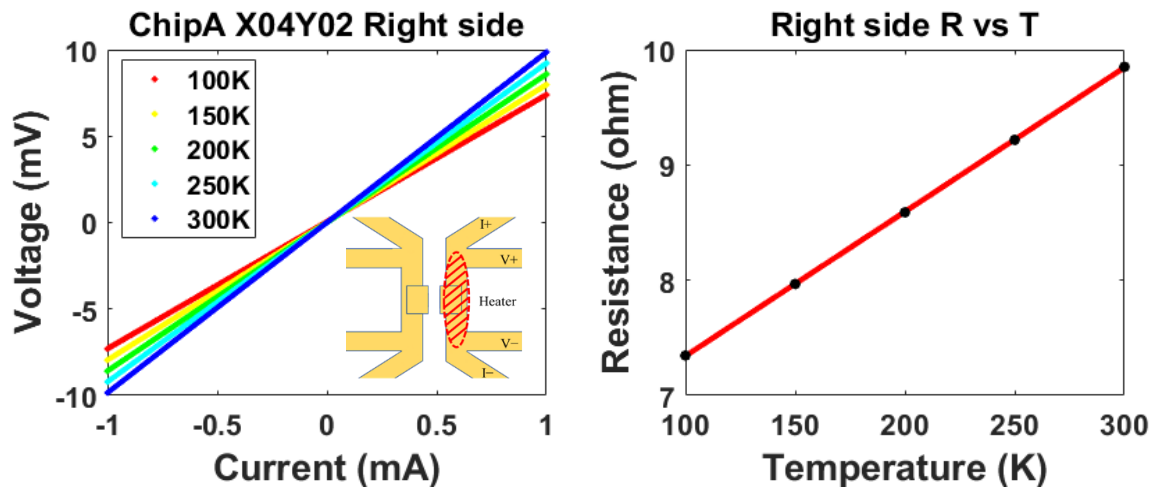


Figure 5-12 The $I_D - V_D$ characteristics of the right side reference electrode at different base temperatures. Right: resistance of the metal electrode as a function of temperature.

Next, to realize the joule heating effect on the heater, we took a constant base temperature at 150K and applied high current to generate temperature at the source. The current sweep was maintained from 5mA – 20 mA. From fig. 5.12, we can see that the resistance of the metal increased linearly as the applied current increased which can be attributed to resistance heating at the wire.

The corresponding power to the applied current can be obtained from the relation $P = I^2 R$.

From the linear plot, the temperature can be obtained by exercising the relationship $y = bx + a$, which can be re-written for resistance and temperature relationships as,

$R = b.T + a$, where b is the slope of the plot and a is the intercept in fig. 5.13(b).

As shown in fig. 5.14 (right), we can now establish the relationship between the applied power and corresponding temperature. The temperature obtained at this point is the temperature at the metal wire without any graphene, which will be addressed as T_h^{NG} where NG corresponds to 'No

graphene' and h corresponds to 'heater'. This nomenclature is followed throughout the rest of the report.

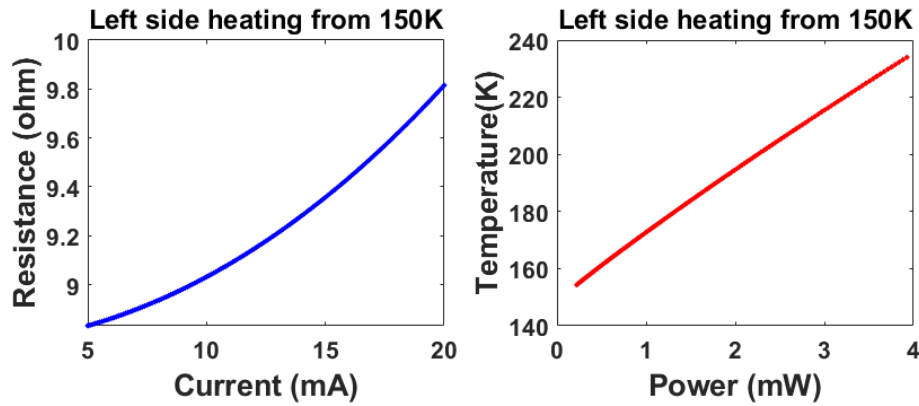


Figure 5-13 Left: heating characteristics of the left side metal electrode as a function of applied current. Right: temperature dependence of the metal electrode as a function of applied power.

We carried out a similar measurement for the electrode on the right side, essentially changing the position of the heater. A similar trend is observed as shown in the following figure.

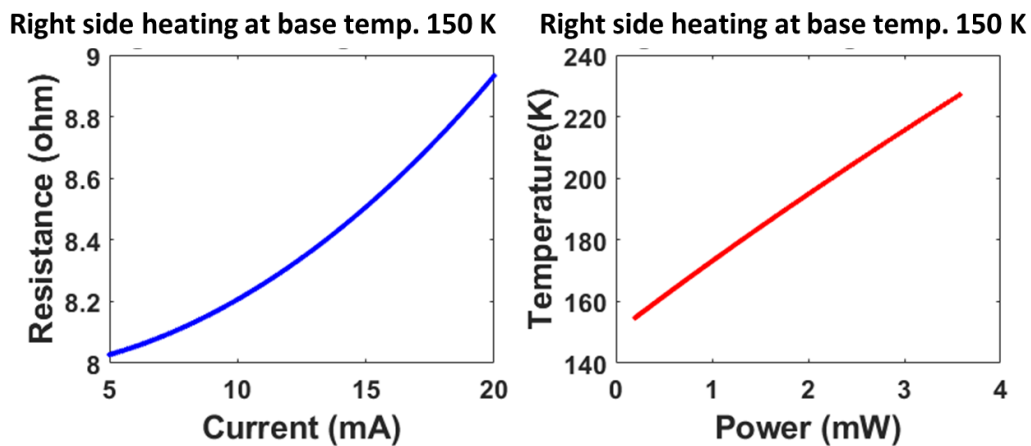


Figure 5-14 Left: heating characteristics of the right side metal electrode as a function of applied current. Right: temperature dependence of the metal electrode as a function of applied power.

After establishing the process, we normalized the temperature to the corresponding power for 4 different devices possessing the same material characteristics and dimensionality in design. From fig. 5.11, we can see that the characteristic linear trait for all the devices are fairly in agreement

which gives us statistical evidence to normalize the plot in fig. 5.15 (b) and use it as the reference for the left side electrode. The similar method is applied for the same devices in the same measurement conditions for the right side electrode, and also in this case we got statistically agreeing normalized plot as shown in figure 5.16.

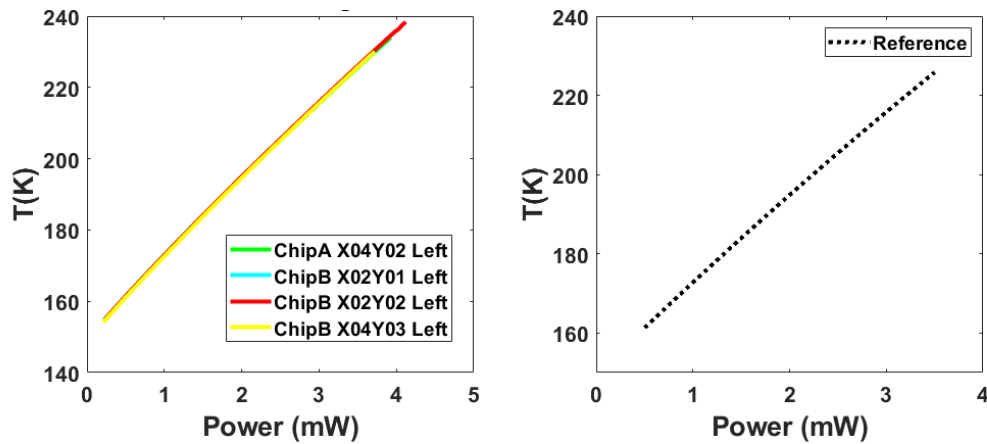


Figure 5-15 Normalized temperature of the left side electrodes of 4 devices as a function of power.

Heating characteristics of metal electrodes (right) without graphene at 150K base temp.

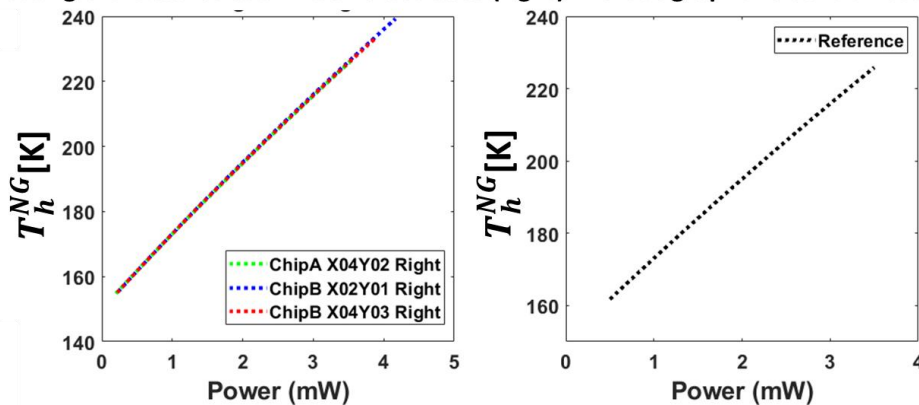


Figure 5-16 Normalized temperature of the right side electrodes of 4 devices as a function of power.

5.4 Thermal characteristics of half-meshed GNM

Taking the measurement process discussed in the previous section as standard, we now proceeded to observe the thermal characteristics of the half meshed GNM as shown in the following figure. The suspended GNR was patterned by helium ion milling on the right half side.

The different pitch were 20, 25 and 30 nm.

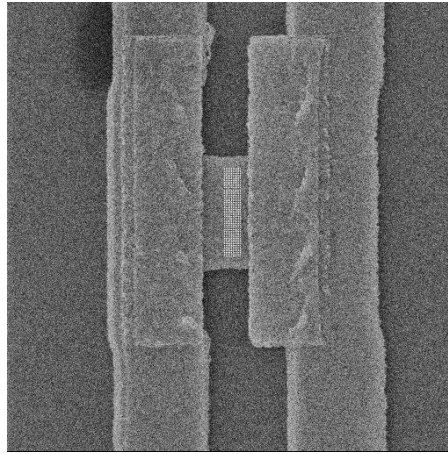


Figure 5-17 SEM image of the half-meshed GNM device.

By maintaining the same measurement conditions as discussed in the previous section, we obtained the temperature at the heater for the half meshed device. This temperature is addressed as T_h^G as shown in the following figure.

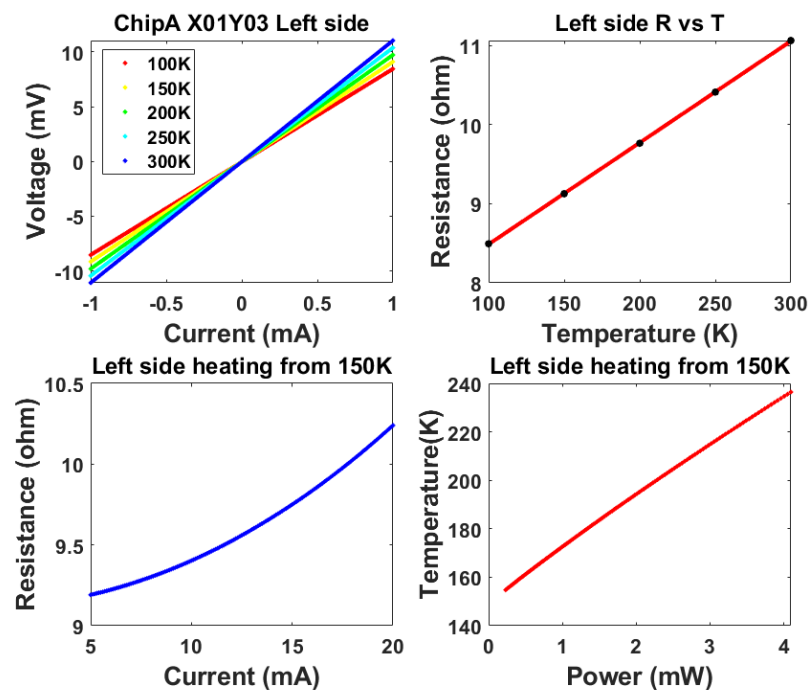


Figure 5-18 $I_d - V_d$ characteristics of half meshed GNM device as measured on the left side. Thermal dissipation is from the non-meshed side to the meshed side.

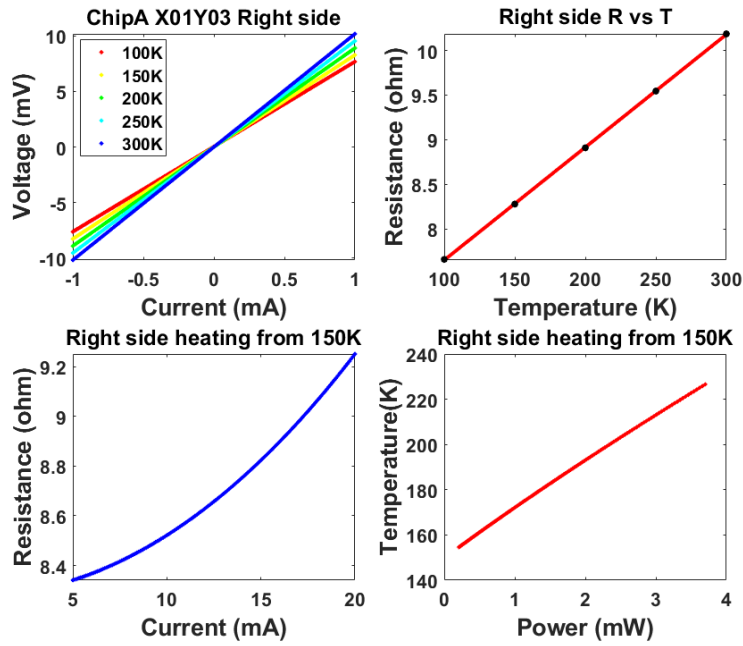


Figure 5-19 $I_d - V_d$ characteristics of half meshed GNM device as measured on the right side. Thermal dissipation is from the meshed side to the non-meshed side.

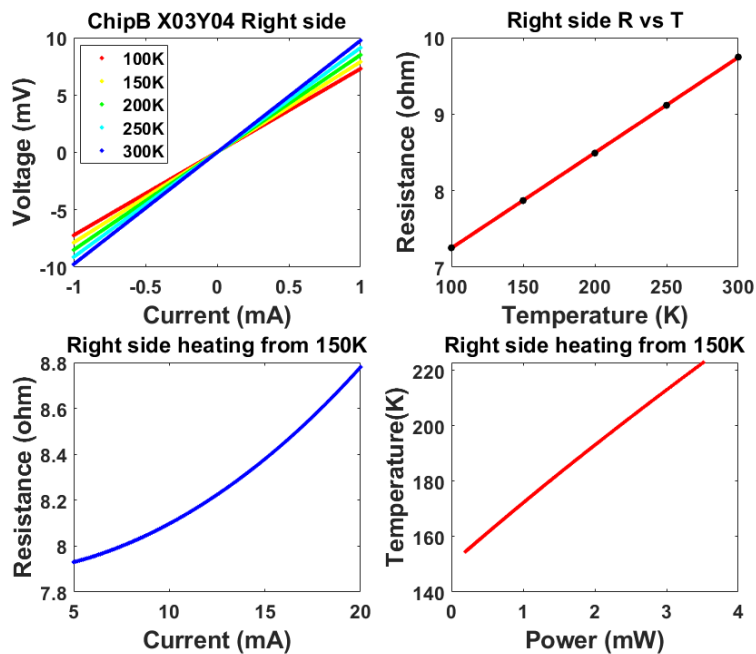


Figure 5-20 $I_d - V_d$ characteristics of half meshed GNM device with 30 nm pitch as measured on the right side. Thermal dissipation is from the non-meshed side to the meshed side.

The T_h^G for the right side electrode can be also obtained for the half-meshed device as shown in fig. 5.19. For comparison and better understanding, we took another half-meshed device with 30 nm pitch and performed the same measurement as shown in figures 5.21 and 5.22.

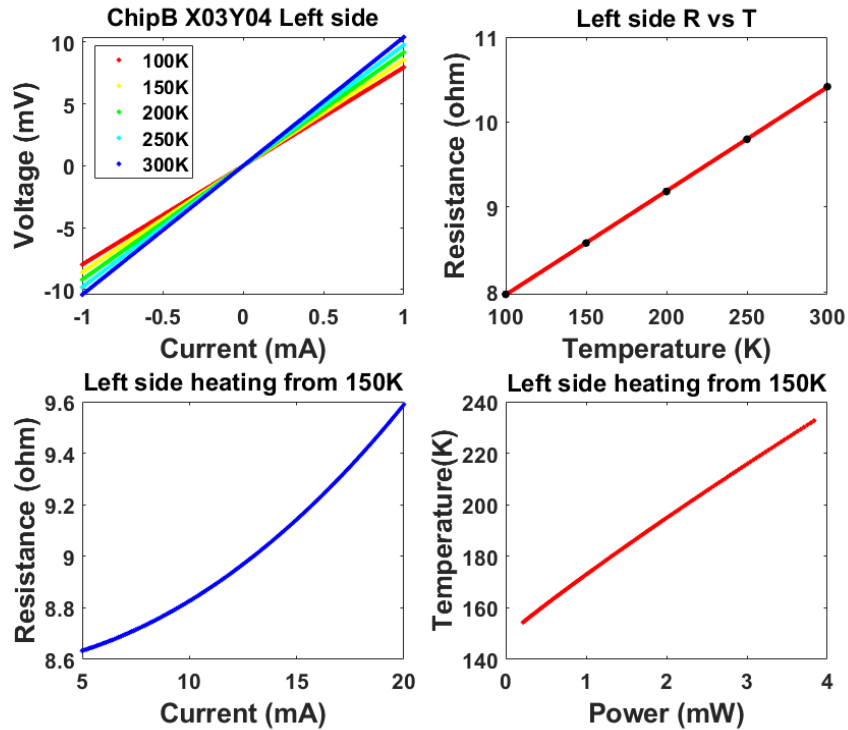


Figure 5-21 $I_d - V_a$ characteristics of half meshed GNM device with 30 nm pitch as measured on the left side. Thermal dissipation is from the meshed side to the non-meshed side.

5.4 Discussion

By applying the principle of resistive heating, we were able to measure the change in resistance at the electrode with and without any GNM present. The temperature was calculated at the heater as a function of power. When there is no graphene present, i.e. reference electrode, we measured a temperature T_h^{NG} where NG means ‘no-graphene’ and the subscript h means ‘heater’. At a base temperature of 150 K, a current from 5 mA to 20 mA was swept at the heater. Where there is no graphene present, it is expected that no conductive heat transfer takes place. As the measurement is carried out in 10^{-7} MPa vacuum condition, the radiative and convective heat transfer is expected to be negligible. Next, when we have GNM present, some amount of heat is expected to be transported through the GNM and the measured temperature at the heater, T_h^G , is expected to be lower than T_h^{NG} . From the difference of these two values we will have ΔT , which is the difference

of these two values and can be written as,

$$\Delta T_h = T_h^{NG} - T_h^G \text{----- (5.1)}$$

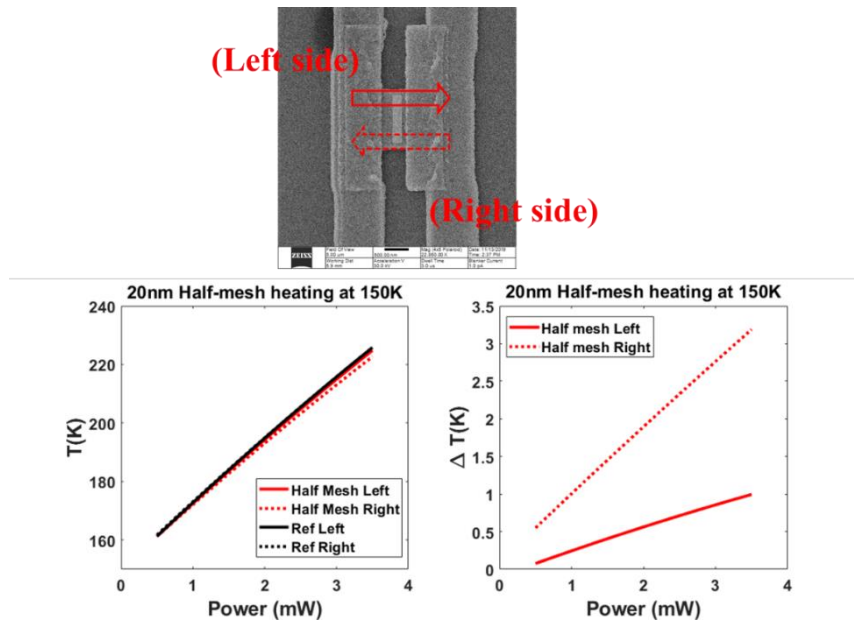


Figure 5-22 Heating characteristics of the half-meshed device with 20 nm pitch. By extracting the heating data for the left and right side of the half-meshed device, a difference in thermal transport is detected.

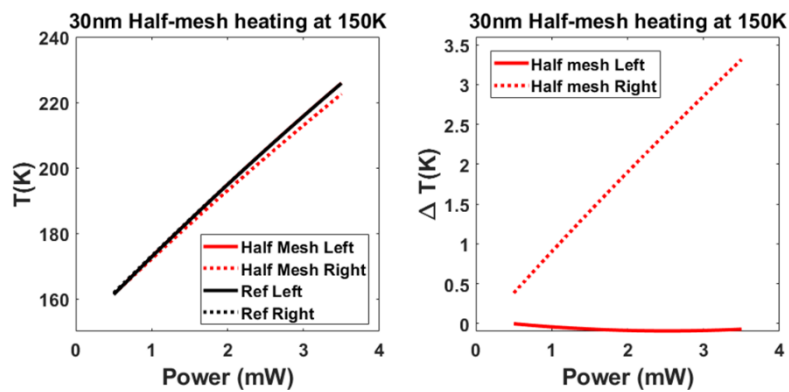


Figure 5-23 Heating characteristics of the half-meshed device with 30 nm pitch. By extracting the heating data for the left and right side of the half-meshed device, a difference in thermal transport is detected.

From the figures 5.22 and 5.23 we can see that when compared to the reference devices, the half mesh devices showed slight deviation. When we extracted the temperature against power for the left and right side heaters for the half meshed devices, both 20 nm and 30 nm pitch devices showed strong difference in thermal transport as the heater position was changed. In fig. 5.24, we extracted similar data for the fully meshed devices.

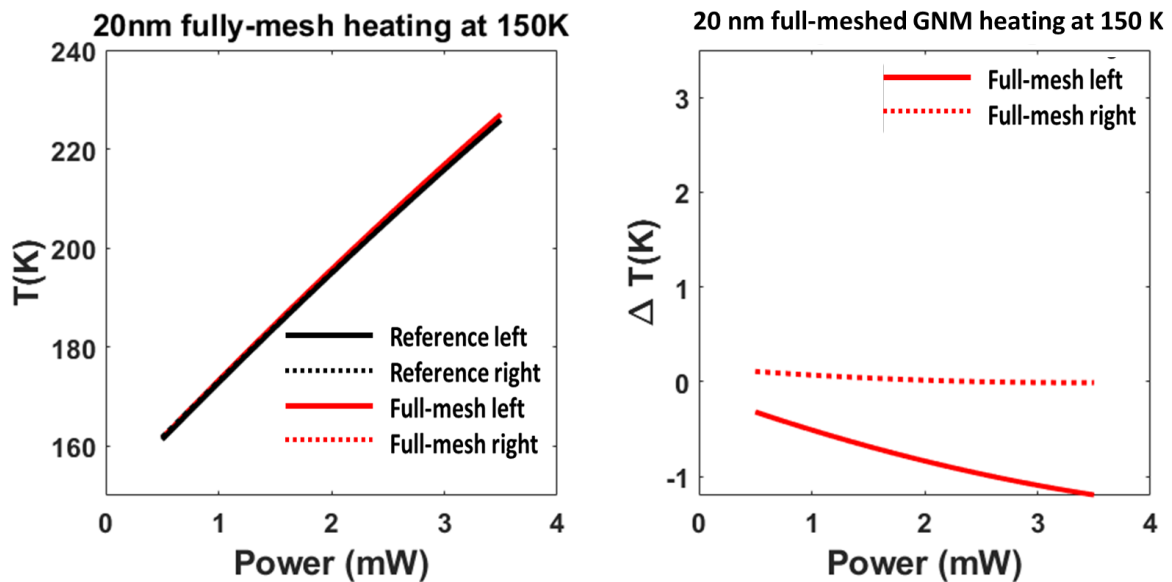


Figure 5-24 Heating characteristics of the fully-meshed device with 20 nm pitch. By extracting the heating data for the left and right side of the full-meshed device, the difference in thermal transport is negligible

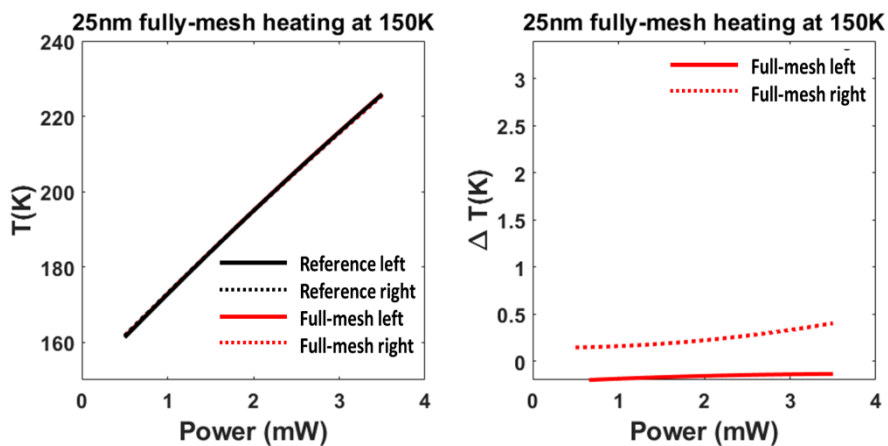


Figure 5-25 Heating characteristics of the fully-meshed device with 25 nm pitch. By extracting the heating data for the left and right side of the full-meshed device, the difference in thermal transport is negligible

Both for the 20 and 25 nm pitch fully meshed devices, the difference in thermal transport when the heater position is changed is almost negligible. From these two figures we can see that even though ΔT_h value is negligible, there's a slight negative slope for the left side electrodes. We associate it with the fabrication anomalies. Due to the fabrication limitations it is impossible to create absolutely symmetrical metal electrodes and therefore, the actual heat transfer is slightly different. As we cannot avoid this limitation during fabrication, this instrumental error remains while we calibrate the electrode and finally results in this anomaly in the extracted plot. In optimum conditions, we expect that the temperature curves for the left and the right electrode would be superimposed on each other.

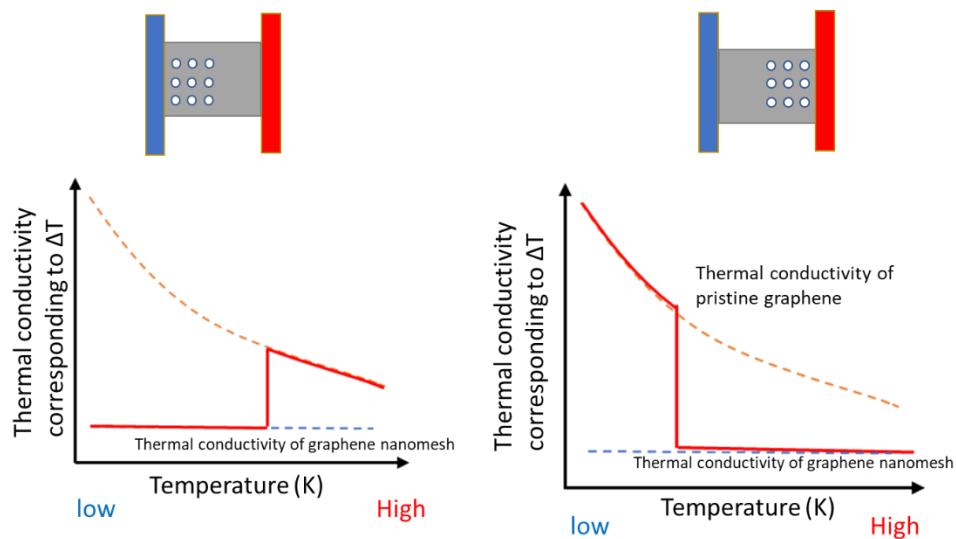


Figure 5-26 Trend of thermal asymmetry observed in the fabricated GPnCs. The thermal transport is observed to be lower when the heater position is on the pristine graphene side of the fabricated GPnC compared to when the heater position is changed to the meshed side of the fabricated GPnC.

In fig. 5-26, a qualitative analysis of the thermal rectification observed in the fabricated sample is shown. The thermal conductivity of pristine graphene is shown by the red dotted line and the thermal conductivity of the meshed graphene is represented by the blue dashed line. The solid red line shows the trend in thermal transport from the meshed to non-meshed area on the left side, and vice versa on the right side. Now, the thermal conductivity of pristine graphene shows an obvious trend of decrease as the temperature is increased. It is due to the Umklapp scattering in graphene that increases with the increase in temperature [34], [52], [82], [83]. As we introduce the nanopores, that induces more scattering sites for phonons which becomes more significant and the thermal conductivity slope for the nanomeshed sample becomes more or less constant with increasing temperature. Therefore, when the thermal transport is from the meshed to the non-meshed side (that is, the heater is placed on the meshed side) the overall thermal transport

is smaller compared to when the heater position is changed to the non-meshed side as shown by the solid red line in fig. 5.26. A similar study has been reported by Wang et al., where they created the asymmetry by milling randomized nanopores on suspended GNR [84].

To summarize this chapter, we have established a thermoelectric measurement method to observe the change in thermal transport in GNM devices. By comparing thermal transport in symmetric (full meshed) and asymmetric (half meshed) devices, we observed thermal rectification nature in the asymmetric GNM device. To understand the physical mechanism of the rectification phenomenon is our next step in this work.

Chapter 6

Conclusion and future tasks

6.1 Conclusion

Controlling the thermal conductivity of a material independently of its electrical conductivity has always been an intriguing aspect for practical applications of thermoelectric materials. Fabricating phononic crystals to induce increased boundary scattering of phonons has been a topic of interest for a while now. The high in-plane thermal conductivity and high Young's modulus make it a more desirable candidate to manipulate THz regime thermal phonon frequencies. Numerical analysis explaining the reduction of thermal conduction due to phonon blockade has been reported for both Si and graphene. Even though for actual experimental works, Si is still very popular due to ease of fabrication, but, any Si based phononic crystal systems applicable for room temperature applications have not yet as the workable phonon frequency range in SiPnC is still in the low GHz regime [8], [85]–[87]. Realizing the superior physical properties of graphene to be more favorable for this case, I worked on fabricating graphene phononic crystals in this project. Until now, the following points are noteworthy.

- In this thesis, I have first shown by numerical simulation that, by using graphene, we can achieve phonon blockade in the THz regime by introducing periodic structures with nanometer range periodicity. This analysis opened up the possibility to experimentally fabricate graphene phononic crystals because the periodicity of the phononic structures suggested by the simulation appeared to be achievable using the available nanofabrication techniques like EBL and HIBM.
- From FEM simulation, it was shown that by introducing snowflake shaped GPnC in a hexagonal unit cell layout, it is possible to obtain THz phonon bandgaps for wide range of neck lengths, which is important from the fabrication point of view for feasibility and flexibility in dimensional control.

- To be able to achieve the high-resolution nanopore arrays suggested by the simulation, HIBM is a decent tool providing small beam diameter and controllability. In collaboration with my colleague, the process for fabricating the GnPC using HIBM was established. In the first step of this process, buffered hydrofluoric acid (bHF) was used for a certain time to etch away SiO_2 and suspend the GNR between two anchor electrodes. Afterwards, it was exposed to HIBM to create nanopores with a radius of 3-4 nm and pitch as low as 11 nm. It is to be mentioned that, for the actual measurement presented in this report, we chose the devices with 15 nm pitch and ~ 6 nm diameter. Also, by fabricating full-meshed and half-meshed GnPC, we introduced different devices to measure. This allowed us to measure the thermal transport through the GnPCs of variant configurations. We focused on the half meshed GnPC which corresponds to the asymmetric crystal. For comparison, we used the full-meshed GnPC under same measurement conditions.
- The feasibility of the phononic crystal can only be justified by the proper thermal measurement method. A proper electrothermal measurement method is established based on the concept of 4-probe measurement method. We were able to accurately detect the change in resistance in the GNR with the change in temperature. Metal electrodes and sensors are fabricated on the suspended graphene, one of which is used as a heater and the others are used as the sensors. Heat is generated by applying some electrical current at the heater, which travels through the graphene sheet contributing to increase the temperature at the sensor.
- Thermal rectification phenomenon has been observed in the asymmetric GnPC. For fully meshed devices, we observed symmetric electrical and thermal transport. For the half meshed devices, symmetric electrical transport and asymmetric thermal transport were observed. We observed that the heat flow through the asymmetric GnPC is higher from the meshed side to the non-meshed side when the temperature gradient is maintained the same. The opposite phenomena is true when the heater position is swapped.

6.2 Future work

Maximizing phonon transport: The issue of electrical leakage current

It has been reported that the estimated electrical thermal conductivity in graphene is about 1% of that of the total thermal conductivity [22] [21]. So it is established that most of the heat transported through graphene is phonon transport. However, for the resistive thermometry that we employed, it is difficult to argue that the electrical transport through graphene will have

negligible effect on the increased resistance on the sensor. For the future endeavors, it is advisable to address this issue. To limit the electrical transport during this measurement while maintaining the thermal transport, there are two possible ways.

- a. The first proposal is to introduce a layer of electrically insulating thermal conductor between the metal electrodes and graphene. Hexagonal boron nitride is one such material possessing a similar lattice structure as graphene and a wide direct electrical bandgap of 5.8eV and a thermal conductivity of ~ 400 W/mK. To include a layer of hBN will require an additional step of EBL and RIE process. But the measured thermal conductivity of this device might be able to answer the questions about the electron contribution to the heat transfer through graphene.

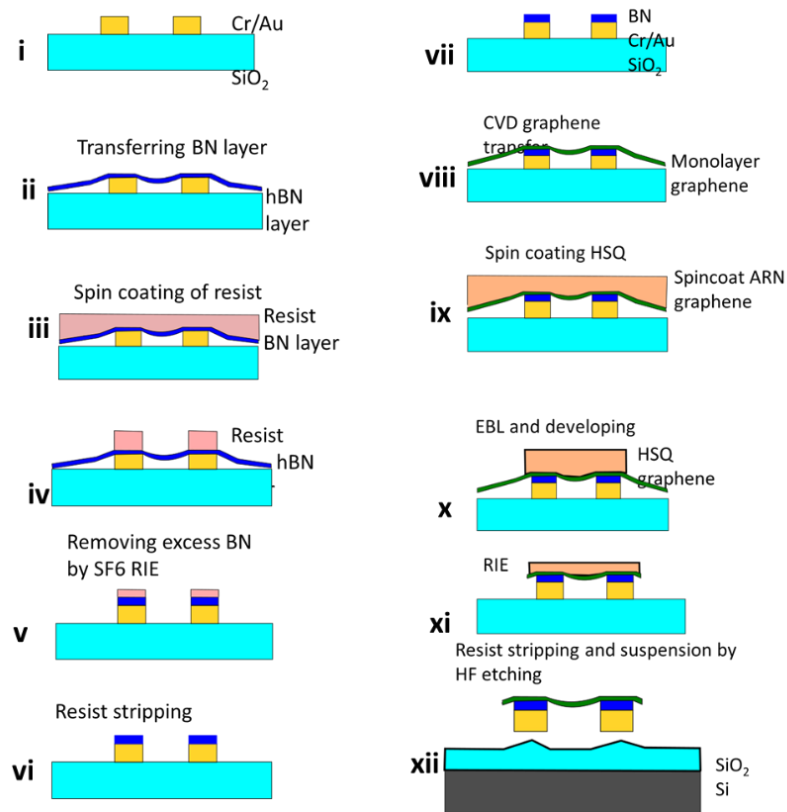


Figure 6-1 Schematic representation of the device fabrication process with hBN as an electrically insulating thermal conduction layer

Another way is to utilize the chromium oxide. As discussed in chapter 3, during the fabrication of metal electrodes, we deposit chrome to increase the adhesion with the metal. One interesting aspect of chrome is that, when exposed to air, it oxidizes into a few nanometer of chromium oxide (Cr_2O_3). This (Cr_2O_3) is also a hexagonal symmetry material with a lattice parameter of 2.49 \AA .

While the high electrical resistivity of Cr₂O₃ has been reported, the thermal conductivity of Cr₂O₃ has not been well studied. However, using Cr₂O₃ makes the fabrication process easier compared to the hBN transfer process. All we need to do is expose the deposited chromium to external air. A few devices has already been fabricated in this method and the I_d - V_d measurements show lower electrical conductivity compared to the devices without oxidized Cr. The Cr₂O₃ devices are still under investigation for thermal conduction properties.

- b. The second method is to separate the heater complete from graphene. By increasing the surface area of the heater like the device shown in 5.1 (a) should increase the temperature. The radiative heat transport, if high enough, should be measurable at a nearby sensor fabricated on graphene. If the similar thermal transport relationship as discussed in chapter 4 can be obtained from such device, we can readily justify the independent phonon transport through the GNR without any contribution from the electrons.

Appendix

Development of heat spreader method for thermal characterization

Determination of the thermal conductivity of a material is of great interest because it contributes to the performance of thermoelectric materials and thermal management in electronic circuits. Thermal conductivity is a property of the material that depends on the parameters such as structure, density, porosity, electrical conductivity etc. Thermal conductivity of a thin film material is usually smaller than their bulk counterpart. For example, at room temperature, κ of bulk Si can be a factor of 5 magnitude higher than a Si thin film of 20 nm [31] [28]. And κ along the plane of a single layer of encapsulated graphene is at least 10 times smaller than the corresponding value for bulk graphite [88]. Two reasons could be associated with such reduction in thermal conductivity,

- a. The techniques available for thin film synthesis technologies are not perfect, and result in impurities, disorder, and grain boundaries which contribute in reducing the thermal conductivity,
- b. Even for atomically perfect thin films, the effects of scattering, phonon leakage and related interactions become more important in the nanoscale. Both basic mechanisms generally affect in-plane (k_x) and crossplane (k_z) transport differently, so even for bulk materials that are isotropic, the thermal conductivity in thin films is usually isotropic.

In this section, I will discuss the methodology of a electrothermal measurement system for measuring the thermal conductivity of supported monolayer graphene. Graphene, a material with extremely high in-plane thermal conductivity, has the possibility to work as a phononic crystal. It is expected that GnPC will exhibit lower thermal conductivity compared to pristine graphene.

A-1 experimental setup for the thermal measurement

Electronic transport in graphene has been extensively studies since it's isolation. But the

experimental challenges limits the methods of understanding the thermal properties. As discussed earlier, a method for measuring room temperature thermal conductivity of suspended graphene has been reported using the heat generated with the laser beam of RAMAN by Balandin et. al. [21], [32], [40] . Malekpour et. al. measure the thermal conductivity of graphene laminate films deposited on polyethylene terephthalate (PTE)[49]. The obtained values range from about $3000 \text{ Wm}^{-1}\text{K}^{-1}$ to $5000 \text{ Wm}^{-1}\text{K}^{-1}$, which is much higher than diamond and graphite. However, the temperature (T) sensitivity of the RAMAN techniques, the k-T behavior for the 2D system has not yet been understood properly. Also, these measurements were performed on supported graphene. the charge mobility of graphene supported on SiO_2 should be 10 times suppressed compared to the supported graphene [73]. An intricate method of measuring the thermal conductivity of supported graphene by using the theory of resistance thermometry has been reported [89]. The sensitivity of four-terminal thermal resistance sensing gives us the freedom to employ the idea for measuring the thermal conductivity of supported and suspended graphene. The study will further be extended for graphene nanomesh structures i.e. graphene phononic crsytals.

As discussed before, the relationship between the rise in temperature and the resistance of the nanowire is given by the following equation,

$$R = R_0 (1 + \alpha\Delta T) \text{ ----- (5.2)}$$

Here, R_0 is the wire resistance at $\Delta T = 0$ and α is the temperatuer coefficient of resistance (TCR).

From this, we can say that,

$$\Delta T = 1 / \alpha R_0 \text{ ----- (5.3)}$$

$$\text{or, } dT/dR = 1 / \alpha R_0 \text{ ----- (5.4)}$$

this is a linear relation, which should be obtainable for any metal. From this equation, we can obtain TCR for gold.

The measurement system that we established can be considered as a modified heat spreader method. The aim is to be able to create a thermal gradient across a sheet of graphene and measuring the change in temperature at different distances from the heater. The basic idea of this measurement comes from resistive thermometry, which is measuring the corresponding change

in resistance of a material with the change in temperature. When resistance is measured with a simple multimeter, the resistance of the cables leading to the sample and any resistance at the contacts is measured as well. The contact resistances can be a serious problem when the electrical contact is made using micromanipulators or scaled down to the nanometer regime. In fig. A-1, the schematic of the 4-probe measurement method is shown. The concept is discussed earlier in chapter 5 of this thesis.

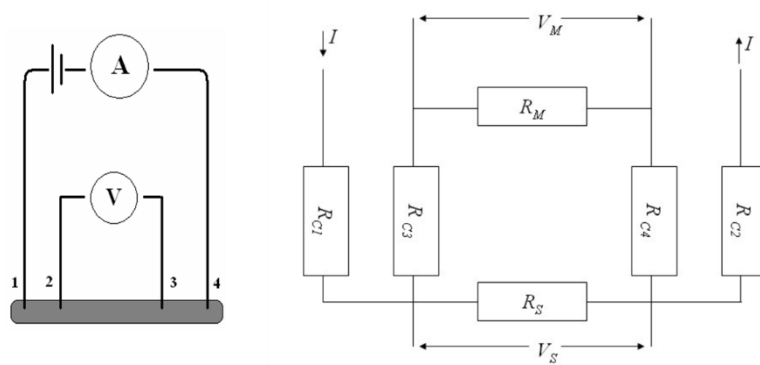


Figure A-1 Schematic representation of the 4-probe electrothermal measurement

A-2 Measurement of thermal transport in supported graphene

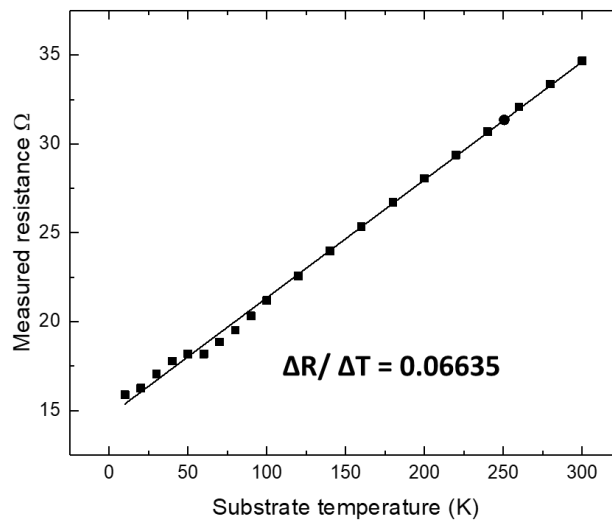
A KEITHLEY 4200 sourcemeter was used to apply current through the metal contacts and a KEITHLEY 2420 nanovoltmeter was used to measure the resistance at the constriction. All measurements were carried out in vacuum in a variable temperature helium close cycle cryogenic cooling system which can go down to ~ 4.8 K base temperature. To measure the TCR for the gold nanowire, the temperature of the stage was maintained at 10K and gradually increased. For establishing the feasibility of the 4-probe measurement system, at first we measured the temperature dependent resistance of the entire circuit. One concern here was to ensure that the applied current was not contributing itself to increase the resistance of the conductor. Keeping the stage temperature at 10K, we applied a series of small currents with an interval of about 20minutes in between each measurement. The applied currents and their corresponding resistance is shown in the following table.

Table: A-1: Determination of sensing current

Current applied (μA)	Resistance (Ω)
50	163.11

100	162.68
200	162.60
300	162.67
400	162.86
500	163

From this table, it is clear that the resistance of the conductor remained constant within the range of 100-400 μA , before it started raising. Above 400 μA , the applied current itself started contributing to increasing the resistance of the conductor. From this initial measurement, we took 100 μA as the reference current. As shown in fig.5, after adopting the reference current, the measurement was carried out from 5K to 300 K substrate temperature. The increase in resistance is fairly linear to the increasing temperature which satisfies the equation 5.4. The slope of the linear plot represents the value of TCR comprising of the entire circuit. This measurement is necessary to obtain a reference data.



Temperature dependent resistance of the entire circuit

Figure A-2 Increase of resistance at the metal conductor with increasing temperature of the substrate.

As shown with the FEM simulation for joule heating in the previous chapter, it is necessary to obtain the temperature generated at the gold electrode due to applied current. As shown in fig. A-1, 4-terminal measurement was employed. The KEITHLEY 2182 nanovoltmeter offers low noise measurements at high speed. This feature is extremely useful for us, as it helps reducing the

measurement time and therefore, we can argue that the small current applied during thermal sensing does not or negligibly contribute in increasing the temperature of the sensor itself. The experiment was conducted again in the similar fashion as the two-terminal method. The temperature variation of the stage i.e. the substrate temperature was maintained the same as the reference measurement. As shown in fig. A-2, also in this case, the resistance of the gold nanowire increased linearly with increasing base temperature. The TCR was calculated from the slope of the linear plot and the value was 0.00314 which is in good agreement of the already reported value of 0.003715 [89].

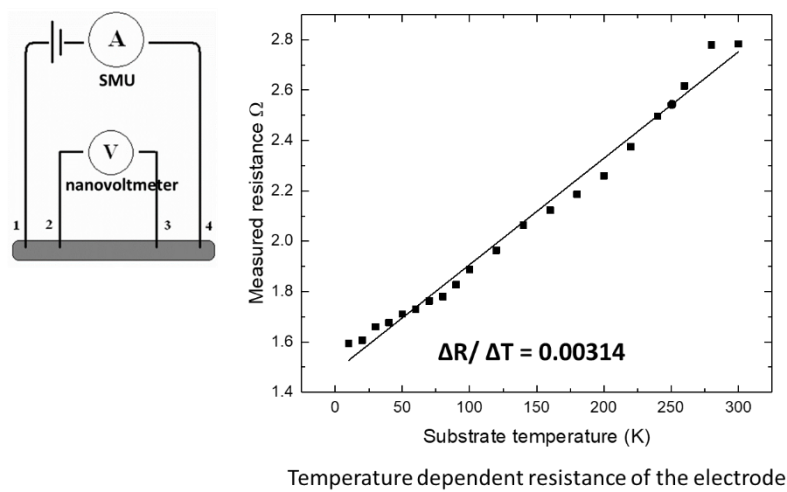


Figure A-3 Increase of resistance at the metal electrode with increasing temperature of the substrate. The calculated value of TCR is in well agreement with literature.

Next, we increased the temperature at the electrode by applying higher current at the terminal. From this point onwards, the base temperature was kept constant at 10K. We were able to measure the change in resistance, R_{source} , of the gold nanowire at different current, which is denoted as I_{source} .

We can rewrite eq. 4.2 as,

$$R = R_0 (1 + \alpha (T - T_0)) \text{ ----- (4.5)}$$

With this experiment, we have established the 4-point probe thermal measurement setup with high resolution nanovoltmeter.

By replacing the obtained value of α and T_0 as 10K, we calculated the temperature T at the gold electrode from the plot shown in fig. 7. It is to be noted that from now onwards, the subscripts 'source' and 'measure' will be used to denote the heater and sensor in the circuit respectively.

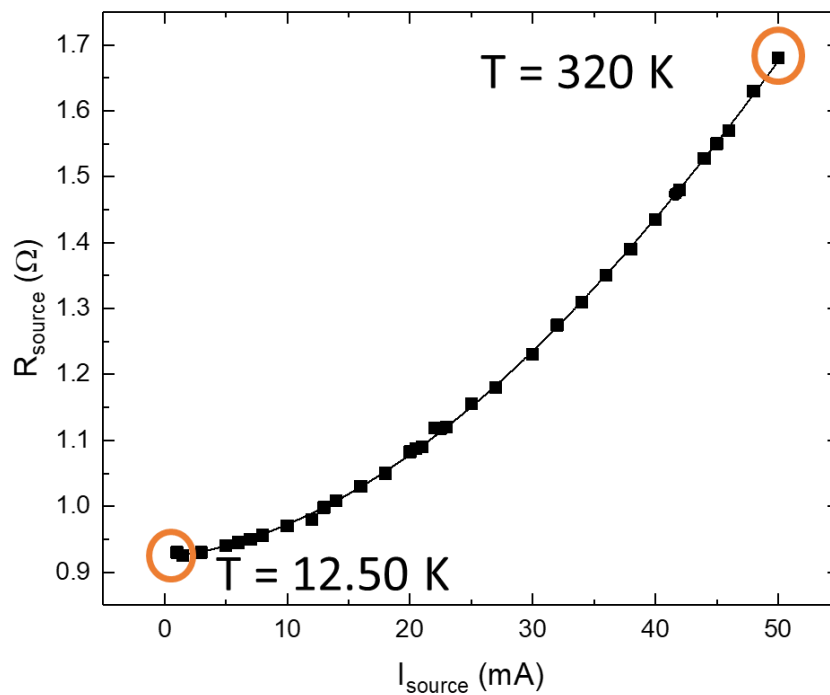
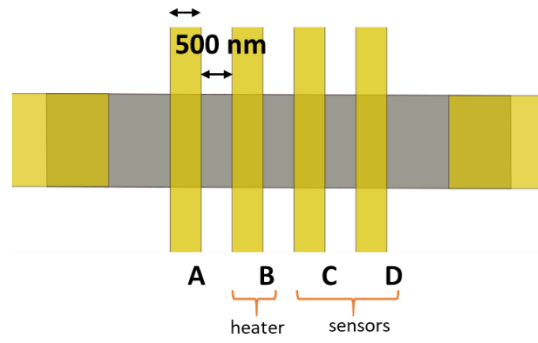


Figure A-4 Calculated temperature at the electrode with respect to applied current.

To measure the thermal transport through graphene, we extended this measurement for a configuration where one of the electrodes was considered as a heater. The other electrodes at different distances from the heater were configured as the thermal sensors as shown schematically in the following figure.



Heater	Sensor
C	D
B	C
B	D

Figure A-5 Possible combinations of heater and sensor on the device.

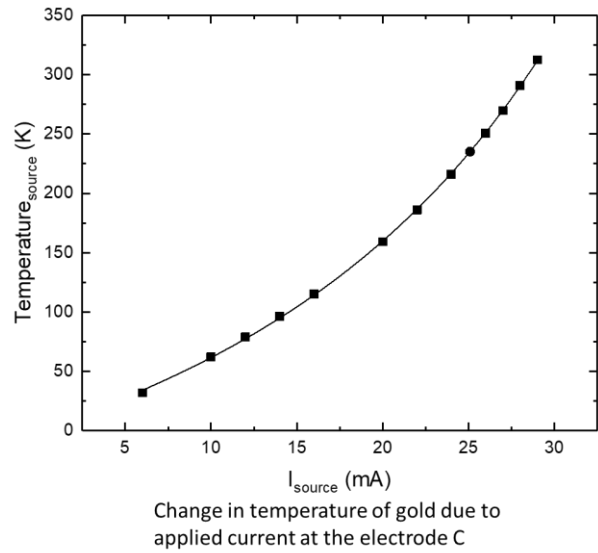
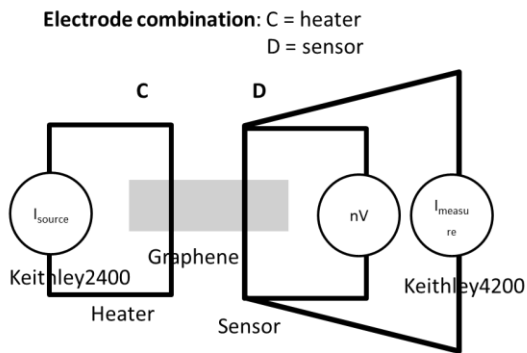


Figure A-6 On the left, the established circuit for thermal measurement is shown. On the right the temperature rise at the electrode with respect to the applied current is shown.

Ideally, the measurement should be carried out in a condition where both the heater and sensor are connected to a 4-probe measurement system. To do that, we would need a system with 8 or more probes. Currently our Nagase prober system provides the assembly suitable for measuring using 6 probes only. Therefore, we used the 4-probe measurement for the sensor electrode. The heater was connected to a KEITHLEY 2400 source meter for supplying current. The experimental setup is shown schematically in the following figure. The possible heater-sensor combinations are shown in fig. A-6(a). The current dependence to the generated temperature for this electrode followed the same trend as before.

After establishing and optimizing the measurement method for the heater and sensor respectively, we proceeded to measure the actual thermal transport through graphene. Using the same circuit combination.

As shown in fig. A-7, we were able to measure the change in temperature at the sensor by varying the current at the heater. Similar to the process described before, the sensing current has been determined as shown in the following table. In this case, we chose 200 μA as the sensing current. The calculated temperature at the sensor was plotted against the calculated temperature at the heater due to current applied from 5mA to 30 mA. The data points show a fairly linear trend which is in well agreement to the fact that the temperature at the sensor is directly related to the temperature at the heater.

Table A-2 Determination of sensing current

$I_{\text{measure}} (\mu\text{A})$	$R_{\text{measure}} (\Omega)$
50	4.3
100	4.1
200	3.9
300	3.9
400	3.88

500	3.8625
-----	--------

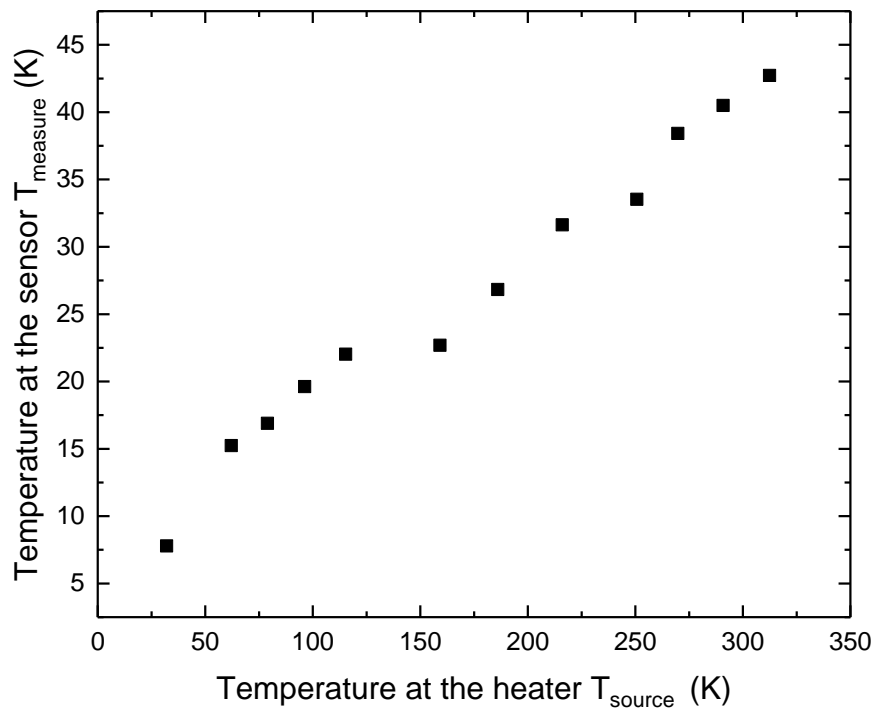


Figure A-7 Change in temperature at the sensor is observed due to the change in temperature at the heater. The temperature change at the heater is induced by the applied current.

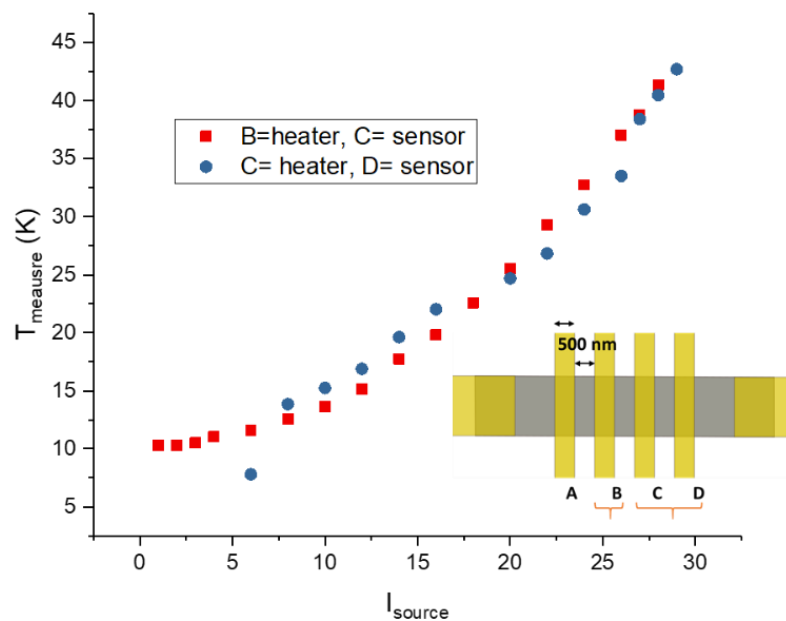


Figure A-8 The thermal transport through graphene is shown here for two different pairs of electrodes. Both pairs have the same distance between them. The temperature dependence at the sensors for both cases show fairly similar characteristics with respect to the applied current.

For the next step, to establish the feasibility for the measurement for the heater-sensor pair, the entire setup was made for a different pair of electrodes. Fig. 4.11 shows the relationship between the two sets of measurements carried out with two different pairs of electrodes. The plot shows that the both measurements deliver fairly similar data. This is the expected outcome as in both cases, the electrodes are of similar dimension and separated by 500 nm graphene in between.

In fig. A-8, the temperature dependence at sensors at different distances from the heater is shown. The red squares in the figure represent the electrode at 500 nm distance and the yellow triangles represents the temperature data point at an electrode 1000 nm away from the heater. From the plot, clear dependence of thermal transport with respect to the distance from the source of heat is observed.

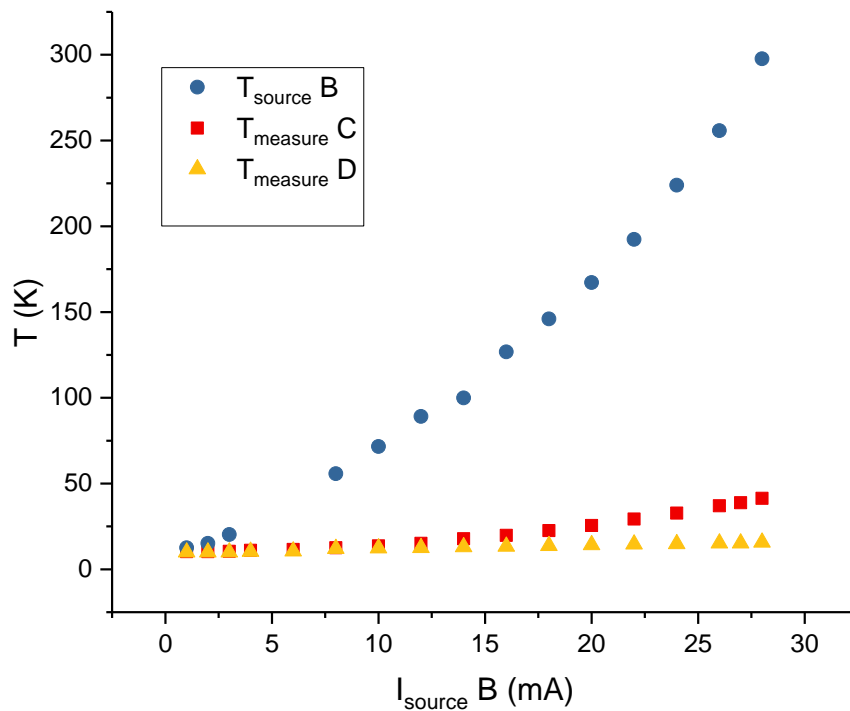


Figure A-9 The thermal transport through graphene at different distance from the heat source is observed. The plot shows clear dependence of thermal transport on distance from the heat source. The electrode that is closer to the heater exhibits higher heat transport trait compared to the electrode further from the source.

A-3 measurement of thermal conductivity of supported graphene

To obtain clear dependence of the thermal transport in terms of distance of the sensor from the heat source confirms the feasibility of the measurement method. To obtain the thermal conductivity of the supported graphene in our sample, we first calculated the resistivity using the following calculations.

$$\text{Thermal resistivity, } R_s = (T_1 - T_2) / A.R \text{ ----- (4.6)}$$

Here, T_1 and T_2 are the temperatures at the heater and sensor, A is the cross sectional area of the nanowire and R is the measured resistance.

$$\text{Conductance} = R_s^{-1} \text{ ----- (4.7)}$$

By multiplying the cross sectional area of the material to eq. 4.7, we can calculate the thermal conductivity k . We calculated the k for graphen considering two cases. For the first one, we included the thickness of SiO_2 which gives $L = 500.3315 \text{ nm}$. For the second case, we took the thickness of conly graphene which is 0.3315 nm . The calculated thermal conductivities are shown in fig. 4.13.

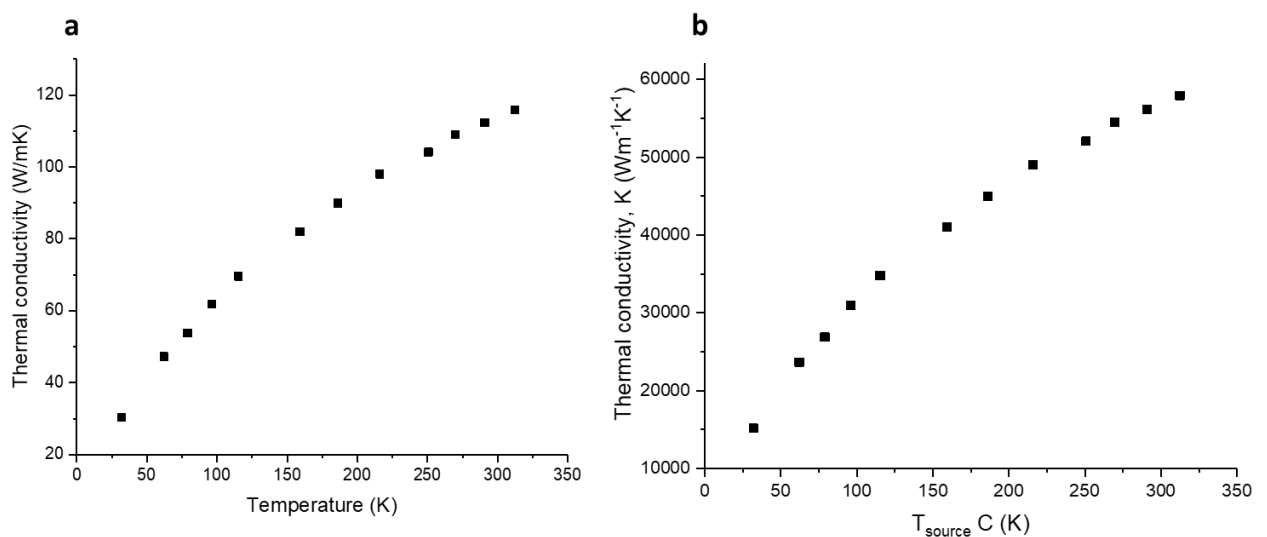


Figure A-10 Calculated thermal conductivity of supported graphene (a) considering total thickness to be 500.3315 nm, (b) considering only the thickness of graphene as 0.3315 nm.

A-4 Extension towards suspended graphene

This experiment provides the reference data to expand this measurement for the supported gNR sample with and without nanopores. The next scheme of the measurement is already established by understanding the thermal transport properties of the suspended cases. It has been observed that the suspended samples are more fragile and also are tricky to be measured. In fig. 4.14, the plot shows the initial measurement for temperature increase with applied current for a suspended gold nanowire. The entire measurement was carried out in similar fashion and similar conditions as discussed until now. However, we have noticed that the gold wires became extremely unsustainable. The heater would fail when the temperature was only around 154 K, at 25 mA applied current.

The possible reason for this kind of failure could be that the heat retained much longer in the nanowire as the SiO_2 was absent after bHF etching. Also, the measurement was done continuously which would also contribute to the joule heating of the wire. For the next measurement, we maintained a cooldown period after each measurement which was 20 minutes. We also reduced the measurement sampling upto 2 seconds. We have already observed that the nanovoltmeter gives stable resistance value almost immediately. In this process we were able to raise the temperature at the gold nanowire upto 308 K as shown in the plot in fig. A-11.

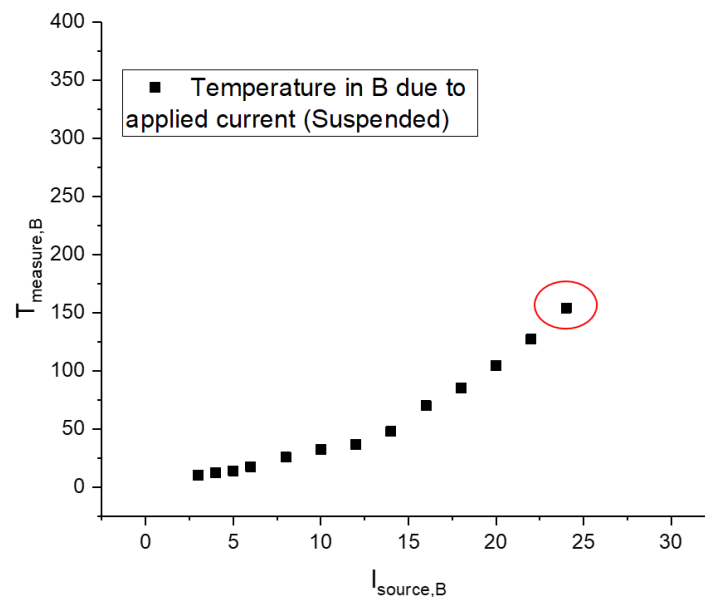


Figure A-11 The highest calculated temperature obtainable with suspended gold heater was about 153.75 K.

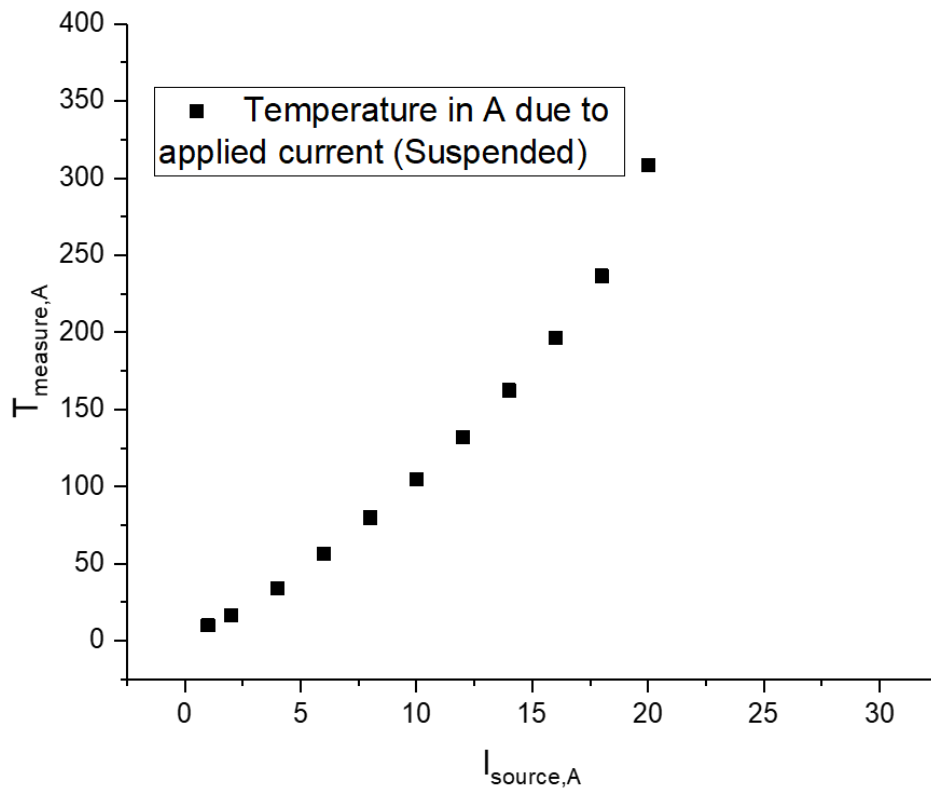


Figure A-12 The highest calculated temperature obtainable with suspended gold heater was about 153.75 K.

This measurement is extremely significant for this project because it supports the idea that the retention of heat at the gold nanowire contributes to the joule heating effect unless it is allowed to be cooled down radiatively.

In conclusion, is important to note the following points,

- The four-probe measurement method has been established for heat spreader samples with supported graphene. compared to TDTR or pulsed laser measurements, this method gives fidelity and flexibility in measurement. Also, the high resolution analyzers provide accurate measurements for minute changes in resistance due to temperature.
- The measurement is now being extended for suspended GNR samples. A reduction of thermal conductivity due to phonon confinement and scattering is expected to be observed for the GnPC samples.

Bibliography

- [1] G. E. Moore, "Cramming More Components Onto Integrated Circuits," *Proc. IEEE*, vol. 86, no. 1, pp. 82–85, Jan. 1998, doi: 10.1109/JPROC.1998.658762.
- [2] A. A. Balandin, "Nanoscale thermal management," *IEEE Potentials*, vol. 21, no. 1, pp. 11–15, Feb. 2002, doi: 10.1109/45.985321.
- [3] E. Pop, "Energy dissipation and transport in nanoscale devices," *Nano Res.*, vol. 3, no. 3, pp. 147–169, Mar. 2010, doi: 10.1007/s12274-010-1019-z.
- [4] M. Maldovan, "Sound and heat revolutions in phononics," *Nature*, vol. 503, no. 7475, pp. 209–217, Nov. 2013, doi: 10.1038/nature12608.
- [5] M. S. Kushwaha, P. Halevi, L. Dobrzynski, and B. Djafari-Rouhani, "Acoustic band structure of periodic elastic composites," *Phys. Rev. Lett.*, vol. 71, no. 13, pp. 2022–2025, Sep. 1993, doi: 10.1103/PhysRevLett.71.2022.
- [6] R. Martínez-Sala, J. Sancho, J. V. Sánchez, V. Gómez, J. Llinares, and F. Meseguer, "Sound attenuation by sculpture," *Nature*, vol. 378, no. 6554, Art. no. 6554, Nov. 1995, doi: 10.1038/378241a0.
- [7] T. Gorishnyy, C. K. Ullal, M. Maldovan, G. Fytas, and E. L. Thomas, "Hypersonic Phononic Crystals," *Phys. Rev. Lett.*, vol. 94, no. 11, p. 115501, Mar. 2005, doi: 10.1103/PhysRevLett.94.115501.
- [8] J.-K. Yu, S. Mitrovic, D. Tham, J. Varghese, and J. R. Heath, "Reduction of thermal conductivity in phononic nanomesh structures," *Nat. Nanotechnol.*, vol. 5, no. 10, pp. 718–721, Oct. 2010, doi: 10.1038/nnano.2010.149.
- [9] M. Maldovan and E. L. Thomas, "Simultaneous localization of photons and phonons in two-dimensional periodic structures," *Appl. Phys. Lett.*, vol. 88, no. 25, p. 251907, Jun. 2006, doi: 10.1063/1.2216885.
- [10] B. Li, L. Wang, and G. Casati, "Thermal Diode: Rectification of Heat Flux," *Phys. Rev. Lett.*, vol. 93, no. 18, p. 184301, Oct. 2004, doi: 10.1103/PhysRevLett.93.184301.
- [11] M. Terraneo, M. Peyrard, and G. Casati, "Controlling the Energy Flow in Nonlinear Lattices: A Model for a Thermal Rectifier," *Phys. Rev. Lett.*, vol. 88, no. 9, p. 094302, Feb. 2002, doi: 10.1103/PhysRevLett.88.094302.
- [12] A. H. Safavi-Naeini and O. Painter, "Design of optomechanical cavities and waveguides on a simultaneous bandgap phononic-photonic crystal slab," *Opt. Express*, vol. 18, no. 14, pp. 14926–14943, Jul. 2010, doi: 10.1364/OE.18.014926.

- [13] A. H. Safavi-Naeini, T. P. M. Alegre, M. Winger, and O. Painter, "Optomechanics in an ultrahigh-Q two-dimensional photonic crystal cavity," *Appl. Phys. Lett.*, vol. 97, no. 18, p. 181106, Nov. 2010, doi: 10.1063/1.3507288.
- [14] A. V. Akimov *et al.*, "Hypersonic Modulation of Light in Three-Dimensional Photonic and Phononic Band-Gap Materials," *Phys. Rev. Lett.*, vol. 101, no. 3, p. 033902, Jul. 2008, doi: 10.1103/PhysRevLett.101.033902.
- [15] E. Gavartin *et al.*, "Optomechanical Coupling in a Two-Dimensional Photonic Crystal Defect Cavity," *Phys. Rev. Lett.*, vol. 106, no. 20, p. 203902, May 2011, doi: 10.1103/PhysRevLett.106.203902.
- [16] Y. Pennec *et al.*, "Simultaneous existence of phononic and photonic band gaps in periodic crystal slabs," *Opt. Express*, vol. 18, no. 13, pp. 14301–14310, Jun. 2010, doi: 10.1364/OE.18.014301.
- [17] S. Sadat-Saleh, S. Benchabane, F. I. Baida, M.-P. Bernal, and V. Laude, "Tailoring simultaneous photonic and phononic band gaps," *J. Appl. Phys.*, vol. 106, no. 7, p. 074912, Oct. 2009, doi: 10.1063/1.3243276.
- [18] Y. Xie *et al.*, "The defect level and ideal thermal conductivity of graphene uncovered by residual thermal reffusivity at the 0 K limit," *Nanoscale*, vol. 7, no. 22, pp. 10101–10110, 2015, doi: 10.1039/C5NR02012C.
- [19] G. E. Moore, "Cramming more components onto integrated circuits, Reprinted from *Electronics*, volume 38, number 8, April 19, 1965, pp.114 ff.," *IEEE Solid-State Circuits Soc. Newsl.*, vol. 11, no. 3, pp. 33–35, Sep. 2006, doi: 10.1109/N-SSC.2006.4785860.
- [20] "Balandin-Spectrum.pdf." Accessed: May 18, 2020. [Online]. Available: <https://balandin-group.ucr.edu/publications/2009/7/Balandin-Spectrum.pdf>.
- [21] S. Ghosh *et al.*, "Extremely high thermal conductivity of graphene: Prospects for thermal management applications in nanoelectronic circuits," *Appl. Phys. Lett.*, vol. 92, no. 15, p. 151911, Apr. 2008, doi: 10.1063/1.2907977.
- [22] S. K. Jaćimovski, M. Bukurov, J. P. Šetrajić, and D. I. Raković, "Phonon thermal conductivity of graphene," *Superlattices Microstruct.*, vol. 88, pp. 330–337, Dec. 2015, doi: 10.1016/j.spmi.2015.09.027.
- [23] A. A. Balandin, "Thermal properties of graphene and nanostructured carbon materials," *Nat. Mater.*, vol. 10, no. 8, Art. no. 8, Aug. 2011, doi: 10.1038/nmat3064.
- [24] T. Gunst, J. T. Lu, T. Markussen, A.-P. Jauho, and M. Brandbyge, "Thermoelectric properties of disordered graphene antidot devices," presented at the International Workshop on Computational Electronics, 2012, Accessed: Jul. 02, 2020. [Online]. Available:

<https://orbit.dtu.dk/en/publications/thermoelectric-properties-of-disordered-graphene-antidot-devices>.

- [25] J. Guo, "Band gap of strained graphene nanoribbons," Accessed: Jul. 02, 2020. [Online]. Available: <https://core.ac.uk/reader/81517192>.
- [26] D. G. Cahill, "Thermal conductivity measurement from 30 to 750 K: the 3ω method," *Rev. Sci. Instrum.*, vol. 61, no. 2, pp. 802–808, Feb. 1990, doi: 10.1063/1.1141498.
- [27] X. Zhou *et al.*, "Two three-dimensional metal–organic frameworks constructed by thiazole-spaced pyridinecarboxylates exhibiting selective gas sorption or antiferromagnetic coupling," *New J. Chem.*, vol. 37, no. 2, pp. 425–430, Jan. 2013, doi: 10.1039/C2NJ40805H.
- [28] R. Chen, A. I. Hochbaum, P. Murphy, J. Moore, P. Yang, and A. Majumdar, "Thermal Conductance of Thin Silicon Nanowires," *Phys. Rev. Lett.*, vol. 101, no. 10, p. 105501, Sep. 2008, doi: 10.1103/PhysRevLett.101.105501.
- [29] A. I. Hochbaum *et al.*, "Enhanced thermoelectric performance of rough silicon nanowires," *Nature*, vol. 451, no. 7175, pp. 163–167, Jan. 2008, doi: 10.1038/nature06381.
- [30] D. Li, Y. Wu, P. Kim, L. Shi, P. Yang, and A. Majumdar, "Thermal conductivity of individual silicon nanowires," *Appl. Phys. Lett.*, vol. 83, no. 14, pp. 2934–2936, Sep. 2003, doi: 10.1063/1.1616981.
- [31] "Thermal conductivity of silicon bulk and nanowires: Effects of isotopic composition, phonon confinement, and surface roughness: Journal of Applied Physics: Vol 107, No 8." <https://aip.scitation.org/doi/10.1063/1.3340973> (accessed Feb. 03, 2020).
- [32] A. A. Balandin *et al.*, "Superior Thermal Conductivity of Single-Layer Graphene," *Nano Lett.*, vol. 8, no. 3, pp. 902–907, Mar. 2008, doi: 10.1021/nl0731872.
- [33] "Thermal properties of graphene and nanostructured carbon materials | Nature Materials." <https://www.nature.com/articles/nmat3064> (accessed Feb. 02, 2020).
- [34] P. Kim, L. Shi, A. Majumdar, and P. L. McEuen, "Thermal Transport Measurements of Individual Multiwalled Nanotubes," *Phys. Rev. Lett.*, vol. 87, no. 21, p. 215502, Oct. 2001, doi: 10.1103/PhysRevLett.87.215502.
- [35] Y. Song, W. Fang, R. Brenes, and J. Kong, "Challenges and opportunities for graphene as transparent conductors in optoelectronics," *Nano Today*, vol. 10, no. 6, pp. 681–700, Dec. 2015, doi: 10.1016/j.nantod.2015.11.005.
- [36] K. S. Novoselov *et al.*, "Electric field effect in atomically thin carbon films," *Science*, vol. 306, no. 5696, pp. 666–669, Oct. 2004, doi: 10.1126/science.1102896.
- [37] "PhD_slavisa_milovanovic.pdf." Accessed: Feb. 14, 2020. [Online]. Available: http://nano.uantwerpen.be/cmt/PhD_slavisa_milovanovic.pdf.
- [38] C. Kittel, "Introduction to Solid State Physics," p. 12.

- [39] J. Gonzalez, "Ab Initio Study of the Electronic and Vibrational Properties of 1-nm-Diameter Single-Walled Nanotubes," *Adv. Mater. Phys. Chem.*, vol. 3, p. 178, Jan. 2013.
- [40] S. Chen *et al.*, "Raman measurements of thermal transport in suspended monolayer graphene of variable sizes in vacuum and gaseous environments," *ACS Nano*, vol. 5, no. 1, pp. 321–328, Jan. 2011, doi: 10.1021/nn102915x.
- [41] A. Arora, T. Hori, T. Shiga, and J. Shiomi, "Thermal rectification in restructured graphene with locally modulated temperature dependence of thermal conductivity," *Phys. Rev. B*, vol. 96, no. 16, p. 165419, Oct. 2017, doi: 10.1103/PhysRevB.96.165419.
- [42] C. Dames, "Solid-State Thermal Rectification With Existing Bulk Materials," *J. Heat Transf.*, vol. 131, no. 6, Jun. 2009, doi: 10.1115/1.3089552.
- [43] W. Kobayashi, Y. Teraoka, and I. Terasaki, "An oxide thermal rectifier," *Appl. Phys. Lett.*, vol. 95, no. 17, p. 171905, Oct. 2009, doi: 10.1063/1.3253712.
- [44] N. Yang, G. Zhang, and B. Li, "Carbon nanocone: A promising thermal rectifier," *Appl. Phys. Lett.*, vol. 93, no. 24, p. 243111, Dec. 2008, doi: 10.1063/1.3049603.
- [45] C. W. Chang, D. Okawa, A. Majumdar, and A. Zettl, "Solid-State Thermal Rectifier," *Science*, vol. 314, no. 5802, pp. 1121–1124, Nov. 2006, doi: 10.1126/science.1132898.
- [46] H. Wang, S. Hu, K. Takahashi, X. Zhang, H. Takamatsu, and J. Chen, "Experimental study of thermal rectification in suspended monolayer graphene," *Nat. Commun.*, vol. 8, no. 1, Art. no. 1, Jun. 2017, doi: 10.1038/ncomms15843.
- [47] M. Maldovan, "Phonon wave interference and thermal bandgap materials," *Nat. Mater.*, vol. 14, no. 7, pp. 667–674, Jul. 2015, doi: 10.1038/nmat4308.
- [48] K. S. Novoselov *et al.*, "Two-dimensional atomic crystals," *Proc. Natl. Acad. Sci.*, vol. 102, no. 30, pp. 10451–10453, Jul. 2005, doi: 10.1073/pnas.0502848102.
- [49] H. Malekpour *et al.*, "Thermal Conductivity of Graphene Laminate," *Nano Lett.*, vol. 14, no. 9, pp. 5155–5161, Sep. 2014, doi: 10.1021/nl501996v.
- [50] A. K. Geim and K. S. Novoselov, "The rise of graphene," *Nat. Mater.*, vol. 6, no. 3, pp. 183–191, Mar. 2007, doi: 10.1038/nmat1849.
- [51] M. E. Schmidt *et al.*, "Structurally Controlled Large-Area 10 nm Pitch Graphene Nanomesh by Focused Helium Ion Beam Milling," *ACS Appl. Mater. Interfaces*, vol. 10, no. 12, pp. 10362–10368, Mar. 2018, doi: 10.1021/acsami.8b00427.
- [52] L. Yang, J. Chen, N. Yang, and B. Li, "Significant Reduction of Graphene Thermal Conductivity by Phononic Crystal Structure," *Int. J. Heat Mass Transf.*, vol. 91, pp. 428–432, Dec. 2015, doi: 10.1016/j.ijheatmasstransfer.2015.07.111.

- [53] E. J. F. Dickinson, H. Ekström, and E. Fontes, "COMSOL Multiphysics®: Finite element software for electrochemical analysis. A mini-review," *Electrochem. Commun.*, vol. 40, pp. 71–74, Mar. 2014, doi: 10.1016/j.elecom.2013.12.020.
- [54] "Detailed Explanation of the Finite Element Method (FEM)." <https://www.comsol.jp/multiphysics/finite-element-method> (accessed Feb. 12, 2020).
- [55] COMSOL MULTIPHYSICS version 5.3. .
- [56] E. W. Montroll, "Size Effect in Low Temperature Heat Capacities," *J. Chem. Phys.*, vol. 18, no. 2, pp. 183–185, Feb. 1950, doi: 10.1063/1.1747584.
- [57] M. Collet, M. Ouisse, M. Ruzzene, and M. N. Ichchou, "Floquet–Bloch decomposition for the computation of dispersion of two-dimensional periodic, damped mechanical systems," *Int. J. Solids Struct.*, vol. 48, no. 20, pp. 2837–2848, Oct. 2011, doi: 10.1016/j.ijsolstr.2011.06.002.
- [58] S. Kubo, M. E. Schimidt, M. Muruganathan, and H. Mizuta, "Finite element method simulation of graphene phononic crystals with cross-shaped nanopores," in *2019 20th International Conference on Thermal, Mechanical and Multi-Physics Simulation and Experiments in Microelectronics and Microsystems (EuroSimE)*, Hannover, Germany, Mar. 2019, pp. 1–5, doi: 10.1109/EuroSimE.2019.8724552.
- [59] H. M. Masrura *et al.*, "Design of Graphene Phononic Crystals for Heat Phonon Engineering," *Micromachines*, vol. 11, no. 7, Art. no. 7, Jul. 2020, doi: 10.3390/mi11070655.
- [60] "Graphene," *Wikipedia*. Feb. 13, 2020, Accessed: Feb. 14, 2020. [Online]. Available: <https://en.wikipedia.org/w/index.php?title=Graphene&oldid=940587839>.
- [61] A. W. Tsen *et al.*, "Tailoring electrical transport across grain boundaries in polycrystalline graphene," *Science*, vol. 336, no. 6085, pp. 1143–1146, Jun. 2012, doi: 10.1126/science.1218948.
- [62] A. V. Zaretski *et al.*, "Metal-assisted exfoliation (MAE): green, roll-to-roll compatible method for transferring graphene to flexible substrates," *Nanotechnology*, vol. 26, no. 4, p. 045301, Jan. 2015, doi: 10.1088/0957-4484/26/4/045301.
- [63] J. C. Meyer, A. K. Geim, M. I. Katsnelson, K. S. Novoselov, T. J. Booth, and S. Roth, "The structure of suspended graphene sheets," *Nature*, vol. 446, no. 7131, Art. no. 7131, Mar. 2007, doi: 10.1038/nature05545.
- [64] X. Li *et al.*, "Transfer of Large-Area Graphene Films for High-Performance Transparent Conductive Electrodes," *Nano Lett.*, vol. 9, no. 12, pp. 4359–4363, Dec. 2009, doi: 10.1021/nl902623y.
- [65] M. Yi and Z. Shen, "A review on mechanical exfoliation for the scalable production of graphene," *J. Mater. Chem. A*, vol. 3, no. 22, pp. 11700–11715, May 2015, doi: 10.1039/C5TA00252D.

- [66] C. Mattevi, H. Kim, and M. Chhowalla, "A review of chemical vapour deposition of graphene on copper," *J. Mater. Chem.*, vol. 21, no. 10, pp. 3324–3334, Feb. 2011, doi: 10.1039/C0JM02126A.
- [67] K. S. Kim *et al.*, "Large-scale pattern growth of graphene films for stretchable transparent electrodes," *Nature*, vol. 457, no. 7230, pp. 706–710, Feb. 2009, doi: 10.1038/nature07719.
- [68] G. Q. Ding *et al.*, "Chemical vapor deposition of graphene on liquid metal catalysts," *Carbon*, vol. 53, pp. 321–326, 2013, doi: 10.1016/j.carbon.2012.11.018.
- [69] J. W. Suk *et al.*, "Transfer of CVD-grown monolayer graphene onto arbitrary substrates," *ACS Nano*, vol. 5, no. 9, pp. 6916–6924, Sep. 2011, doi: 10.1021/nn201207c.
- [70] X. Li *et al.*, "Transfer of Large-Area Graphene Films for High-Performance Transparent Conductive Electrodes," *Nano Lett.*, vol. 9, no. 12, pp. 4359–4363, Dec. 2009, doi: 10.1021/nl902623y.
- [71] G. Li *et al.*, "Continuous control of the nonlinearity phase for harmonic generations," *Nat. Mater.*, vol. 14, no. 6, pp. 607–612, Jun. 2015, doi: 10.1038/nmat4267.
- [72] D. Emmrich *et al.*, "Nanopore fabrication and characterization by helium ion microscopy," *Appl. Phys. Lett.*, vol. 108, no. 16, p. 163103, Apr. 2016, doi: 10.1063/1.4947277.
- [73] J.-H. Chen, C. Jang, S. Xiao, M. Ishigami, and M. S. Fuhrer, "Intrinsic and extrinsic performance limits of graphene devices on SiO₂," *Nat. Nanotechnol.*, vol. 3, no. 4, pp. 206–209, Apr. 2008, doi: 10.1038/nnano.2008.58.
- [74] J. Hu, X. Ruan, and Y. P. Chen, "Thermal Conductivity and Thermal Rectification in Graphene Nanoribbons: A Molecular Dynamics Study," *Nano Lett.*, vol. 9, no. 7, pp. 2730–2735, Jul. 2009, doi: 10.1021/nl901231s.
- [75] W. Jeong, K. Kim, Y. Kim, W. Lee, and P. Reddy, "Characterization of nanoscale temperature fields during electromigration of nanowires," *Sci. Rep.*, vol. 4, no. 1, pp. 1–6, May 2014, doi: 10.1038/srep04975.
- [76] Electrical4U, "Drift Velocity Drift Current and Electron Mobility | Electrical4U," <https://www.electrical4u.com/>. <https://www.electrical4u.com/drift-velocity-drift-current-and-electron-mobility/> (accessed Feb. 09, 2020).
- [77] "Heat Transfer Module Updates - COMSOL® 5.4 Release Highlights," *COMSOL Multiphysics®*. <https://www.comsol.jp/release/5.4/heat-transfer-module> (accessed Feb. 10, 2020).
- [78] J. Sun, W. Wang, M. Muruganathan, and H. Mizuta, "Low pull-in voltage graphene electromechanical switch fabricated with a polymer sacrificial spacer," *Appl. Phys. Lett.*, vol. 105, no. 3, p. 033103, Jul. 2014, doi: 10.1063/1.4891055.

- [79] Y. Zhang *et al.*, “Strain Modulation of Graphene by Nanoscale Substrate Curvatures: A Molecular View,” *Nano Lett.*, vol. 18, no. 3, pp. 2098–2104, Mar. 2018, doi: 10.1021/acs.nanolett.8b00273.
- [80] K. G. S. H. Gunawardana, K. Mullen, J. Hu, Y. P. Chen, and X. Ruan, “Tunable thermal transport and thermal rectification in strained graphene nanoribbons,” *Phys. Rev. B*, vol. 85, no. 24, p. 245417, Jun. 2012, doi: 10.1103/PhysRevB.85.245417.
- [81] T. M. G. Mohiuddin *et al.*, “Uniaxial strain in graphene by Raman spectroscopy: G peak splitting, Grüneisen parameters, and sample orientation,” *Phys. Rev. B*, vol. 79, no. 20, p. 205433, May 2009, doi: 10.1103/PhysRevB.79.205433.
- [82] “breakdown of wiedemann-franz law.pdf.” .
- [83] “thermal transport zone folding_edward.pdf.” .
- [84] H. Wang, S. Hu, K. Takahashi, X. Zhang, H. Takamatsu, and J. Chen, “Experimental study of thermal rectification in suspended monolayer graphene,” *Nat. Commun.*, vol. 8, no. 1, Art. no. 1, Jun. 2017, doi: 10.1038/ncomms15843.
- [85] J. O. Vasseur, P. A. Deymier, B. Djafari-Rouhani, Y. Pennec, and A.-C. Hladky-Hennion, “Absolute forbidden bands and waveguiding in two-dimensional phononic crystal plates,” *Phys. Rev. B*, vol. 77, no. 8, p. 085415, Feb. 2008, doi: 10.1103/PhysRevB.77.085415.
- [86] C. Croënne, E. J. S. Lee, H. Hu, and J. H. Page, “Band gaps in phononic crystals: Generation mechanisms and interaction effects,” *AIP Adv.*, vol. 1, no. 4, p. 041401, Dec. 2011, doi: 10.1063/1.3675797.
- [87] N. Zen, T. A. Puurtinen, T. J. Isotalo, S. Chaudhuri, and I. J. Maasilta, “Engineering thermal conductance using a two-dimensional phononic crystal,” *Nat. Commun.*, vol. 5, p. 3435, Mar. 2014, doi: 10.1038/ncomms4435.
- [88] W. Jang, Z. Chen, W. Bao, C. N. Lau, and C. Dames, “Thickness-Dependent Thermal Conductivity of Encased Graphene and Ultrathin Graphite,” *Nano Lett.*, vol. 10, no. 10, pp. 3909–3913, Oct. 2010, doi: 10.1021/nl101613u.
- [89] J. H. Seol *et al.*, “Two-Dimensional Phonon Transport in Supported Graphene,” *Science*, vol. 328, no. 5975, pp. 213–216, Apr. 2010, doi: 10.1126/science.1184014.

List of publications

Academic journals

1. **Haque Mayeesha Masrura**, Afsal Kareekunnnan, Fayong Liu, Sankar Ganesh Ramaraj, Günter Ellrott, Ahmmed MM Hammam, Manoharan Muruganathan and Hiroshi Mizuta, **Design of Graphene Phononic Crystals for Heat Phonon Engineering**, *Micromachines* 2020, 11(7), 655 / DOI: 10.3 0655
2. Fayong Liu, Zhongwang Wang, Soya Nakanao, Shinichi Ogawa, Yukinori Morita, Marek Schmidt, **Mayeesha Haque**, Manoharan Muruganathan and Hiroshi Mizuta, **Conductance Tunable Suspended Graphene Nanomesh by Helium Ion Milling**, *Micromachines* 2020, 11(4), 387; DOI:10.3390/ mi11040387
3. M. E. Schmidt, T. Iwasaki, M. Muruganathan, **M. Haque**, NH Van, S. Ogawa and H. Mizuta, **Structurally Controlled Large-Area 10 nm Pitch Graphene Nanomesh by Focused Helium Ion Beam Milling**, *ACS Applied Materials & Interfaces* (2018), Vol.10, No. 12, pp. 10362-10368, DOI:10.1021/acsami.8b00427

International conferences (in chronological order)

1. **Sub-10-nm Pitch Nanopore Array in Graphene by Helium Ion Beam Milling for Heat Phonon engineering**
Marek E. Schmidt, Teruhisa Kanzaki, **Mayeesha Haque**, Takuya Iwasaki, Manoharan Muruganathan, Shinichi Ogawa and Hiroshi Mizuta
HybridQS Workshop, Miyagi-Zao, Japan, 10-13 September, 2017
2. **Downscaled graphene nano-electro-mechanical (NEM) devices for extreme sensing and phonon engineering applications (Keynote Speech)**
H. Mizuta, H. Van Ngoc, M. E. Schmidt, **M. Haque**, T. Iwasaki, S. Ogawa, M. Muruganathan
2nd International Carbon Materials Conference & Exhibition (Carbontech2017), Beijing, 18-19 December 2017
3. **Phononic bandgap formation in single nanometer graphene nanomesh**
M. Haque, M. E. Schmidt, M. Muruganathan, I. Katayama, J. Takeda, S. Ogawa, H. Mizuta
The 1st JAIST World Conference (JWC2018), Nomi, 27-28 February 2018
4. **Phononic Bandgap Engineering in Single Nanometer Graphene Nanomesh**
Mayeesha M. Haque, Marek E. Schmidt, M. Muruganathan, I. Katayama, J. Takeda, S. Ogawa, H. Mizuta
Joint Conference of the 16th International Conference on Phonon Scattering in Condensed Matter (Phonons 2018) and the 4th International Conference on Phononics and Thermal Energy Science (PTES 2018), Nanjing, China, 31 May - 3 June 2018
5. **Graphene NEMS technology for extreme sensing and nano thermal engineering (Plenary Speech)**
H. Mizuta, M. E. Schmidt, **M. Haque**, S. Kubo, G. Agbonlahor, H. Miyashita, J. Kulothungan, S. Ogawa and M. Muruganathan
19th EuroSciCon Conference on Nanotechnology & Smart Materials, Amsterdam, 4-6

October, 2018

6. **Graphene nano-electro-mechanical (NEM) device technology for extreme sensing, sub-thermal switching and heat phonon engineering (Invited Talk)**
H. Mizuta, M. E. Schmidt, **M. Haque**, S. Kubo, G. Agbonlahor, H. Miyashita, J. Kulothungan, S. Ogawa and M. Muruganathan
3rd International Conference on Emerging Advanced Nanomaterials (ICEAN 2018), Newcastle, Australia, 30 Oct. - 2 Nov., 2018

National conferences (in chronological order)

1. **グラフェン NEMS 上でのシングルナノスケールフォノン結晶の作製**
水田 博, Marek Schmidt, **Mayeesha Haque**, 小川 真一, 衛藤 宏明, Manoharan Muruganathan
応用物理学会フォノンエンジニアリング研究グループ JST「微小エネ」領域合同研究会
2017年7月14日-15日 熱海
2. **Effects of structural dimensions on phonon bandgaps in nanopatterned graphene phononic crystals**
Mayeesha M. Haque, Marek E. Schmidt, Takuya Iwasaki, Manoharan Muruganathan, Hiroshi Mizuta
第78回応用物理学会秋季学術講演会
2017年9月5日-8日 福岡国際会議場・国際センター・福岡サンパレス
3. **Single-nanometer graphene patterning with helium ion beam for extreme sensing and phonon engineering applications (招待講演)**
Hiroshi Mizuta, Marek E. Schmidt, **Mayeesha Haque**, Shinichi Ogawa, Manoharan Muruganathan
第78回応用物理学会秋季学術講演会
シンポジウム「GFIS(電界電離ガスイオン源)・先端イオン源顕微鏡技術とその材料・デバイス研究開発への応
4. **Probing graphene nanomesh fidelity by electrical transport measurement**
Marek Edward Schmidt, Takuya Iwasaki, Manoharan Muruganathan, **Mayeesha Haque**, Ngoc V. Huynh, Shinichi Ogawa, Hiroshi Mizuta
第65回応用物理学会春季学術講演会
2018年3月17日-20日、早稲田大学西早稲田キャンパス・ベルサール高田馬場
5. **広帯域顕微コヒーレントフォノン分光法の開発**
田岡 裕貴, 神島 悠司, 奈良 脩平, 嵐田 雄介, 小川 真一, **Mayeesha Haque**, Marek Schmidt, Manoharan Muruganathan, 水田 博, 片山 郁文, 武田 淳
第65回応用物理学会春季学術講演会
2018年3月17日-20日、早稲田大学西早稲田キャンパス・ベルサール高田馬場

6. **Suspension of large, electrically contacted graphene for sub-15-nm phononic crystal patterning**
Marek Edward Schmidt, Mayeasha Haque, Manoharan Muruganathan, Ikufumi Katayama, Jun Takeda, Shinichi Ogawa, Hiroshi Mizuta
第 65 回応用物理学会春季学術講演会
2018 年 3 月 17 日-20 日、早稲田大学西早稲田キャンパス・ベルサール高田馬場
7. **Graphene Nanophononics: Sample fabrication and FEM Simulation I**
Mayeasha M. Haque, Seiya Kubo, Marek E. Schmidt, Manoharan Muruganathan, Shinichi Ogawa, Hiroshi Mizuta
第 2 回フォノンエンジニアリング研究会
2018 年 7 月 13 日-14 日、KKR ホテル熱海
8. **Graphene Nanophononics: Suspended Heat spreader measurement and FEM Simulation II**
Seiya Kubo, Mayeasha M. Haque, Marek E. Schmidt, Manoharan Muruganathan, Hiroshi Mizuta
第 2 回フォノンエンジニアリング研究会
2018 年 7 月 13 日-14 日、KKR ホテル熱海
9. **3D FEM analysis of graphene phononic crystals with noncircular nanopores(presented in Japanese)**
S. Kubo, M. E. Schmidt, M. Haque, M. Manoharan, H. Mizuta
第 79 回応用物理学会秋季学術講演会
2018 年 9 月 18 日-21 日、名古屋国際会議場
10. **Fabrication process and thermal conductivity measurement setup of graphene phononic crystal**
M. Haque, S. Kubo, M. E. Schmidt, M. Muruganathan, S. Ogawa, H. Mizuta
第 79 回応用物理学会秋季学術講演会
2018 年 9 月 18 日-21 日、名古屋国際会議場
11. **Graphene nanoelectromechanical (GNEM) devices functionalized by using helium ion beam for nanoscale thermal engineering**
H. Mizuta, M. Haque, S. Kubo, M. Koyano, Y. Oshima, M. Muruganathan, Y. Arashida, I. Katayama, J. Takeda, S. Ogawa, M.E. Schmidt
第 79 回応用物理学会秋季学術講演会
2018 年 9 月 18 日-21 日、名古屋国際会議場